

Biomimetic Actuators

by

Yu Wan

A thesis submitted in partial fulfillment of the requirements for the degree of

Doctor of Philosophy

Department of Chemistry
University of Alberta

© Yu Wan, 2023

Abstract

Biomimetic actuators are receiving growing attention due to the novel ideas inspired by mother nature. By mimicking the behaviors or traits of living creatures, scientists are able to realize various functions and properties that are difficult to achieve. An enormous number of applications in robotics, biomedical, wearable devices, and autonomous smart systems are emerging and advancing thanks to the perpetual development of biomimetic actuators. With new breakthroughs and advancements in 3D printing, biomedical engineering and architecture, artificial intelligence, machine learning, and brain machine interface, biomimetic actuators are now in a prosperous era. Chapter 1 gives a thorough introduction to biomimicry from the perspective of properties and functions as well as some discussion on biomimetic actuators in terms of the materials and working mechanisms. In Chapter 2, we developed a wireless swimming device with sensing capability. The swimming behavior was inspired by an octopus; it can swim slowly under normal conditions, but snaps quickly away to escape predators. Chapter 3 focuses on developing a touch-responsive actuator, mimicking the behavior of the shy plant, *Mimosa Pudica*. The actuator was able to close its “leaves” upon a fingertip touch. Chapter 4 focused on a porous magnetic hydrogel actuator capable of morphing in size as well as capturing and transporting cargo under the actuation of heat produced by magneto-thermo effect. In Chapter 5, a conclusion and future outlook are discussed. Finally, Appendix A, B, C, and D are included as supplementary information and some preliminary experiments during my Ph.D. program.

Preface

This thesis is an original work by Yu Wan (Y. Wan) performed under the supervision of Dr. Michael J. Serpe (M. J. Serpe). M. J. Serpe was involved in the generation of ideas, reasoning, and discussion of the obtained experimental results of all works.

Chapter 2 of this thesis has been published as Y. Wan, K. Cuff, M. J. Serpe, “A Wirelessly Controlled Shape-Memory Alloy-Based Bistable Metal Swimming Device”, *Adv. Intel. Syst.* **2022**, 210025. I was responsible for the ideas, experimental design, data collection and analysis as well as the manuscript composition. M. J. Serpe was the supervisory author and was involved with the research design and manuscript composition. K. Cuff helped on coding and the design of the electronic systems.

Chapter 3 of this thesis is in preparation for submission for peer review and publication. I was responsible for the ideas, experimental design, data collection and analysis as well as the manuscript composition. M. J. Serpe was the supervisory author and was involved with research design and manuscript composition.

Acknowledgements

This incredible journey finally has come to an end. What it comes with is not only exuberant joy but also some sort of sorrow. Joy is for the years of hard work that paid off and getting ready for the next chapter of my life. Sorrow is for having to say goodbye to everything and everyone that accompanied me for the past few years.

First, I would like to thank my supervisor Michael J. Serpe (Mike). Mike has been a supportive supervisor and friend since the first day I met him at the Christmas party in 2016. Mike is very ambitious about scientific research and always has a lot of ideas. He gave constructive advice whenever I encountered difficulties on my research. Mike is open minded and allows us to explore various topics that we are interested in. Without his support and insightful suggestions, I would never be able to achieve my goals in my Ph.D. program. Mike is a friend, with whom I can talk about anything care-free. We always share our stories and anecdotes with each other. We talk about food, movies, music, politics, and anything that came to our mind during lunch or get-togethers. You will always feel relaxed and be your true self around him. Mike also has a welcoming family, his wife Tiffany, who is an extremely nice with her hospitality and his lovely daughter Beatrice. We have holiday parties, summer BBQs, and just get-togethers for chatting and relaxing, which made my life full of joy and gratitude.

I also would like to thank the past and current Serpe group members for their support. I would give a special thanks to Keith, who helped me with the development of the swimming device. Building the device from scratch and seeing it come to life and perfect, bit by bit, is incredible experience.

A special thanks to my committee members Dr. Jonathan Veinot and Dr. Mark McDermott for their constructive criticism and valuable support. I would like to thank Dr. Cagri Ayranci, Dr. Hyun-Joong Chung, and Dr. Charles A. Lucy for agreeing to be the examiners for my candidacy exam. I also want to thank Dr. Cagri Ayranci for agreeing to be the arm's length examiner, as well as Dr. Yue Zhao as the external examiner for my defense.

Specifically, I am truly grateful to Anna Jordan for her meticulous work on proofreading this thesis. My thesis writing was a long journey, but she was always

there to help.

I would like to extend my gratitude to Anita Weiler for helping with my questions on scholarship applications, deadlines, forms, etc. Also, I am thankful for the guidance from the lab coordinators, Norman Gee, Yoram Apelblat, and Gregory Kiema, who helped me to be a better TA.

Thank you to all the funding agencies for the scholarship or financial support, specifically, Alberta Innovates for the Alberta Innovates Graduate Student Scholarship and Future Energy Systems for the FES Student and Postdoctoral Opportunity Award.

Finally, I would like to thank my family and friends for their unconditional support and love. Your love will keep nourishing me in the future. I love you all!!!

Table of Contents

| | |
|---|------|
| Abstract | ii |
| Preface | iii |
| Acknowledgement | iv |
| Table of Contents | vi |
| List of Figures | ix |
| List of Abbreviation | xxii |
| Chapter 1 | 1 |
| Introduction to Biomimetic Actuators | 1 |
| 1.1 Biomimicry | 1 |
| 1.2 Biomimetic Applications | 3 |
| 1.3 Biomimetic Actuators | 13 |
| 1.4 Challenges and Outlooks | 41 |
| Chapter 2 | 43 |
| Octopus-Like Shape-Memory-Alloy-Based Bistable Metal Actuators | 43 |
| 2.1 Introduction | 43 |
| 2.2 Experimental Section | 45 |
| 2.3 Results and Discussion | 50 |
| 2.4 Conclusions | 66 |
| Chapter 3 | 67 |
| Mimosa Pudica-like Touch-responsive Actuators | 67 |
| 3.1 Introduction | 67 |
| 3.2 Experimental Section | 69 |
| 3.3 Results and Discussion | 74 |
| 3.4 Conclusions | 85 |
| Chapter 4 | 87 |
| Temperature- and Magnetic Field-responsive Actuators for Cargo Transportation ... | 87 |

| | |
|--|-----|
| 4.1 Introduction | 87 |
| 4.2 Experimental Section | 88 |
| 4.3 Results and Discussion | 92 |
| 4.4 Conclusions | 102 |
| Chapter 5 | 104 |
| Conclusions and Future Outlook | 104 |
| References | 108 |
| Appendix A | 116 |
| Studies on Temperature & Salt Responses of PNIPAm-based Hydrogels..... | 116 |
| A.1 Introduction | 116 |
| A.2 Experimental Section..... | 116 |
| A.3 Results and Discussion | 118 |
| A.4 Conclusions and Outlook | 124 |
| Appendix B | 125 |
| Poly(Ethylene Glycol) Diacrylate-based Hydrogel Actuators in Response to Alkaline Potassium Ions | 125 |
| B.1 Introduction..... | 125 |
| B.2 Experimental Section..... | 125 |
| B.3 Results and Discussion | 127 |
| A.4 Conclusions and Outlook | 129 |
| Appendix C | 131 |
| A PNIPAm/P(AAm-co-AAc) Bilayer Actuator with Locking and Unlocking Mechanism..... | 131 |
| C.1 Introduction..... | 131 |
| C.2 Experimental Section..... | 131 |
| C.3 Results and Discussion | 133 |
| C.4 Conclusions and Outlook..... | 134 |

| | |
|---|-----|
| Appendix D | 136 |
| Developing a Science Education Kit Based on the Swimming Device Project | 136 |
| D.1 Introduction | 136 |
| D.2 Experimental Section..... | 136 |
| D.3 Results and Discussion | 137 |
| D.4 Conclusions and Outlook | 138 |

List of Figures

Figure 1.1. a) Wind turbine blades utilizing LE tubercles.⁶ Reproduced with permission from Springer Nature. b) Octopus arm-inspired tapered soft actuators with suckers for improved grasping.⁸ The publisher for this copyrighted material is Mary Ann Liebert, Inc. publishers. c) Taken from the synchronous swimming experiment of Octobot.⁹ Reproduced with permission from Springer Nature. 3

Figure 1.2. a) Retina-inspired 2D retinomorphic hardware for MDR.¹⁶ Reproduced with permission from Springer Nature. b) Schematics of the fabrication process for μ BN and the assembled μ BN used to detect gaseous TMA. Reprinted from Ref.²⁴ with permission from Elsevier. c) Characterization of human tongue surfaces using polymeric impressions. Reprinted from Ref.²⁵ Copyright 2020, American Chemical Society. d) Prosthetic skin based on site-specifically designed SiNR electronics.²⁶ Reproduced with permission from Springer Nature. 6

Figure 1.3. a) Thermally responsive wettability for a flat PNIPAAm-modified surface.³¹ Reprinted from Ref. Copyright 2003, John Wiley & Sons, Inc. b) Dimension character of the superhydrophobic fibrous structures of both the water strider's leg and water spider's abdomen. Reprinted from Ref.³³ Copyright 2022, American Chemical Society. c) The non-wetting leg of a water strider.³² Reproduced with permission from Springer Nature. 10

Figure 1.4. a) Gecko adhesive system. Reprinted with permission from Ref.³⁵ Copyright 2006, COMPANY OF BIOLOGISTS LTD. b) Stickybot, a new bioinspired robot capable of climbing smooth surfaces. Inset: detail of toes curling to facilitate detachment. Reprinted from Ref.³⁶ Copyright 2008, IEEE. c) Photographs of *O. vulgaris* sucker. d) (a) Resin mould used to produce suction cups. The mould consists of three components: two specular external elements, p, and an internal core, c. (b) Sealed mould during liquid silicone pouring. (c) Suction cup prototypes before and after engraving. On the left, the surface of the infundibulum is completely smooth; on the right, the engraved geometry is visible. (d) Plexiglas masks used to flatten the infundibular surface during engraving. c&d were reprinted with permission from Ref.³⁷

| | |
|---|----|
| Copyright 2015, IOP Publishing Ltd. | 12 |
| Figure 1.5. a) Metal “slap bracelet”. Reprinted from Ref. ⁴⁰ Copyright 2006, ASME. b) Localized buckling under increased loads ($F_2 > F_1$). Further increasing of the localized load may lead to a complete curvature reversal. Reprinted from Ref. ⁴¹ Copyright 2019, SAGE Publications. c) Potential well schematic diagram for a bi-stable plate under the action of an MFC actuator. Reprinted from Ref. ⁴² Copyright 2011, SAGE Publications. | 14 |
| Figure 1.6. a) Atomic structures of the cubic B2, or- thorhombic B19, monoclinic B19' , and orthorhombic B33 NiTi phases with the monoclinic angle (β) and the lattice constants (a and c) indicated. Ni and Ti atoms are represented by blue (dark gray) and orange (gray) balls, respectively. Reprinted from Ref. ⁶⁴ Copyright 2015, American Physical Society. b) Systems exhibiting heliotropism and nyctinasty. Reprinted with permission from Ref. ⁶⁵ Copyright 2018, Mary Ann Liebert, Inc..... | 18 |
| Figure 1.7. a) Graphical illustration of pNIPAm used for sensing and actuation purposes. Adapted from Ref. ⁷⁰ Copyright 2021, Elsevier B.V. b) (a) Actuation of the pNIPAm–pDADMAC hydrogel/PDMS bilayer system; (b) actuation of the pNIPAm hydrogel/PDMS bilayer system. Reprinted with permission from Ref. ⁶⁹ Copyright 2017, The Royal Society of Chemistry. c) Fabrication of self-folding polymer origami. Reprinted with permission from Ref. ⁷¹ Copyright 2014, John Wiley and Sons, Inc.. | 20 |
| Figure 1.8. (a) The petiole of mimosa bends downward after being touched. (b) The mechanism of the motion is based on a swelling of the upper part of mimosa's pulvinus, while the lower part shrinks. (c) The shape change of the pulvinus is mainly induced by the directional water transfer between the lower part and the upper part because of a change of osmotic pressure. (d) Imitating the actuation of mimosa, a bilayer hydrogel consisting of a PNIPAM layer ontop of a P(AAc-co-AAm) layer is fabricated to function in open-air. (e) At low temperature (15 °C), the PNIPAM layer is swollen by water. Increasing the temperature to 40 °C leads to a shrinking of the PNIPAM layer, and directional water transfer to the P(AAc-co-AAm) layer that consequently swells and as a result lets the bilayer hydrogel bend. Reprinted with permission from Ref. ⁸⁰ Copyright 2018, Royal Society of Chemistry..... | 24 |

Figure 1.9. Setup for achieving and observing the electro-driven motility of cargo-loaded hydrogel walker. Reprinted from Ref.⁹¹ Copyright 2015, Chao Yang et al.... 28

Figure 1.10. a) The top row shows a 9 cm tip-to-tip PneuNet gripping an uncooked chicken egg. On the bottom, a modified version of the starfish-based gripper with 14 cm tip-to-tip distance; thinner and longer fingers can pick up a live anesthetized mouse. Adapted with permission from Ref.⁵⁰ Copyright 2011, John Wiley & Sons, Inc. b) Experiments to grasp different items in water by the soft robotic gripper. (P represents the liquid pressure inside the chamber of the soft actuators. Reprinted from Ref.⁹⁷ with permission from Elsevier. 30

Figure 1.11. a) Photoinduced rolling motion of a continuous ring of LCE film. Reprinted with permission from Ref.¹⁰⁰ Copyright 2008, John Wiley & Sons, Inc. b) Schematic showing leftward and rightward shift of the center of gravity in the wheel due to the UV-light-induced asymmetric deformation. Adapted with permission from Ref.¹⁰¹ Copyright 2017, John Wiley & Sons, Inc. 33

Figure 1.12. a) Highly stretchable PDMA/Fe₃O₄ magnetic NC hydrogel. Schematic of the preparation of magnetic hydrogels and Images showing three types of hydrogels. b) Remotely triggered shape morphing of magnetic hydrogels. Adapted with permission from Ref.¹¹³ Copyright 2018, Royal Society of Chemistry. 36

Figure 1.13. a) A photograph of a mussel attached to the shell of another mussel, Schematic representation of the adhesive plaque and byssal thread, and Schematic representation of the ionoprinting process. Adapted with permission from Ref.¹¹⁵ Copyright 2014, John Wiley & Sons, Inc. b) Shape memory effect of the Alg-PBA/PVA hydrogel. Reprinted with permission from Ref.¹¹⁶ Copyright 2015, John Wiley & Sons, Inc. c) Schematic illustrations of the structure of different hydrogels. Reprinted with permission from Ref.¹¹⁷ Copyright 2016, John Wiley & Sons, Inc. d) Schematic illustration of controllable self-driven hydrogel with shape memory effect. Reprinted with permission from Ref.¹¹⁸ Copyright 2018, John Wiley & Sons, Inc. .. 38

Figure 1.14. a) Conceptual scheme of the strong contractive materials based on mechanical energy storing method. Reprinted from Ref.¹²¹ Copyright 2020, Yanfei Ma et al. b) Complex shape transformations of the Lego hydrogels. Reprinted with

| | |
|---|----|
| permission from Ref. ¹²² Copyright 2014, John Wiley & Sons, Inc. | 40 |
| Figure 2.1. Hollow channel introduction. The outer layer is a straight glass tube, a plastic tube is inserted in the glass tube to get supported and avoid being bent, and a long fishing thread is placed in the middle of the plastic tube..... | 47 |
| Figure 2.2. Programming and coding. Arduino and Spyder is used to upload the code and program the Wi-Fi module. DearPyGui is used as a control panel to actuate the swimming device. | 48 |
| Figure 2.3. Layout for the 3D printed parts of the swimming device. All connecting wires can go inside the parts to avoid cluster and entanglement. | 49 |
| Figure 2.4. Picture shows the basic structure of pNIPAm microgel-based etalon composed of a monolith of microgel layer (II) sandwiched between two gold layers (I and III) on a support glass substrate (IV). To fabricate etalon chips, first, PNIPAm-based microgels containing 10% acrylic acid (AAc) (pNIPAm-co-10%AAc) were prepared by free radical precipitation polymerization of the monomer NIPAm with N,N'-methylenebis(acrylamide) (BIS) as the crosslinker and AAc as a comonomer. The resulting microgels have a size about 750 nm in diameter. For the etalon chip, 2 nm Cr and 15 nm Au were subsequently coated on to the glass slides using thermal evaporator. A layer of microgel was coated, and then another 15 nm Au layer was deposited..... | 50 |
| Figure 2.5. Conceptual design of the swimming device. The gray piece is a bistable metal strip; black coils are Nitinol wires (FL: front left; FR: front right; BL: back left; BR: back right); blue highlights around the coils are hydrogels; purple rod is a central pivot supporting plastic piece; light green lines connecting metal strip and nitinol coils are nonelastic threads. | 51 |
| Figure 2.6. Different shape designs of the bistable metal strips. The tips were tapered to a different extent. From left to right, the taper ratio becomes larger. The number below represents the shape of the strip: taper ratio (first number: tapered length; second number: untapered length). | 52 |
| Figure 2.7. Side view illustration of a) reset and b) trigger force tests. The angles are all in reference to the extended position of the metal strip. Theoretically, the angle (θ) | |

can range from 0° to 180°. However, restricted by the device design, the angle is below 90°. (Blue: bistable metal strip; black: pivot fixed onto the middle of the metal strip; silver: pulling thread; box with “F”: force sensor.)..... 52

Figure 2.8. Force-Time diagram recorded on Logger Pro software (Reset for 4–3 taper ratio at 60° angle). Each spike represents the force evolution for one test repeat (e.g., dark rectangle). The peak values are picked (e.g., dark circle) and analyzed to represent the force required to reset the metal strip..... 53

Figure 2.9. Force-Time diagram recorded at different pulling rates. Slow rate was about 2 cm/s, fast rate was about 10 cm/s. Different pulling rates yielded similar peaks indicating similar forces..... 53

Figure 2.10. Boxplot of reset forces for different taper ratios at certain trigger/reset angles **a)** 50°, **b)** 60°, and **c)** 70°. Box plot of trigger forces for different taper ratios at certain trigger/reset angles **d)** 25° **e)** 35°, and **f)** 45°. For all the angles, both reset and trigger forces decrease with more tapering on the tip..... 54

Figure 2.11. Boxplot of reset forces with different angles at certain taper ratios **a)** 4–3, **b)** 5–2, **c)** 6–1, and **d)** 7–0. Box plot of trigger forces with different taper ratios at certain angles **e)** 4–3, **f)** 5–2, **g)** 6–1, and **h)** 7–0. For all the taper ratios, both reset and trigger forces decrease with larger angle. 55

Figure 2.12. Ping pong ball test apparatus for determining bistable metal strip snapping energy output. (Bottom right red dot represents the initial position of ping pong ball; top left red dot represents the highest position the ping pong ball reaches; the height elevation is marked by the vertical height difference between the two positions.) 56

Figure 2.13. Snapping energy of different taper ratios. The figure shows the height the ping pong ball reached for different taper ratios. 7–0 is not included here because the snapping is difficult to reproduce and did not have enough force to move the ping pong ball..... 57

Figure 2.14. Differential scanning calorimetry result for a piece of Nitinol. The black curve is the heating process and red for cooling. The blue scale bar for y-axis represents 10 mW heat flow difference..... 58

| | |
|---|----|
| Figure 2.15. a) Setup for water bath actuation temperature test. b) Plot of displacement of Nitinol coil at the indicated temperatures. | 58 |
| Figure 2.16. a) Setup for no displacement actuation test (stretched Nitinol wire tied one end to the hood accessory bar, the other to a force sensor (black); red alligator clips with copper wire to apply voltage onto the Nitinol wire). b) Time needed for actuation at different voltages. c) Normalized cooling time for different voltages per unit time of heating. | 59 |
| Figure 2.17. a) Force diagram of 10 s of actuation, followed by cooling. Red dashed line represents roughly where the voltage is stopped; 86 repeats were performed. b) Force diagram of actuation until reaching 4.2 N (red dashed line) followed by cooling; 222 repeats were performed. | 61 |
| Figure 2.18. a) Polyacrylamide hydrogel coated Nitinol wires (bottom) monomer and crosslinker structures. Snapshots of Nitinol wire actuation under water b) without hydrogel coating c) with hydrogel coating (see Video S6/7). | 62 |
| Figure 2.19. a) Illustration of the electronic components and (bottom) top view of the device. b) Device side view in water tank (top: electronic components; bottom: side view of the device). | 63 |
| Figure 2.20. a) Pictures of 3D printed etalon holder and assembly (top: in air; bottom: in water). Photographs of etalons b) upon salt addition to water and c) a pH change. | 65 |
| Figure 3.1. Schematic illustration of the actuation mechanism. The polymer network is stretched under an external force. While fixed in the stretched state, the gel is crosslinked by FeCl_3 solution by coordination interaction. The gel is relaxed in DI water, but the coordination interaction prevents the crosslinked area to return to the unstretched state. Finally, when immersed in HCl solution, Fe^{3+} ions are removed, which causes the network to recover to the original shape. | 69 |
| Figure 3.2. Wax capsule fabrication. a) The set up for the fabrication process: a beaker containing hot water and a layer of melt wax; b) the process of fabrication: inject; dip; cool; remove; seal. | 70 |

Figure 3.3. Wax capsule break force test. This is one of the capsule force test experiments, which was screenshot directly from the Logger Pro software. x-axis is the elapsing time; y-axis is the force exerted onto the sensor..... 71

Figure 3.4. Hydrogel fixation process. a) A piece of rectangular hydrogel was placed on top of the glass slide; b) the hydrogel was stretched and fixed using clips; c) the fixed hydrogel was soaked in an 0.06 M FeCl_3 solution for 30 min; d) the hydrogel was transferred to DI water to remove excess Fe^{3+} ions. The crosslinking was rearranged and strengthened during this process; e) the hydrogel was removed from the tube and f) stored in DI water. 72

Figure 3.5. Illustration of the touch-responsive actuator. a) Sideview of the actuation process: (i) two pieces of pre-stretched and Fe^{3+} -fixed hydrogel sandwiching a wax capsule containing HCl solution; the two ends of the hydrogel attached to a V-shaped 3M plastic film, mimicking *M. pudica* plant leaves; (ii) fingertip applied pressure onto the hydrogel piece to break the wax capsule; (iii) the wax capsule releasing HCl solution, actuating by shrinking and pulling the two leaves closer; b) the real object of the actuator assembled with the 3M plastic film, pre-stretched and Fe^{3+} -fixed hydrogel, and wax capsule containing HCl solution..... 74

Figure 3.6. Trigger solution incorporation amount of the wax capsules. Left in the graph is the boxplot indicating the data distribution; right is the real data cluster from all the measurements..... 75

Figure 3.7. A graph showing the solution weight change over time. Different colors representing different wax capsule samples..... 76

Figure 3.8. Wax capsule breaking force. a) Experimental setup before and after the breakage of the wax capsule (the metal hook is part of the force sensor); b) wax capsule breaking force. On the left in the graph is a boxplot indicating the data distribution; right is the real data cluster from all the measurements..... 77

Figure 3.9. Pictures of the press and release process of the wax capsule containing crystal violet indicator solution. a) A wax capsule containing crystal violet was floating on the surface of water in a Petri dish; b) a finger was placed on top of the wax capsule;

c) a force was exerted onto the was capsule and ruptured it; d) the crystal violet solution continued to release in water. 77

Figure 3.10. Hydrogel dimension changes for different stretching extent after the process of stretch & fix, relaxation, and actuation, respectively. The dark gray bars are the original lengths of the hydrogels; yellow bars are the lengths after FeCl^{3+} solution soaking; light yellow bars are the lengths after DI water soaking; light gray bars are the lengths after actuation in HCl solution. 78

Figure 3.11. Hydrogel fixation in FeCl^{3+} solution and actuation in HCl solution. a) A ring-shaped hydrogel was cut from a big piece of hydrogel using the hole punch tool; b) the hydrogel was expanded on a cap and immersed in FeCl^{3+} solution; c) the fixed ring-shaped hydrogel; d) some DI water was dropped in the ring, and a wax capsule containing HCl solution was placed in the middle; e) the wax capsule was pressed till rupture; f-h) the ring-shaped hydrogel in contact with the HCl solution released from the wax capsule after 6 min, 10 min, and 30 min, respectively. (In g and h, hydrogels were outlined by a red circle to better visualize since the orange color faded.) 80

Figure 3.12. Ring-shaped hydrogel actuation repeatability. The first cycle was tested starting with the freshly made hydrogels; the hydrogels were hooked onto an Eppendorf and fixed in Fe^{3+} solution; the fixed hydrogels were soaked in DI water for relaxation and polymer chain rearrangement; the hydrogels were soaked in HCl solution for actuation. For the rest of the cycles, the same hydrogels were used repeatedly. 81

Figure 3.13. SEM images of the morphology of the hydrogel at different actuation stages. a) Freshly prepared hydrogel sample before stretching and Fe^{3+} -fixation; b) the hydrogel after stretching and Fe^{3+} -fixation; c) the hydrogel after HCl solution soaking and recovery. (Scale bar represents 1 μm for all the pictures.) 82

Figure 3.14. The actuation process for actuators wrapped in Parafilm and VHB tape. a-d) Actuator wrapped in Parafilm; e-h) actuator wrapped in VHB tape; i) the two pieces of hydrogels were unwrapped from the film and soaked in 1.0 M HCl solution after 30 min. (Scale bar represents 1 cm for all the pictures.) 83

Figure 3.15. *M. pudica* leaf folding demonstration. a) Fingertip applied pressure to

break the wax capsule inside; b-g) the HCl solution released to trigger the leaf folding for 0 min, 5 min, 10 min, 15 min, 20 min, and 25 min, respectively; h) manually detaching the hydrogel from the leaf, resulting in the leaf unfolding due to the intrinsic elastic properties of the 3M plastic film; i) the angle measurement between the two leaves during the actuation process. (Scale bar represents 1 cm for all the pictures.) 85

Figure 4.1. Preparation of porous magnetic pNIPAm hydrogel samples at room temperature. Figure created on BioRender.com. 90

Figure 4.2. Alternating magnetic field apparatus. Output of inductive heater is 24 VDC/15 A, and ~120–150 kHz. Copper coil has 7 turns, length of 5.19 cm, and is internally cooled with cold water. 92

Figure 4.3. Illustration of temperature- and magnetic field-responsive hydrogel on an “Ant man mission”. A porous hydrogel with magnetic bead embedded; objects move into the vacant pores of the swollen hydrogel; with AMF on, the hydrogel is heated and traps the objects inside; the external magnetic field guides the hydrogel with cargo through space; the AMF is switched off, the hydrogel cools and swells releasing the cargo in the pores. 92

Figure 4.4. Pictures of the different molds. a) 3D printed PLA hemisphere mold with some hemispherical wax beads; b) 3D printed PLA negative hemisphere mold; c) PDMS hemisphere mold made from negative PLA mold; d) PDMS mold made from bead templating; e) the pores left inside. 93

Figure 4.5. Wax template beads with three different sizes. a) A picture of the wax beads on a bench; b) a box plot of the wax template bead size distribution with both boxplot (left) and real data (right). 94

Figure 4.6. A bar graph showing the different surface area for hydrogels with different sizes of wax template beads. With smaller wax beads, the hydrogels have larger surface area per unit volume of hydrogel. 95

Figure 4.7. Hydrogel volume change in response to temperature change over time. a) Heating process: hydrogel is transferred from 22 °C DI water into a 40 °C water bath; b) cooling process: hydrogel is transferred from 40 °C DI water into a 22 °C water bath.

| | |
|--|-----|
| | 96 |
| Figure 4.8. Equilibrium swelling ratios for hydrogels with different porosities. a) A graph showing the different swelling ratios for different porosities; b) top: illustration showing the hydrogel network swells more around the surfaces; bottom: pictures showing the hydrogel morphologies..... | 97 |
| Figure 4.9. The magnetization process. a) The picture of the pNIPAm hydrogel; b) the picture of the pNIPAm hydrogel saturated with iron solution; c) the picture of the magnetized hydrogel after the co-precipitation synthesis..... | 98 |
| Figure 4.10. Volume changes of both the magnetized (black) and non-magnetized (red) pNIPAm hydrogels when the temperature increased from 25 °C to 40 °C. Note: the point on the curve where the slope changes sharply often is referred to as the phase transition; the corresponding temperature is referred to as the LCST. | 98 |
| Figure 4.11. Magneto-thermo effect of the magnetic particles. a) Magnetic particles collected at the bottom of a centrifuge tube; b) a picture of an IR camera image of the magnetic particles in a centrifuge tube. The red part at the center of the screen is where the magnetic particles sit..... | 99 |
| Figure 4.12. Magneto-thermo effect of the magnetic hydrogel. a) The setup for monitoring the temperature using an IR camera; b) a picture of an IR camera image of the magnetic hydrogel at 0 s; c) a picture of an IR camera image of the magnetic hydrogel at 120 s; d) a picture of an IR camera image of the magnetic hydrogel at 300 s. | 100 |
| Figure 4.13. Magneto-thermo effect of the magnetic hydrogel in a water bath at room temperature. a) Magnetic hydrogel before AMF was turned on; b) magnetic hydrogel after AMF was turned on for 20 min. The dotted lines are the reference lines for better size inspection..... | 100 |
| Figure 4.14. Cargo capture and release demonstration. a) A piece of magnet was used to direct the movement of the porous hydrogel towards the surface of the water with wax beads floating; b) the wax beads moved into the pores of the hydrogel; c) the wax bead were trapped inside of the hydrogel when the water was heated above the LCST; | |

d) The water was cooled to room temperature; wax beads were released due to the expansion of the pores of the hydrogel. 102

Figure A.1. The setup for the synthesis of hydrogels. The pre-solution sample was clamped between glass slides and put on top of a cooling plate. The UV lamp was placed at a 45° angle, irradiating the surface of the pre-solution container.117

Figure A.2. Hydrogel thermal response results and experimental pictures of the hydrogel shape changing. a) Hydrogel size change with different BIS concentrations. Different colored lines represented different UV exposure times; b) pictures of a piece of hydrogel (1 a.t.% BIS, 30 min UV exposure) immersed in 55 °C water after 5 min, 60 min, and 120 min, respectively. (Scale bar represents 0.5 cm in length.).....119

Figure A.3. Hydrogel KCl response results and experimental pictures of the hydrogel shape changing. a) Hydrogel size change with different BIS concentrations. Different colored lines represented different soaking times; b) pictures of a piece of hydrogel (2 a.t.% BIS, 60 min UV exposure) immersed in KCl solution after 0 min, 30 min, 60 min, and one day, respectively. (Scale bar represents 1.5 cm in length.)..... 120

Figure A.4. PEGDA-based hydrogel in response to KCl and experimental pictures of the hydrogel shape changing. a) Hydrogel size change with different PEGDA concentrations. Different colored lines represented different soaking times; b) pictures of a piece of hydrogel (5 a.t.% PEGDA, 30 min UV exposure) immersed in KCl solution after 0 min, 30 min, 60 min, and one day, respectively. (Scale bar represents 1.5 cm in length.) 121

Figure A.5. PEGDA+BIS-based hydrogel in response to KCl and experimental pictures of the hydrogel shape changing. a) Hydrogel size change with different PEGDA concentrations. Different colored lines represented different soaking times; b) pictures of a piece of hydrogel (4 a.t.% PEGDA) immersed in KCl solution after 0 min, 30 min, 60 min, and one day, respectively. (Scale bar represents 1.5 cm in length.) 122

Figure A.6. PVA-based hydrogel thermal response test and experimental pictures of the hydrogel shape changing. a) Hydrogel size change with different PVA concentrations. Different colored lines represented different molecular weight of PVA

used; b) pictures of a piece of hydrogel (1 w.t.% PVA, 86,000 Mr) immersed in 55 DI water after 0 s, 5 s, 60 s, and 120 s, respectively. (Scale bar represents 1.5 cm in length.)

..... 123

Figure B.1. The scheme for the synthesis of hydrogels. The pre-solution was mixed well in a centrifuge tube and poured into a Teflon gasket sandwiched between two glass slides. The solution was irradiated under UV light to polymerize. The afforded hydrogel was peeled from the mold and tested in a KCl solution. 126

Figure B.2. Illustrations of the mechanisms for the actuation and the actuator design. a) Coordination interaction between the PEG structural units and the alkaline metal ions; the polymer network changes from the extended state to the coiled state; b) bilayer actuator design composed of a PDMS passive layer and a PEGDA-based hydrogel active layer; the bilayer actuator cross-section changes from the flat state to a curved state, resulting in shape morphing of the whole actuator..... 127

Figure B.3. Hydrogel KCl salt response. a) Pictures of hydrogels with 0%, 10 %, 30%, and 50% of PEGDA incorporation after soaking in salt solution for 35 min and 60 min (black rectangles were the original sizes when they were cut); b) a bar graph showing the size change for different PEGDA incorporations; c) pictures of hydrogels with 0%, 2.0%, 5.0%, 8.0%, and 10.0% of PEGDA incorporation after soaking in salt solution.

..... 128

Figure B.4. Pictures of the PEGDA-based hydrogel/PDMS bilayer actuator shape changing in response to a 1.0 M KCl solution. a) The helical structure of the bilayer actuator after DI water equilibrium; b-f) pictures of the bilayer actuator immersed in the KCl solution after 3 min, 5 min, 7 min, 9 min and 11 min, respectively; g) the unraveled helical bilayer actuator after 30 min soaking in the KCl solution. (Scale bar represents 1.0 cm in length.)..... 129

Figure C.1. The scheme for the synthesis of hydrogels and the bilayer actuator. The pre-solution was mixed well in a centrifuge tube and poured into a Teflon gasket sandwiched between two glass slides. The solution was irradiated under UV light to polymerize. To fabricate the bilayer actuator, the previous steps were repeated to

polymerize the second hydrogel on top of the first. The afforded bilayer actuator was peeled from the mold and soaked in DI water. 132

Figure C.2. Illustrations of the mechanisms for the actuation and bilayer actuator design. Note: The bilayer actuator taken from the mold did not show any bending before the test. However, after the first cycle, the structure was consistent, showing repeatable two-sides bending. 133

Figure C.3. Pictures of the pNIPAm/p(AAm-co-AAc) bilayer actuator shape changing in one locking/unlocking cycle. The cycle was performed four times; similar behavior was observed. 134

Figure D.1. Pictures of the parts that were optimized. a) The fish flipper with cut openings for easier operations; b-c) the beaded spacing string design that enabled easier adjustment of the effective actuation length (b with short actuation length; c with long actuation length); d) the picture of the 3M VHBTM acrylic tape that was used; e) the Nitinol wire without any coating; f) the Nitinol coil coated with 3M VHBTM acrylic tape. 138

List of Abbreviation

ABP: 4-acryloylbenzophenone
Af: austenite finish temperature
AgNW: silver nanowire
ALCE film: LCE film with an azobenzene mesogens incorporated
Al NPs: aluminum nanoparticles
AMF: alternating magnetic field
AMPS: 2-acrylamido-2methyl-propanesulfonic acid
As: austenite start temperature
BDPPA: 9,10-bis(diphenylphosphoryl)anthracene
BIS: N, N'-methylenebisacrylamide
CVD: chemical vapor deposition
CNT: carbon nanotube
CTE: coefficient of thermal expansion
DC: direct current
DEA: dielectric elastomers actuator
DEAP: 2,2-diethoxyacetophenone
DI water: Deionized water
DMC: dimethylaminoethyl methacrylate methylchloride
DSC: differential scanning calorimetry
 ϵ' : dielectric permittivity
ELPs: elastin-like polypeptides
FEA: finite element analysis
FIB: focused ion beam
FRMMs: field responsive mechanical metamaterials
FWBA: flexible water hydraulic soft bending actuator
GO: graphene oxide
HASSEL: hydraulically amplified self-healing electrostatic
IR: infrared
JPL: Jet Propulsion Laboratories

KPS: potassium persulfate
 LCE: liquid crystal elastomer
 LCs: liquid crystals
 LCN: liquid crystalline network
 LCST: lower critical solution temperature
 Mf: martensite finish temperature
M. pudica: Mimosa pudica L.
 MR: magnetorheological
 Ms: martensite start temperature
 Na-4-VBS: Na-4-vinylbenzenesulfonate
 NdFeB: neodymium–iron–boron
 NIPAm-co-SP-co-AAc: N-isopropylacrylamide-co-acrylated spiropyran-co-acrylic acid
 Nitinol: Nickel Titanium-Naval Ordnance Laboratory
 p(AAc-co-AAm): poly(acrylic acid-co-acrylamide)
 PAAm: polyacrylamide
 PBA: phenylboronic acid
 PC: polycarbonate
 pDADMAC: poly(diallyldimethylammonium chloride)
 pDMAEMA: poly(dimethylaminoethyl methacrylate)
 PDMS: polydimethylsiloxane
 PEG: polyethylene glycol
 PEGDA: poly(ethylene glycol) diacrylate
 PHT: poly(3-hexylthiophene)
 PI: polyimide
 PLA: polylactic acid
 PneuNets: pneumatic networks
 pNIPAm: poly(*N*-isopropylacrylamide)
 p(NIPAAm-ABP): poly(*N*-isopropylacrylamide-co-acryloylbenzophenone)
 poly(AMPS-co-AAm): poly(2-acrylamido-2-methylpropanesulfonic acid-co-acrylamide)

poly (NIPAm-co-AAc): poly (*N*-isopropylacrylamide-co-acrylic acid)

PR: polyrotaxane

PSPMA: potassium 3-sulfopropylmethacrylate

PtTPBP: platinum(II) tetraphenyltetrabenzoporphyrin

PU: polyurethane

PVA: poly(vinyl alcohol)

SEM: scanning electron microscopy

SMA: shape memory alloy

SWBA: strong water hydraulic soft bending actuator

SY: super yellow

TEMED: N,N,N',N'-tetramethyl ethylenediamine

TPU: thermoplastic polyurethane

TTA-UCL: triplet–triplet annihilation-based upconversion luminescence

UCST: upper critical solution temperature

UV: ultraviolet

Chapter 1

Introduction to Biomimetic Actuators

1.1 Biomimicry

For centuries, humans have been fascinated with studying nature and natural processes; this most certainly began out of curiosity, although in many cases it led to a desire for mimicry. The term “biomimicry” originates from the Greek words *bios* (life) and *mimesis* (imitate).¹ Nature has been evolving for at least 3.8 billion years, during which time many creatures have been optimizing themselves to better survive. Many of their functions and characteristics are highly efficient; human beings are not able to emulate this easily.

Biomimicry mostly started from what human beings could not accomplish themselves. For example, people have been dreaming about flying freely like a bird. Early biomimicry of flying dates back to Leonardo de Vinci, an Italian polymath of the High Renaissance.² He dedicated himself in observing birds and their flying. Until 1486, a vast knowledge of flying was acquired through meticulous observations and trial and error, making him a pioneer of biomimicry of birds flying. Later on, more research facilitated the development and advancements of airplanes or other flying objects, such as gliders.

In another example, in 1941, during a hunting trip, George de Mestral found himself covered by the burs from the burdock plant.³ Out of curiosity, de Mestral observed the burs under a microscope and found thousands of tiny hooks on the surface that were able to attach themselves to fabric. Immediately, an idea of a new type of fastener using a synthetic fiber and microscopic hooks struck his mind. With nearly twenty years efforts after his initial idea, de Mestral finally managed to mass-produce his hook-and-loop fasteners. The whole thing became a hit when VELCRO® Brand fastener system was used by a NASA agent who was looking for a way to attach things to the wall while floating.

In yet another example, in 2008 the Japanese automobile company Nissan

announced a bee-inspired car robot BR23C in order to cut the occurrence of car accidents by half.⁴ It is known that bees have 300 degrees of view and have a 99% success rate in avoiding collisions. Nissan developed this 180-degree view car robot using a Laser Range Finder programmed to decelerate cars and perform a 90-degree sharp turn to avoid an obstacle within six feet safety shield radius.

Indeed, there are countless inspirations from nature. Bats and dolphins gave insights on how to develop sonar for military and exploratory applications.⁵ The flippers of humpback whales challenged the notion that rotating blades in turbines and fans should be smooth and straight, which led to the invention of turbine blades that produce 20% more power with less wind (Figure 1.1(a)).⁶ By observing nature and its creatures, more and more inventions are being made to benefit human beings.

However, modern biomimicry is focused on imitating functions or characteristics instead of replicating the entire biological system. For example, an octopus can be smart enough to open the lid of a jar from inside, which involves both complex synergistic muscles and nervous system cooperation. For scientist to understand the mechanism fully and fabricate something this complex is and will remain a difficult task for the foreseeable future. Instead, most biomimetic research is focused on how to achieve specific functions, such as the simple movements of tentacles for grabbing⁷ or swimming applications,^{8,9} even though the mechanisms can be totally different (Figure 1.1(b–c)). It is worth noting that with science or engineering involved, the biomimicry products can be endowed with even more superior properties that the biological systems do not have, for example, the tentacles of an octopus can be made with stronger and more durable synthetic polymers to withstand harsh environments better and have a longer life span.¹⁰ In the aspect of scientific research, biomimicry, a combination of abstraction and simplification of biology, can inspire more novel research ideas that lead to various functions more directly. For research groups with limited resources and instrumentation, biomimetic research can be more accessible and easier to achieve functionalities. The most exciting part of biomimicry is that there are millions of creatures on the earth, aquatic and terrestrial. With all their distinct features and behaviors, there is an enormous amount to learn or imitate, and biomimicry will not reach its exhaustion.

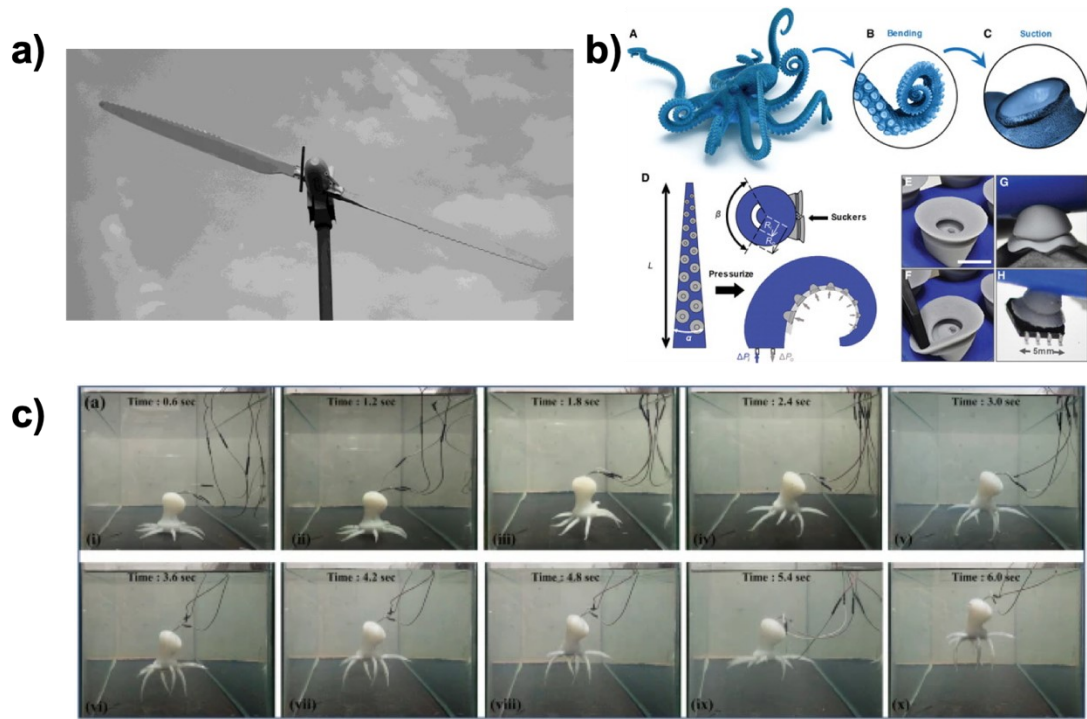


Figure 1.1. a) Wind turbine blades utilizing LE tubercles.⁶ Reproduced with permission from Springer Nature. b) Octopus arm-inspired tapered soft actuators with suckers for improved grasping.⁸ The publisher for this copyrighted material is Mary Ann Liebert, Inc. publishers. c) Taken from the synchronous swimming experiment of Octobot.⁹ Reproduced with permission from Springer Nature.

1.2 Biomimetic Applications

In this section, we will introduce mainly the biomimetic applications from three major aspects in terms of how biomimicry is exploited. The first aspect is information; we can obtain information from the biomimetic applications, for example, we imitate senses to gain information to help us understand the surroundings better. The second is properties; we imitate certain living organisms to optimize our products to achieve similar properties. The third aspect is functions; we design and fabricate devices that can help us accomplish tasks by mimicking the functions of some living organisms.

1.2.1 Information

The first category of biomimetic application is to provide information. Human beings, as well as some other living creatures, have many types of senses, for example, human beings have five basic senses, including sight, hearing, smell, taste, and touch. Any

scientific research products that can provide information on these senses can be regarded as biomimetic applications.

Telescopes, microscopes, and cameras are very obvious biomimetic applications. These devices to some extent imitate how light is transmitted and projected onto eyes so that images can be processed with some improved alterations either to see things that are far away, things that are small, or to record moments. As we know, human eyes are limited due to the photoreceptor cell limitations of humans.¹¹ Our vision was expanded when IR cameras were invented so that things in the darkness could be visualized.¹² The electron microscope, fluorescence microscope, and other improved microscopes really opened the possibilities to observe and study objects that the human naked eye could never see. Recently, the James Webb Space Telescope, a three mirror anastigmat telescope, sent back the first batch of new pictures of space that astonished and excited all humankind.¹³ However, all of these applications only provide images that still require humans to interpret or process. The fascinating thing about human eyes is that it is connected with the brain; the images can be processed, and reactions can be executed immediately. How these instruments can be interfaced with an intelligent system for better interpretation and decision making should be the focus of most biomimetic application researchers. Recently, bio-inspired electronic eyes are emerging as a hot topic for artificial vision systems.¹⁴ In these highly compact systems, high-quality acquisition and efficient processing of massive image data are the basic requirements. Natural vision systems and neural networks for image acquisition and recognition may provide a solution to the challenges, for example, electronic eyes with curved image sensor arrays to simplify the system minimize the size and reduce the weight; neuromorphic in-sensor image processing functions for improved machine vision efficiency (Figure 1.2(a)).^{15, 16} More research should focus on integrating the system to people's everyday life that can be tailored to make decisions and help improve the quality of life.

As is introduced briefly, hearing also is another important sense. However, human beings have limited hearing compared to some other creatures, such as bats and dolphins. By learning from these creatures, human beings were able to develop sonar technology for various applications, for example, topographic survey, ultra-wideband

radar detection of trapped victims in complex environments, and ground penetrating radar for non-invasive investigation.¹⁷⁻¹⁹ The trending for these hearing biomimetic applications is to exploit unmanned vehicle operations with more advanced data processing.²⁰ More importantly, since this area is studied well, artificial intelligence can play an essential role in the advancement of these technologies.

Smell is a very intricate sense, which can perceive and discriminate numerous odors, but it still is acknowledged commonly to be less sensitive than sight and hearing for human beings. The smell perception is triggered when a specific odor binds with specific odorant binding proteins.²¹ The most explored research in this area is an artificial nose for detecting different kinds of molecules that is based on two different mechanisms. The first is an electronic nose, which utilizes a chemical adsorption method to collect molecules. Common electronic noses are arrays of sensors that can provide chemical or physical responses. For example, Gu et al. used a portable electronic nose to extract a flavor fingerprint map of Chinese-style sausage during processing and storage.²² An optimal sensor array was determined and used for evaluation of the lipid oxidation of the sausages. The limitation of the electronic nose is its low sensitivity and low selectivity due to lacking the specific odor receptors. The other type of artificial nose is the bioelectronic nose that is based on olfactory receptor proteins. When the receptors bind with the odor molecules, the biological signal is converted into electrical or optical signals that can be processed by a computer. Thanks to the specific binding mechanism, bioelectronic noses can provide better selectivity and sensitivity, on par with an animal nose. Dacres et al. developed a bioluminescence resonance energy transfer-based biosensor that can detect a volatile ligand at a femtomolar level.²³ Lee et al. fabricated a bioelectronic nose, based on a microfluidic system to detect gaseous trimethylamine using olfactory receptor-derived peptides that can recognize the trimethylamine molecules at a 10 ppt level in real-time (Figure 1.2(b)).²⁴ Once more, for the future advancement of “smell”-based biomimetic applications, the integration between the device and artificial intelligence will be the main difficulty but of great importance. We would like to see the system to work seamlessly in everyday life for quality control and risk management and to perform decision making without human intervention.

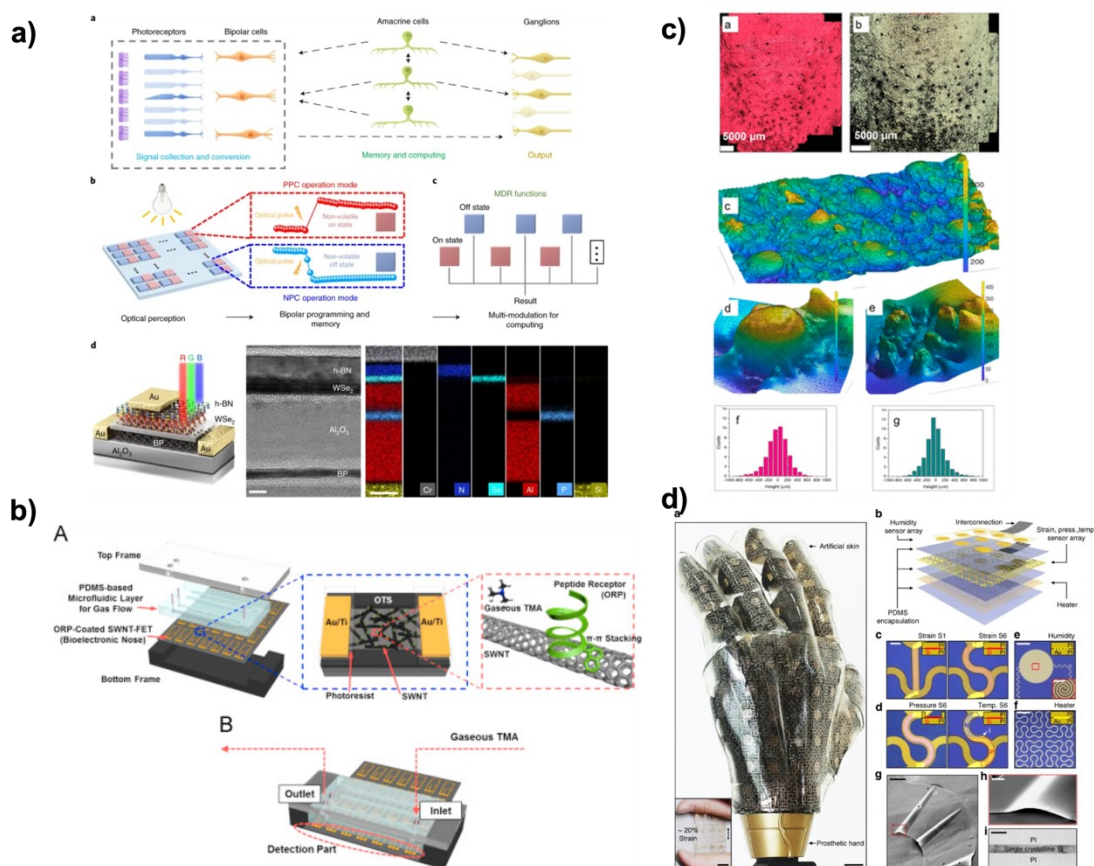


Figure 1.2. a) Retina-inspired 2D retinomorphic hardware for MDR.¹⁶ Reproduced with permission from Springer Nature. b) Schematics of the fabrication process for μ BN and the assembled μ BN used to detect gaseous TMA. Reprinted from Ref.²⁴ with permission from Elsevier. c) Characterization of human tongue surfaces using polymeric impressions. Reprinted from Ref.²⁵ Copyright 2020, American Chemical Society. d) Prosthetic skin based on site-specifically designed SiNR electronics.²⁶ Reproduced with permission from Springer Nature.

Taste is an insufficiently investigated area with not much going on scientifically compared to other senses. The ongoing research is focused on mimicking a tongue and its functions. When tasting food, our tongue can perceive taste and texture with the “taste buds”. Advanced taste sensors were developed, using artificial-lipid membranes, based on concepts of global selectivity and high correlation with human sensory score. Using electrochemistry, the interaction between the lipid membrane and the taste molecules can be quantified by measuring the change of the electrical double layer formed on the charged membrane. As a result, the sensors can quantify more objectively the basic tastes of saltiness, sourness, bitterness, umami, astringency, and richness.^{27, 28} However, the electronic tongues do not resemble the real shape of a

tongue at all. With the development of 3D printing technology, the fabrications of electronic tongues that look like real tongues are possible. Andablo-Reyes et al. 3D printed a tongue-emulating soft silicone surface that resembles the tribological performances of a real human tongue with wettability (Figure 1.2(c)).²⁵ This new technology opened the possibility of using this artificial tongue for food texture tasting applications. If combined with the sensor arrays, this artificial tongue can be used for applications in the food, beverage, and pharmaceutical markets for taste evaluations, quality control purposes, and so much more.

Touch as a sense is very complicated. Human skin can sense touch, force, and even vibration, as well as temperature and humidity. When any of the senses get too strong, the signal can pass through the nervous system to alert the brain of the potential hazards; the brain can send a signal to the body to react and avoid the danger. For example, fingertips are covered by dense touch spots. When a fingertip touches a sharp object, it can sense the pressure and respond quickly to avoid a cut or puncture wound. This is a very important approach for human beings to better protect themselves. Sensory receptors in human skin can transmit tactile and thermal signals from external environments to the brain. The Dae-Hyeong Kim group from Seoul National University has made a lot of progress in researching electronic skins. In 2014, they developed stretchable silicon nanoribbon electronics for skin prostheses (Figure 1.2(d)).²⁶ They fabricated a stretchable prosthetic skin with ultrathin single crystalline silicon nanoribbons that formed strain, pressure, and temperature sensor arrays. The geometries could be tuned to match the target skin segment according to the dynamic mechanical properties. This design provided a high level of spatio-temporal sensitivity and mechanical reliability. In addition, they incorporated stretchable capacitance-based humidity sensors and heater arrays to encompass the moist sensation and body temperature regulation properties. The ultimate goal of the electronic skins to provide actual senses for amputees. The research group tried to relay sensory signals to peripheral nerves. This is and remains a great challenge for future research in electronic skins. Another group that focuses on electronic skins and their integration with the nervous system is the group of Zhenan Bao from Stanford University. The Bao group is focusing on skin-inspired materials, for example, stretchable conductors and

semiconductors, self-healing/tough materials, biodegradable/transient materials, and tissue-level modulus conducting materials.²⁹ With fundamental research on materials, they managed to develop skin-inspired pressure, strain, and shear sensors; e-skin circuits, sensors, and displays; wearable chemical and biological sensors, and research on robotic, implantable, and neuro-interface. Recently, they reported a material design strategy and fabrication processes to achieve stretchable all-polymer-based light-emitting diodes with high brightness, current, and stretchability.³⁰ The diodes can emit red, green, and blue lights with on-skin wireless powering and real-time display of pulse signals. The highlight was to use a light-emitting layer with nanoconfined light-emitting polymer structures formed by spontaneous phase separation from a soft elastomer. They used Super Yellow (SY) as the light-emitting polymer and polyurethane (PU) as the soft elastic matrix. Also, they developed an additive polyrotaxane (PR) on the basis of a water-soluble polyethylene glycol (PEG) backbone and sliding cyclodextrins with PEG methacrylate side chains for a high-conductivity transparent stretchable anode and cathode. This work really laid the foundation for the next-generation stretchable skin electronics and bioelectronic applications. However, there are still great difficulties researchers are facing. Most research groups still are focusing on the optimization of the materials for better electronic skin applications. The ultimate goal is to develop implantable devices and study neuro-interface in depth. Hopefully, challenges in biocompatibility, signal collection, transmission, processing, and artificial intelligence implementation can be solved in the near future. These electronic skins and wearable devices can make human beings reimagine the future and change how people live.

1.2.2 Properties

Biomimetic applications are developing non-stop due to constantly emerging needs from human beings and society. Either out of curiosity or to improve the quality of life, people always want to improve or perfect their existing standard. In this section, we will list a few examples of utilizing biomimicry to add properties to materials or products to improve their performances. Specifically, surface wettability, strong

sucking capability for attachment, and surface smoothness for reduced friction will be discussed.

Our ancestors came up with the idea of wearing clothes mostly just to cover themselves and keep warm. However, nowadays we want more properties for our clothing. Scientists were fascinated by how lotus leaves were able to keep dry in the rain. The impetus to add this water repelling property to our clothing or fabrics to keep them dry and clean galvanized scientists to investigate lotus leaves or plants with similar properties. Superhydrophobic surfaces are extremely difficult to wet, with water contact angle higher than 150° . This property can bring greater convenience to daily life as well as industrial processing. On such surfaces, various phenomena could be inhibited, for example, snow sticking, contamination or oxidation, and current conditions. Lei Jiang's group has been dedicated in superhydrophobicity studies. By observing the structure of lotus and rice leaves, they found that a superhydrophobic surface with a large contact angle and a small sliding angle needs the cooperation of both micro- and nanostructures, as well as the arrangement of the microstructures on the surface (Figure 1.3(a)).³¹ Additionally, they managed to fabricate superhydrophobic films, using polymer nanofibers and differently patterned aligned carbon nanotubes. Apart from the observation on plant leaves, they also took a close look at water striders that can stand and move quickly on water (Figure 1.1(c)).³² Interestingly, they also found a special hierarchical structure of the legs, covered by oriented small hairs with fine nanogrooves. With the understanding of how plants and insects obtain their superhydrophobicity, we can imitate this superior property and use it on our materials and designs. However, hydrophobic surfaces often suffer from being penetrated by micro-/nano-droplets in a high humidity environment that deteriorate the performance of long-lasting hydrophobicity. Tang et al. revealed a dimension character featured as the conical topology and the micro-meter- scaled cylindrical diameter (Figure 1.3(b)).³³ This conical fiber array with a high rp/l (r is the radius; l is the length; p is the apex spacing between fibers) over $0.75\text{ }\mu\text{m}$ generated a big difference in the Laplace pressure due to the asymmetric confined space between fibers. The resulted fibrous structure could propel the condensed dew away due to the generated outward force as well as sustaining the air pocket formed that can be used for underwater aerobic reactions.

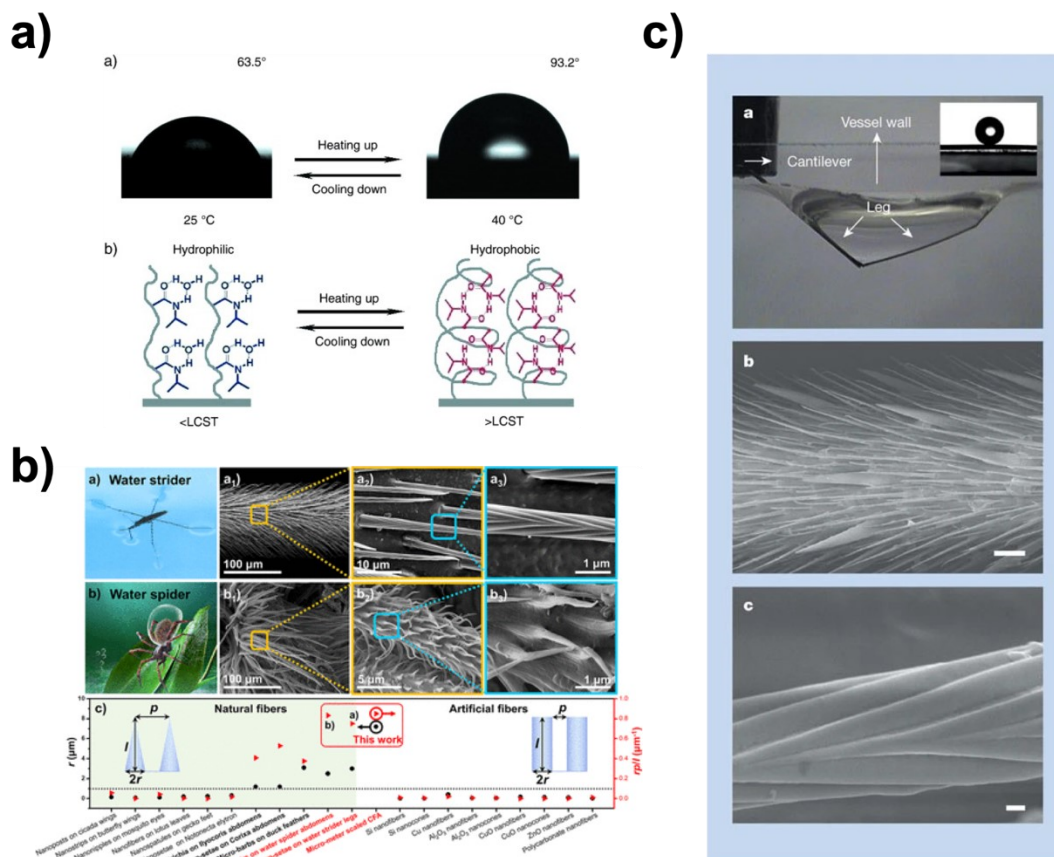


Figure 1.3. a) Thermally responsive wettability for a flat PNIPAAm-modified surface. Reprinted from Ref.³¹ Copyright 2003, John Wiley & Sons, Inc. b) Dimension character of the superhydrophobic fibrous structures of both the water strider's leg and water spider's abdomen. Reprinted from Ref.³³ Copyright 2022, American Chemical Society. c) The non-wetting leg of a water strider.³² Reproduced with permission from Springer Nature.

Sometimes, we want the opposite property of superhydrophobicity, i.e., superhydrophilicity.³⁴ This property can enhance the performance, such as coating and filtering. The original polypropylene film has a poor filtering efficiency due to its hydrophobic nature. However, its wettability can be enhanced greatly with surface chemical modification and nanosized topographical structure construction. Furthermore, we even want the material to be able to switch between superhydrophobic and superhydrophilic. Sun et al. constructed a surface with a pNIPAm coating, a temperature responsive polymer that is hydrophilic when hydrated but hydrophobic when collapsed.³¹ Upon temperature change from 25 to 40 °C the water contact angle increased from $63.5 \pm 2.6^\circ$ to $93.2 \pm 2^\circ$. The detailed mechanism of pNIPAm polymer

temperature response will be discussed later in this chapter. They also managed to change the surface roughness of pNIPAm by introducing groove spacing at $\sim 6\ \mu\text{m}$, which produced the surface wettability switching between $\sim 0^\circ$ and $\sim 150^\circ$ contact angles.

Robots are deployed always by humans to help with tasks that are difficult or dangerous. However, robots are limited themselves in terms of certain properties. For example, it might be a great challenge for robots to navigate a complicated landscape. If robots can climb to scale buildings or creep up windows, the potentials of robots can be expanded enormously. For example, they can access hard-to-reach places, such as skyscrapers, spacecrafts, and bridges, to perform inspections and repairs. Scientists have been getting inspiration from geckos. Cutkosky and his doctoral student, Sangbae Kim from Stanford University, inspected closely the foot of a gecko (Figure 1.4(a)).³⁵ They found that the bottom of its foot is covered by billions of fibers, 200 nm wide. They hypothesized that a weak intermolecular attraction, known as the van der Waals force between the fibers and the surface enabled the attachment and climbing. Moreover, this adhesion is directional, which supported the gecko by exerting an upward force but can be released when the gecko moves its foot. To achieve this “sticky” property, the researchers fabricated polymer patches that had 30 μm wide stalks, which were angled and had oblique tops (Figure 1.4(b)).³⁶

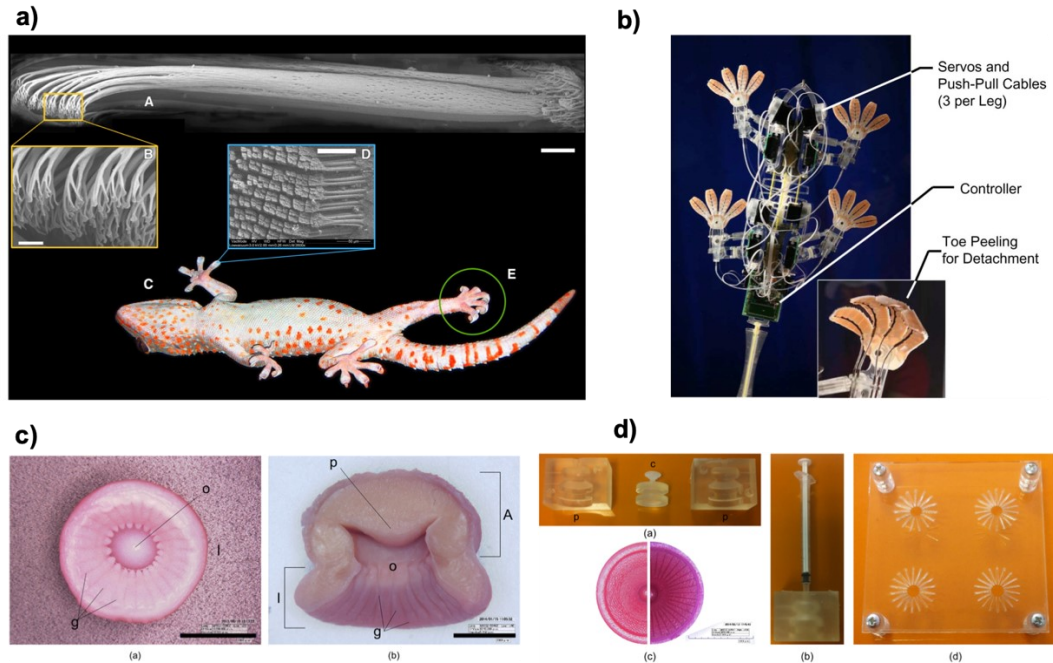


Figure 1.4. a) Gecko adhesive system. Reprinted with permission from Ref.³⁵ Copyright 2006, COMPANY OF BIOLOGISTS LTD. b) Stickybot, a new bioinspired robot capable of climbing smooth surfaces. Inset: detail of toes curling to facilitate detachment. Reprinted from Ref.³⁶ Copyright 2008, IEEE. c) Photographs of *O. vulgaris* sucker. d) (a) Resin mould used to produce suction cups. The mould consists of three components: two specular external elements, p, and an internal core, c. (b) Sealed mould during liquid silicone pouring. (c) Suction cup prototypes before and after engraving. On the left, the surface of the infundibulum is completely smooth; on the right, the engraved geometry is visible. (d) Plexiglas masks used to flatten the infundibular surface during engraving. c&d were reprinted with permission from Ref.³⁷ Copyright 2015, IOP Publishing Ltd.

Another example is octopus' suckers that use a different adhesion mechanism. The attachment feature resulted from the softness of the sucker tissue and its surface morphology. Octopus suckers have a series of radial grooves that can increase the area for pressure reduction. Tramacere et al. characterized the artificial suction cups fabricated from casting and subsequent laser cutting (Figure 1.4(c–d)).³⁷ They found that an engraving treatment enhanced the attachment and the geometry that resembles the octopus performed the best.

Another property that scientists tried to imitate is the drag reduction property of shark skin. Most importantly, scales with V-shaped central ridges were found on the surface of pectoral fins of a number of fast swimming shark species.³⁸ It is acknowledged that these ridges reduced water drag. Furthermore, shark scales can act as longitudinal vortex generators, causing bulk fluid to mix and the thickness of thermal boundary-layer to reduce, which can improve the swimming performance. It is worth

noting that on the skin of sharks, a thin layer of mucus also was considered to reduce the drag. When designing fabrics or materials with a drag reduction property, researchers also will consider modifying the surface hydrophobicity to mimic a similar mucus drag reduction property. This is a very good example of scientists combining different techniques and mechanisms for perfecting the performance of materials and products.

1.2.3 Functions

One of the most fascinating traits of living organisms is movement. Especially for human beings, motion is the key to accomplishing tasks. Ultimately, scientists are interested in mimicking the motion functions of living organisms to help people achieve tasks that are either tedious or dangerous. As a result, there are function-oriented biomimetic applications emerging, in particular, products that can help do work such as moving, lifting, grabbing, and rotating. This will be discussed in detail in the following section.

1.3 Biomimetic Actuators

Actuators, sometimes called artificial muscles, by definition, are materials or devices that can perform physical motion upon certain stimuli, for example, electricity, temperature, magnetic fields, and different chemicals. In some sense, actuators can be regarded as biomimetic actuators in a general way due to the motion movements of the device resembling living organisms.

1.3.1 Materials

Conventionally, actuators are made of rigid structural materials, mainly metal, metal composites, and plastics, and they are powered by electricity or pressurized fluids. These actuators primarily mimic the moving behaviors of living organisms. In 2003, researchers at NASA Jet Propulsion Laboratories (JPL) and Caltech developed a series of minimalist jumping robots called “Hoppers” for celestial exploration.³⁹ The actuators can control the steering, hopping, and self-righting motions with the assistance of on-board cameras. Vertical hopping motions are generated by the release

of a simple linear spring with compression and decompression cycles. One simple metal material, bistable metal strip, is worthy of some detailed introductions in this section. It is seen mostly in a kid's toy-slap (snap) bracelet, which was invented by Stuart Anders, a Wisconsin teacher in 1983.

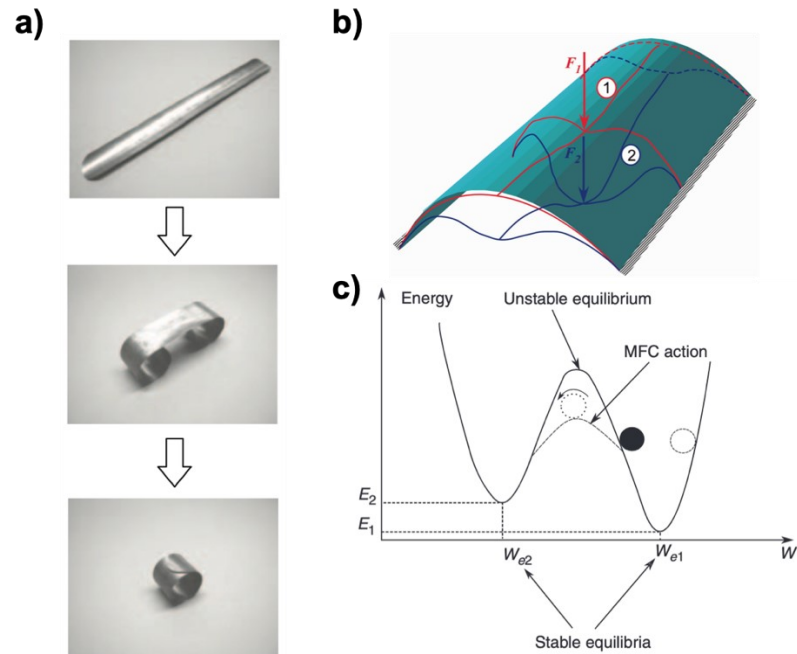


Figure 1.5. a) Metal “slap bracelet”. Reprinted from Ref.⁴⁰ Copyright 2006, ASME. b) Localized buckling under increased loads ($F_2 > F_1$). Further increasing of the localized load may lead to a complete curvature reversal. Reprinted from Ref.⁴¹ Copyright 2019, SAGE Publications. c) Potential well schematic diagram for a bi-stable plate under the action of an MFC actuator. Reprinted from Ref.⁴² Copyright 2011, SAGE Publications.

The slap bracelet is made of a bistable metal strip wrapped by some fabrics to prevent a cut injury. The core of the bracelet is the bistable metal strip, which is a piece of carbon steel or flexible stainless steel. When the strip is straight, it looks like a shallow trough (Figure 1.5(a)). However, it becomes a coiled flat band when curled up. Just like the Venus flytrap plant, the bistable metal strip exhibits a snap-through behaviors between the straight and curled states. A lot of research was done to study the bistability. Chen and coworkers developed a theoretical framework to addresses quantitatively the large deformation of shell structures with geometric nonlinearity, using differential geometry, elasticity theory, and variational principles.⁴³ They found out that only when the plane is wide and thin enough does bistability start to manifest,

and the system assumes a nearly cylindrical shape (a shape with nearly zero Gauss curvature that can reduce the total potential energy). On the other hand, the principal driving forces (surface stress) in the two perpendicular directions need to bear different signs. A lot of researchers sought solutions with the help of finite element analysis (FEA) to broaden the scope of their studies in terms of different boundary and loading conditions^{44, 45} as well as different materials (Figure 1.5(b))⁴¹ and geometries.⁴⁶ For the bistable metal strip, when it is straight in the long direction, a curvature forms in the short direction to keep the Gauss curvature near zero. Due to the surface stress lateral to the surface, which means no net driving force for the strip to curl, the strip remains stable in the straight form. If an external force is large enough to deform any point of the strip (critical displacement (Figure 1.5(c))⁴²) that induces curvature changes or inflection points,⁴¹ causing the surface to flatten in the short direction; a curvature will form in the long direction to minimize the potential energy.⁴⁷ This will render the surface stress to be out of the plane in the long direction, causing the strip to translate the curling towards the whole piece, which is a snapping behavior. The idea of using a small external force to cause a strong snapping without the need of a continuous energy input inspired a lot of novel designs for actuators.^{48, 49} However, hard actuators must be positioned accurately to perform their tasks due to the noncompliant materials, and they are generally not able to adapt autonomously to different shapes or specific tasks. Elastomeric materials, on the contrary, are compliant and easy to manipulate.

With the novel development of soft materials, biomimetic actuators started to adopt various of soft components, such as hydrogels, which added tissue-like softness that resembles actual living organisms' texture. Soft actuators are different from their hard counterparts, intellectually and technologically, mainly due to different objectives, uses, and mechanisms. The Whitesides group took advantage of soft elastomers by pressurizing embedded pneumatic channels and designed and developed a soft gripper, using silicone elastomers polydimethylsiloxane (PDMS) and Ecoflex 00-30.⁵⁰ Due to the difference in the material mechanical properties and channeled/layered design, the gripper could be actuated pneumatically to perform bending, curling, and gripping movements. The compliant grippers, just like human hands, could even handle fragile

objects (e.g., a chicken egg), which could be an extremely difficult task for hard actuators.

1.3.2 Sizes

In terms of sizes, biomimetic actuators range from microscopic sizes to macroscopic sizes. Fabricating actuators with small sizes such as a submicron-size can be challenging. The common approach is a top-down process, which means to start with larger objects and break them down to smaller pieces.⁵¹ Zakharov et al. fabricated successfully a microscale-sized functional bilayer composite material with a shape memory effect, using focused ion beam-assisted (FIB) milling for fabrication of shape memory alloy (SMA) cantilevers and ion-assisted chemical vapor deposition (CVD) for deposition of a platinum elastic layer.⁵² They also demonstrated that the microactuator can be used as micromechanical nanotweezers for manipulation of submicron- and nano-sized objects by pick up a CNT bunch. Compared to hard materials, microscale actuators based on soft elastomers are easier to make using soft lithography technique. Buguin et.al. utilized a soft lithography, called replica molding, and created micron-sized responsive pillars made of nematic liquid crystal elastomers.⁵³ They applied an oriented magnetic field onto the nematic mesophase and polymerized the network to afford pillars that can change their lengths in response to temperature.

1.3.3 Mechanisms

Biomimetic actuators have been developing rapidly. Actuation mechanism is the key to the successful designs and applications. The focus in this area is on exploiting different mechanisms (traditional and novel) and combining them to realize more novel and useful designs for various applications. In this section, we will focus on discussing different mechanisms, listing examples, and providing thoughts and insights on each.

1.3.3.1 Temperature

One of the most common mechanisms for actuating actuators is through temperature change. The most obvious reason is the simplicity of inducing a temperature change.

Different metals have different thermal expansion coefficients. The coefficient of thermal expansion (CTE) refers to the rate at which a material expands with an increase in temperature.⁵⁴ Early in the eighteenth-century, a clockmaker named John Harrison made a marine chronometer (H3) to compensate for temperature-induced changes in the balance spring.⁵⁵ Charles Édouard Guillaume, a Swiss physicist, received the Nobel Prize in Physics in 1920 in recognition of his discovery of anomalies in nickel steel alloys.⁵⁶ The near-zero coefficient of thermal expansion made it useful for constructing precision instruments whose dimensions should not change in various temperature conditions.

When pieces of metal strips with different CTE are bonded together (usually welded) flat, the strip can bend one way if heated or the other way if cooled.⁵⁷ By utilizing this bending behavior, a temperature change can be converted into a mechanical displacement, which can be harnessed for actuation purposes. Typically, the bimetallic strips are used in thermostats. A bimetallic strip is used as a switch between electrical contacts. When the temperature changes, the strip bends and touches the electrical lead that turns on/off the heating elements. Moreover, the bimetallic strip can be used in a safety shutter mechanism to release the spring-loaded shutter when the temperature exceeds the maximum safe value.⁵⁸

A shape memory alloy is another material that has received a lot of attention. The most well-known shape memory alloy that can respond to temperature change is Nitinol (Nickel Titanium-Naval Ordnance Laboratory).⁵⁹ Its properties were discovered by William J. Buehler and Frederick Wang during research at the Naval Ordnance Laboratory in 1959. Nitinol has a solid-to-solid phase transition that produces its unusual properties that are used in numerous practical applications in cardiovascular surgery, orthopaedics, orthodontics, safety products, eyeglass frames, and toys.^{60, 61} Its interesting property and behavior also incited novel inventions and applications, making perfect lecturing material both in class and laboratory.

The shape memory property of Nitinol is a result of certain basic atomic structural characteristics. When in the higher temperature regime, the atoms adopt an ordered solid-state phased-austenite (B2), while at a lower temperature, the atoms can move locally into a complex, new atomic arrangement or phase–martensite (B19')

(Figure 1.6(a)).^{62, 63} The austenite/martensite transitions can be induced by a temperature change or an external stress. With the reversible phase change, a shape memory cycle can be realized. Using Nitinol wire as an example, at a low temperature environment, Nitinol adopts the martensite structure that is ductile and easy to deform. The wire can be bent or twisted into some random shapes. When the temperature is increased and reaches the phase transition temperature of Nitinol, the atomic structure starts to change from martensite to austenite that is difficult to deform. As a result, the Nitinol wire recovers to the original shape slowly. When the phase transition finishes, the shape will be recovered fully. If the temperature is lowered to below the phase transition temperature, the austenite structure will change to martensite again, making the Nitinol wire ductile and ready for the next deformation cycle.

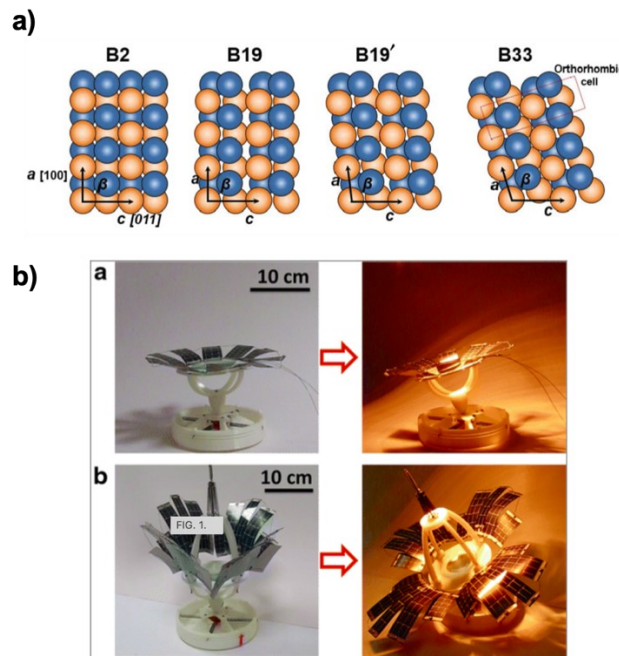


Figure 1.6. a) Atomic structures of the cubic B2, orthorhombic B19, monoclinic B19', and orthorhombic B33 NiTi phases with the monoclinic angle (β) and the lattice constants (a and c) indicated. Ni and Ti atoms are represented by blue (dark gray) and orange (gray) balls, respectively. Reprinted from Ref.⁶⁴ Copyright 2015, American Physical Society. b) Systems exhibiting heliotropism and nyctinasty. Reprinted with permission from Ref.⁶⁵ Copyright 2018, Mary Ann Liebert, Inc.

It is worth noting that there are many ways of bringing a temperature change to facilitate the phase transition, for example, a hot water bath, hot air from a heat gun, or Joule heating by applying electricity.⁶⁶ Despite the fact that different approaches are

feasible, the ultimate goal is to bring the temperature above the phase transition temperature. Baytekin et al. developed a completely autonomous biomimetic plant that can perform diurnal cycles of sun tracking (heliotropism) and leaf opening (nyctinasty) (Figure 1.6(b)).⁶⁵ The biomimetic actuator did not contain electronics, instead, it relied on an in-built optomechanical feedback to control the plant-like movement. They came up with a design comprising a three-dimensional printed body and a stem connected to and supported by radially oriented pre-stretched nitinol springs. When the light was irradiated onto the unbent stem, the light was focused by the lenses to the spot near the center of one of the springs. The spot of the Nitinol was heated and contracted, bringing the whole plant slanted toward the light. As a result, the plant was stabilized in the position facing the light source. They took a step further by incorporating Nitinol wires to control the solar panel leaves that exhibited nyctinastic motions. The final biomimetic actuator mimicked the phenomenon in real plants with even faster sun-tracking motions. Autonomous feedback elements still are challenging for biomimetic actuator systems, and it should be the focus of all researchers in order to advance this research area further.

Temperature-responsive soft materials also received enormous interests. The most commonly studied polymer is poly (N-isopropylacrylamide) (pNIPAm). pNIPAm has a lower critical solution temperature (LCST) at around 32 °C.^{67, 68} When the temperature is above the LCST, pNIPAm transitions from an extended state to a collapsed state reversibly, accompanied by an exclusion of water from the hydrated pNIPAm (Figure 1.7(a)).⁶⁹ PNIPAm also can be crosslinked chemically or physically to form microgels or hydrogels that also exhibit swollen-to-collapse transitions. This process induces a large volume change of the material, which is of great interest for actuators. Li et al. generated a bilayer gripper that can exhibit a bidirectional bending behavior (Figure 1.7(b)).⁷⁰ The authors synthesized a layer of water swellable pNIPAm hydrogel on top of a non-water swellable polydimethylsiloxane (PDMS) layer. In the pNIPAm hydrogel layer, poly(diallyldimethylammonium chloride) (pDADMAC), a polycationic polymer was added, which greatly increased the water absorption content. When the temperature is below the LCST, the bilayer gripper bends toward PDMS side due to hydrogel hydration, while bending toward the pNIPAm hydrogel side when the

temperature is higher than the LCST due to the hydrogel losing water. They demonstrated successfully that the as prepared bilayer gripper can grab a plastic bead from cold water and release it in hot water.

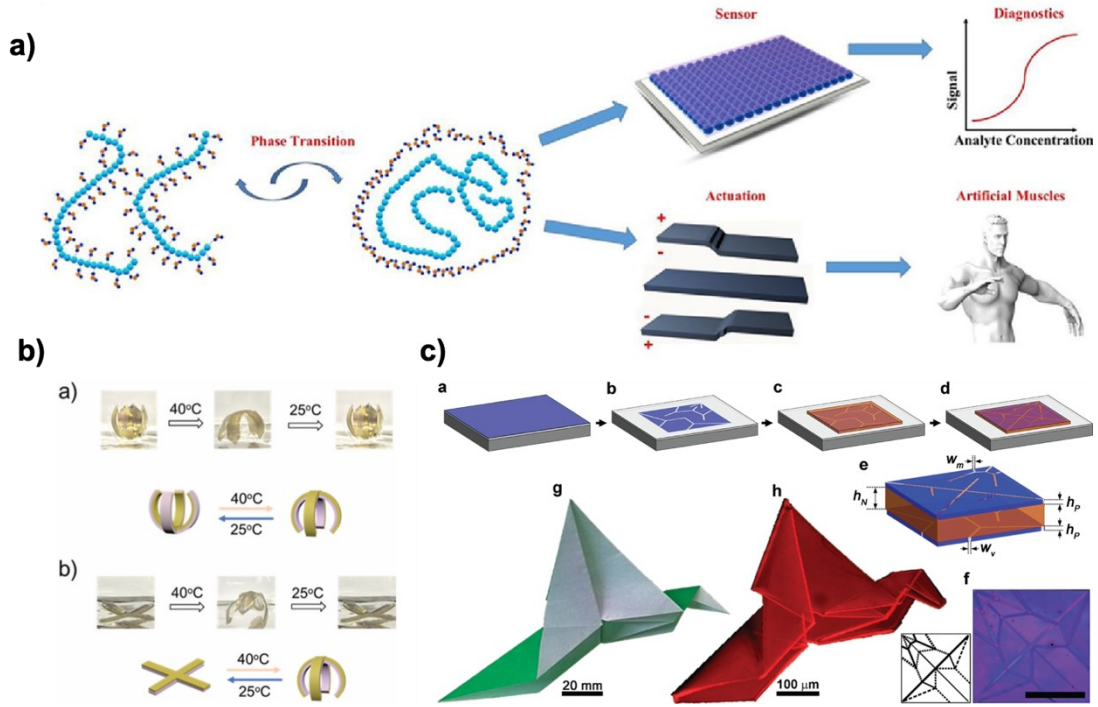


Figure 1.7. a) Graphical illustration of pNIPAm used for sensing and actuation purposes. Adapted from Ref.⁶⁹ Copyright 2021, Elsevier B.V. b) (a) Actuation of the pNIPAm-pDADMAC hydrogel/PDMS bilayer system; (b) actuation of the pNIPAm hydrogel/PDMS bilayer system. Reprinted with permission from Ref.⁷⁰ Copyright 2017, Royal Society of Chemistry. c) Fabrication of self-folding polymer origami. Reprinted with permission from Ref.⁷¹ Copyright 2014, John Wiley and Sons, Inc.

Breger et al. photopatterned a gripper that is composed of a continuous layer of a temperature responsive poly (NIPAm-co-AAc) hydrogel layer and a segmented layer of stiff polypropylene fumarate.⁷² This combination can endow the actuator with enough mechanical property to be used in the application of cell excision. However, this actuator is limited to only one mode of actuation, folding and unfolding, which greatly restricted the applications that require complicated actuations. Na et al. provided a solution to this problem by fabricating a trilayer structure origami (Figure 1.7(c)).⁷¹ They sandwiched a layer of a temperature-responsive pNIPAm hydrogel between two layers of rigid poly(p-methylstyrene) polymers and introduced open stripes with different widths on them during the photolithography fabrication process.

Due to the different swelling properties between the pNIPAm hydrogel and rigid polymers, the trilayer structure can fold according to the predesigned stripes pattern, such as a Randlett's flapping bird. The bird can fold when the temperature changes from 55 °C to 22 °C; it can return to a flat sheet when heated to 55 °C with good reproducibility.

Increasing the temperature for actuation can be a problem for some application scenarios, such as protein and cells. Hu et al. reported a cooling triggered shape memory actuator which can recover the preprogrammed shape when the temperature is lowered.⁷³ They polymerized acrylamide with the presence of linear methylcellulose, N, N'-methylenebisacrylamide as crosslinker. The hydrophobic methoxy groups of the methylcellulose can be hydrated in water at a lower temperature and can aggregate at a higher temperature due to entropy driven aggregation; this is similar to the pNIPAm LSCT property. The hysteresis between the temperature ramping and hydrogel modulus change suggested the potential realization of multi-stage shape memory actuation. By programming a two-step fixation at different temperatures, the authors can recover a stepwise actuation at different positions when they lower the temperature to different levels. Protein and cells can tolerate a low temperature rather than a high temperature. This cooling triggered actuation can circumvent the high temperature required in most shape memory actuators and will be of great importance for in vivo applications. However, the problem with this system is that it needed an external force to complete a shape fixation and could undergo actuation only once. More designs and research are needed to improve the system.

Isotropic pNIPAm hydrogel-based temperature-responsive actuators have a notorious problem, slow actuation. Because the volume change of the hydrogel is due to the absorbing and expelling of water molecules into or out from the polymer network, the response speed is limited by the diffusion of water. To improve the responsivity of hydrogel actuators, the common concept is to introduce channels or porosity to enhance the water exchange speed. Jiang et al. fabricated a bilayer actuator by electrospinning an active polymer layer of poly(N-isopropylacrylamide-co-acryloylbenzophenone) (p(NIPAAm-ABP)) onto a passive layer of thermoplastic polyurethane (TPU) with the presence of photo-crosslinker (4-acryloylbenzophenone,

ABP).⁷⁴ Electrospinning of the polymers greatly increases the porosity and surface area, which speeds up water transportation. The bilayer actuator can respond and curve fully within one second. However, the actuator does not show bi-directional folding. The authors attributed this unusual behavior to the anisotropic property of the electrospun fibers. The swelling of the polymer at a temperature lower than the LCST counteracts the contraction resulting from the relaxation of polymer chains into coils.

Heating up the temperature-responsive actuators in a water medium is the most direct method. However, this direct heating method cannot offer fast, local, or remote heating, which largely limits the applications. As a result, two main types of indirect heating methods were developed; one is electrothermal conversion by Joule heating, the other is photothermal conversion. Since the actuation mechanism is related to electricity and light, the discussion here also applies to those sections that are discussed later in the chapter.

Electrothermal conversion is an easy and convenient way to introduce heat to the actuators. However, many designs require an electrolyte that can be activated only under extremely high voltage, which is not efficient and practical. Yao et al. came up with a design using silver nanowires (AgNW) as heaters and achieved fast actuations.⁷⁵ They drop-casted silver nanowires onto a silicon substrate through a mask. Then, polydimethylsiloxane (PDMS) was spin-coated on to the AgNW film and peeled off from the substrate. Commercially available polyimide (PI) tape was attached onto the PDMS film on the side with AgNW. A maximum heating rate of 18 °C/s, and a cooling rate of ~20 °C/s can be achieved with a driving voltage as low as 4.5 V. The assembled actuator can undergo a maximum bending angle of 720° due to different thermal expansion coefficients between PDMS and PI. A soft actuator as a self-walker and a four-finger gripper were made successfully and exhibited good stability and reproducibility.

Remote manipulation has been a hot topic recently. Operating the actuators without direct contact can accomplish tasks that were not possible for in vivo or biomedical applications. Even though electric wires also can transduce the electric stimuli to further space, the deployment of the wires can still be a problem and is not practical in many cases, for example, in the human blood stream. The alternative

approach is a photothermal conversion where photons are converted into heat. Many research groups are utilizing this method to realize remote actuation for temperature-responsive actuators. Graphene, carbon nanotubes (CNT), and other carbon nanomaterials have superior optical, thermal, electrical, and mechanical properties. Therefore, these materials often are composited into other materials to enhance their performance. Utilizing the photothermal conversion effect of carbon nanotubes, Hu et al. fabricated a jumping robot that mimicked the motion of a human finger flickering.⁷⁶ A bilayer structured roll of CNT and PDMS was made by a simple heating method. Upon exposure to light, the CNT layer heats up the actuator due to the photothermal conversion effect. The thermal expansion coefficient difference between CNT and PDMS causes the opening of the roll. However, the two ends of the roll were stacked, and an opening behavior was hindered. When the accumulation of energy overcomes the friction, about a 21 mm height jumping of the roll was achieved due to the abrupt release of energy.

Graphene and other carbon nanomaterials also were incorporated directly into a temperature responsive pNIPAm hydrogel network to improve the mechanical strength and temperature responsivity. However, most methods disperse graphene directly into the monomer solution in order to establish a great interaction with the polymer network, which might restrict the polymer chain motion. Qiu et al. came up with a design, using highly structured graphene aerogel as a foundation.⁷⁷ By infiltrating and crosslinking a monomer solution into the aerogel in vacuum, the temperature responsive hydrogel can have better mechanical and electrical properties while retaining the responsivity.

Contrary to LCST polymers, UCST polymers exhibit volume expansion when the temperature is increased.^{78, 79} The most typical UCST is the interpenetrating network of polyacrylamide and polyacrylic acid. Due to hydrogen bonding between acrylamide and acrylic acid, the networks interact with each other. When the temperature increases, the hydrogen bonds break and allow the network to be solvated. Zheng et al. generated a bilayer structured actuator by combining poly(acrylic acid-co-acrylamide) (p(AAc-co-AAm)) hydrogel with UCST and pNIPAm hydrogel with LCST (Figure 1.8).⁸⁰ When the temperature is lower than the LCST and the UCST, the

pNIPAm hydrogel holds a large amount of water, while the p(AAc-co-AAm) hydrogel layer could not be due to the hydrogen bonding within the polymer chains. This resulted in curvature toward UCST hydrogel side. However, when temperature is increased above the LCST and the UCST, the LCST hydrogel collapses and the UCST hydrogel gets solvated, which leads to the opposite phenomenon, the hydrogel bilayer bends toward the LCST hydrogel. By switching the temperature, the bilayer actuator curves towards different directions, similar to the behavior of the *Mimosa Pudica* plant.

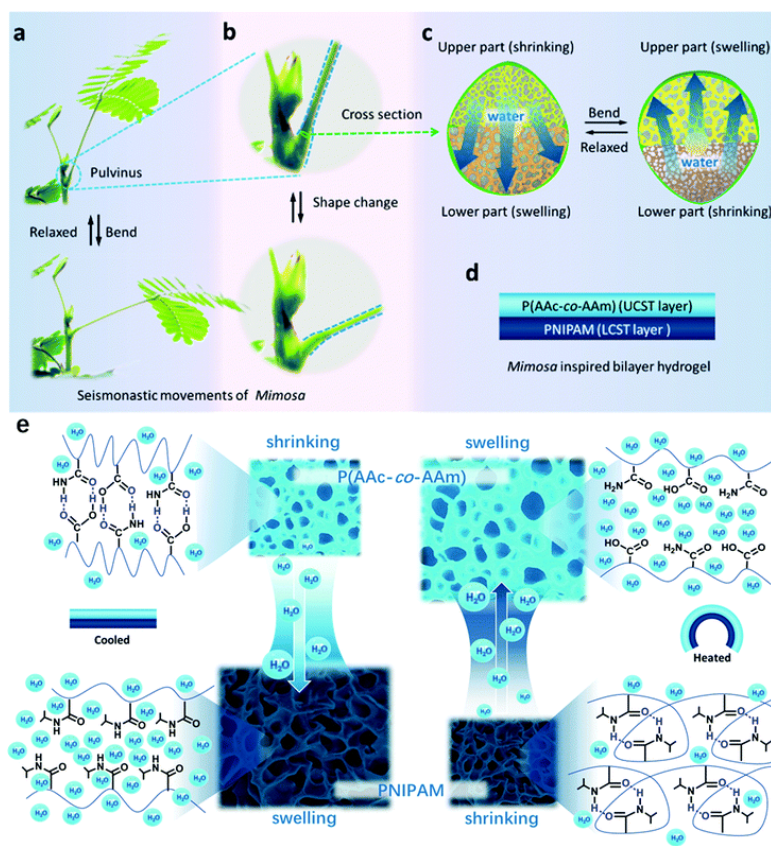


Figure 1.8. (a) The petiole of mimosa bends downward after being touched. (b) The mechanism of the motion is based on a swelling of the upper part of mimosa's pulvinus, while the lower part shrinks. (c) The shape change of the pulvinus is mainly induced by the directional water transfer between the lower part and the upper part because of a change of osmotic pressure. (d) Imitating the actuation of mimosa, a bilayer hydrogel consisting of a PNIPAM layer on top of a P(AAc-co-AAm) layer is fabricated to function in open-air. (e) At low temperature (15 °C), the PNIPAM layer is swollen by water. Increasing the temperature to 40 °C leads to a shrinking of the PNIPAM layer, and directional water transfer to the P(AAc-co-AAm) layer that consequently swells and as a result lets the bilayer hydrogel bend. Reprinted with permission from Ref.⁸⁰ Copyright 2018, Royal Society of Chemistry.

Due to the possible manipulation of the functional entities by genetic alteration, protein-based polymers also can be using in biological applications. Wang et al. created

a temperature responsive hydrogel actuator composed of graphene nanosheets and elastin-like polypeptides (ELPs).⁸¹ They first functionalized graphene nanosheets with their synthesized ELPs with an anchor to the graphene surface. Then, the network was crosslinked in the presence of water to introduce inhomogeneity across the depth. The exposed surface was confirmed to have a higher porosity due to a water vapor-induced phase separation. When the temperature is increased, ELPs will shrink and expel water from the network, resulting in a change in volume. The porosity difference across the depth provided the hydrogel actuator with the ability to bend. Due to the photothermal conversion endowed by graphene, many different modes of actuator are possible, for example, a finger-bending hand, a laser directed folding hydrogel, and a light driven crawler.

A liquid crystal elastomer (LCE) is another temperature responsive material. It encompasses the elasticity of elastomers and the ordered orientation of liquid crystals.⁸² When the temperature changes, the orientation of the liquid crystals changes and results in volume changes. Xing et al fabricated a temperature responsive actuator that can bend with a color change upon temperature variations.⁸³ They deposited a 3D-structured SiO₂ photonic crystal onto the glass substrate, infiltrated it with LCE monomers, and crosslinked the network with UV irradiation at 5 °C to keep the LCs at a nematic phase. After they were peeled off from the glass substrate, the composite film was tested by changing the temperature. When the temperature is increased (> 123 °C), the nematic phase orientation was disturbed, resulting in a lateral shrinkage. The shrinking of the LCE layer caused the film to bend towards the LCE layer as well as a stretching in the opal PC layer. As a result, the lattice distance decreased and caused a blue shift of the photonic band gap. However, the drawback of this temperature responsive actuator is that it requires a very high temperature for the actuation, which greatly limits its potential applications.

Viscosity change in a polymeric material results from chain movements.^{84, 85} Shape memory effect happens when crystalline phases exist. When the material is heated above the thermal transition temperature, the crystalline regions can soften and deform upon an external force. The shape can be locked temporally when the temperature is lowered, but recoverable when it is heated above thermal transition

temperature again. Michal et al. synthesized semi-crystalline polydisulfide networks that worked as shape memory adhesives.⁸⁶ To test the shape memory actuation of the polymer, they placed the material between two glass slides in a lap joint. The top slide was rotated when heated at 80 °C; it was locked in the position when cooled down. When the material was heated up to 80 °C the top slide rotated and recovered to its original position due to the elastic energy stored.

1.3.3.2 Electricity

When talking about actuators and robotics, electricity is used mostly as an energy source to power the motors to facilitate the movement of parts of the device. However, electricity as an actuation mechanism is still receiving enormous attention due to its easy application and fine-tune capability through the magnitude of applied voltage and its waveform. In 2000, Pelrine et al. demonstrated that an acrylic elastomer can produce an actuation strain of 215% when a $128 \text{ V } \mu\text{m}^{-1}$ voltage is applied.⁸⁷ After that, more and more research on dielectric elastomers emerged. Even though electricity is an easy stimulus for actuation, the biggest problem is that high voltages are required for most of them. This limitation led to a lot of research on optimization of the dielectric elastomers, for example, introducing polar groups (e.g., nitrile groups and trifluoropropyl groups), high permittivity ceramic fillers, and/or conductive nanofillers into on dielectric elastomer actuators (DEAs) to increase dielectric permittivity (ϵ'). Carpi et al. managed to blend a poly(dimethylsiloxane) (PDMS)-based rubber with an undoped poly(3-hexylthiophene) (PHT) at 1–6 wt%, which resulted in an increase in ϵ' and a decrease in Young's modulus.⁸⁸ For dielectric elastomers to be used for underwater actuation, such as robot fish or jellyfish can be challenging due to the high voltage requirement. Shintake et al. provided a solution to this problem.⁸⁹ They developed a soft biomimetic robotic fish, based on DEAs. The method consists of laminated soft silicone layers, ensuring the insulation of the high-voltage DEA electrodes for safe actuation operations. It is noted that the DEA electrodes on the groundside are, instead, exposed to the surrounding water, making the fabrication process much simplified. They fabricated a robot fish consisting of four silicone elastomer layers: two uniaxially pre-stretched DEAs sandwiching a body made of two

silicone layers, forming an antagonistic configuration. The robot shape is straight when unactuated due to the two DEAs that are equally pre-stretched. Once each DEA is actuated periodically and sequentially, the recoil motion of the tail can generate an undulating fish-like motion, propelling the body to move forward. DEAs are driven by high electric fields, prone to failure from dielectric breakdown and electrical aging. If the optimization work can be implemented in the underwater biomimetic actuator design, a much lower voltage and a less demanding power source will be required, thus a lower energy consumption could be achieved for safer actuations.

Hydrogels also are popular candidates for actuators, using electricity as the actuation mechanism due to their lower driving voltage (<10 V). The hydrogels are actuated to undergo shape morphing due to the migration of ions inside the hydrogel network in the applied electric field. Migliorini et al. developed an electro-responsive hydrogel based on Na-4-vinylbenzenesulfonate (Na-4-VBS).⁹⁰ The actuator was able to actuate at low voltage (0.2–5 V) in a NaCl aqueous solution. The hydrogel deformation resulted from free ionic species migration throughout the polymer, which was a dynamic osmotic equilibrium that happened at the interface between the polymer and the aqueous medium. Specifically, when an electric field was applied, cations drifted toward the cathode through the hydrogel that resulted in a concentration decrease of cations at the anodic side. An osmotic pressure build-up between the boundary and the anodic side of the hydrogel induced the actuator to swell. Meanwhile, inverse osmotic pressure that occurred at the cathodic side induced swelling. The cooperative effects rendered the hydrogel to bend toward the cathode. The interesting part about this research is that the bending behavior also was observed in environments, which offers the possibility to use this as a tool for remote surgical operations or micro-robots in physiological systems.

Biomimetic actuators using hydrogel as artificial crawlers, artificial fishes, and mechanical hands were developed. Yang et al. developed soft hydrogel walkers with an electro-driven motility (Figure 1.9).⁹¹ The hydrogel walkers with an arc looper-like shape with two “legs” consisted of polyanionic poly(2-acrylamido-2-methylpropanesulfonic acid-co-acrylamide) (poly(AMPS-co-AAm)). The authors utilized the gradient distribution crosslinking density that resulted from the attenuation

of UV light strength to afford this initial bending shape. The polyanionic hydrogel can bend toward the cathode in electrolyte solutions quickly. By controlling the electric field, the walker can walk on the rough surface even with heavy cargos 25 times heavier that of the walker at the dried state.

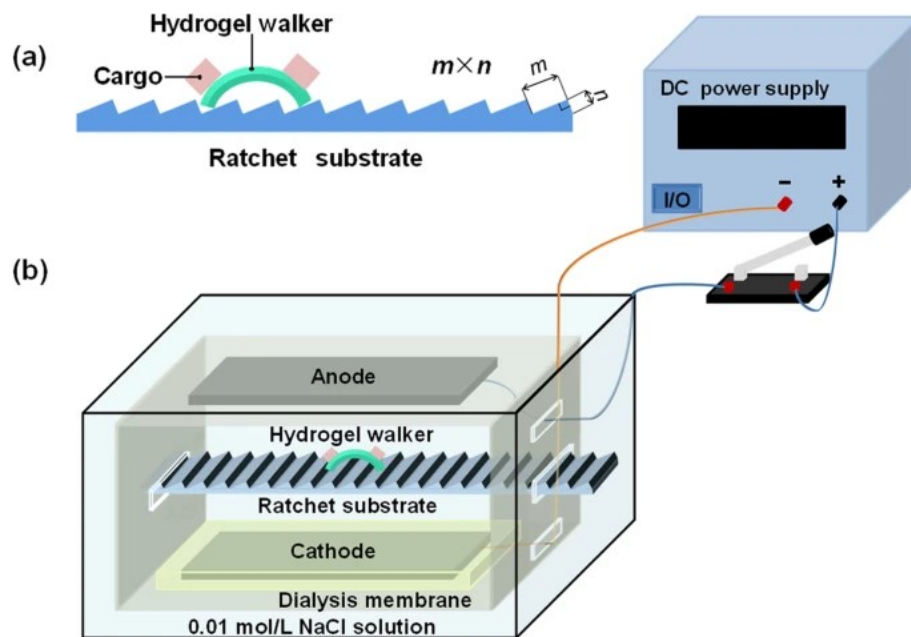


Figure 1.9. Setup for achieving and observing the electro-driven motility of cargo-loaded hydrogel walker. Reprinted from Ref.⁹¹ Copyright 2015, Chao Yang et al.

In order to enhance electroresponsivity, nanomaterials were used, which also improved the mechanical strength. Peng et al. managed to improve the response rate and mechanical property of the electro-responsive hydrogels by forming a hydrogel fiber and adding graphene oxide (GO).⁹² They used microfluidic spinning and free radical polymerization to obtain graphene oxide/polyacrylamide/sodium alginate hydrogel fibers. The hydrogel fibers bent toward the cathode when an electric field was applied. When the content of GO increased from 2% to 6%, the bending angle increased from 25° to 85°; this is due to the high content of polyions from the carboxylate groups in GO. These electricity-triggered biomimetic actuators should focus on interfacing with nervous systems and improving biocompatibility. With the more drastic improvement on electro-response rate as well as mechanical properties, biomimetic muscles that resemble actual muscle tissues are one step closer to our life. Hopefully,

people suffering from muscle malfunction or amputees using artificial limbs can benefit from the advancement of this research area soon.

1.3.3.3 Pneumatic & Hydraulic

Pneumatic and hydraulic biomimetic actuators have similar mechanisms, using fluids that are hard to compress to power the actuation movement. The general design idea is to create channels that can allow the fluids to occupy, which changes the volume that can result in conformation change or shape morphing locally. Through a careful design of the channels, different moving modes can be achieved. As mentioned briefly previously, the Whitesides group exploited a lot of pneumatic biomimetic actuators capable of more complex tasks that also are cheaper and simpler than conventional hard robots (Figure 1.10(a)).^{50, 93-95} They used networks of channels in elastomers for actuation that can inflate like balloons, which they called “PneuNets” (pneumatic networks). They were able to control the actuator by modifying the geometry of the embedded chambers and the material properties. When a PneuNets actuator is pressurized by air, expansion occurs locally in the most compliant regions (e.g., thinner walls). They could tune carefully the distribution, configuration, and size of the embedded pneumatic network to realize different movements according to specific task requirements. For example, they fabricated this starfish-like actuator gripper that can pick up a chicken egg. Moreover, they realized a crawling movement of an actuator by cycles of pressurization and depressurization of individual channels. They fabricated these artificial “fingers” that can play a tune on a digital keyboard as well as an array of expandable chambers that can manipulate a ball. Marchese et al. developed an autonomous soft robot fish capable of rapid, continuum-body motion.⁹⁶ The core of the fish's soft body was an array of fluidic elastomer actuators and a second inextensible but flexible layer that constrained the axial tension. When pressurized gas was pumped into the channels, the channels expanded and bent towards the other side. In this work, they used an 8 g CO₂ gas cylinder housing fluid at high pressure and low volume as the fluidic power supply, realizing a rapid body motion, such as escaping. However, the limitation of a pneumatic actuator is the gas supply. For example, approximately 30 tail beats were available from the 8 g CO₂ cylinder, which might be challenging for long term swimming robots.

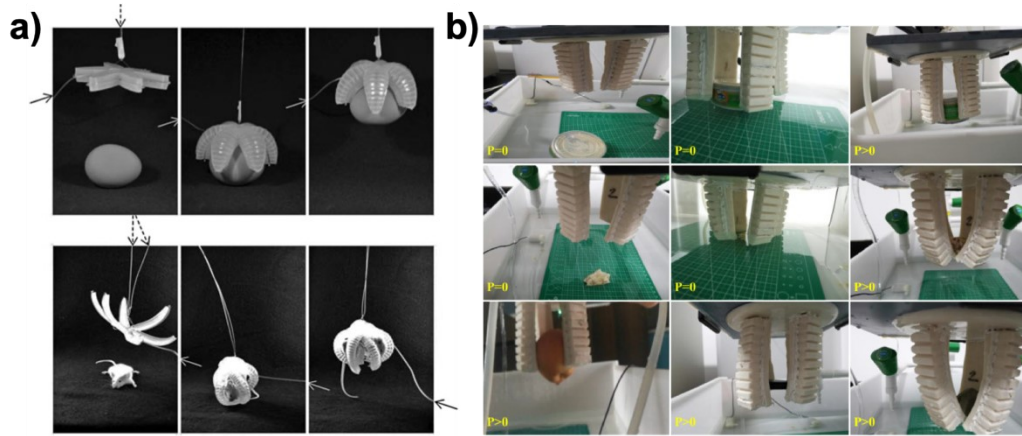


Figure 1.10. a) The top row shows a 9 cm tip-to-tip PneuNet gripping an uncooked chicken egg. On the bottom, a modified version of the starfish-based gripper with 14 cm tip-to-tip distance; thinner and longer fingers can pick up a live anesthetized mouse. Adapted with permission from Ref.⁵⁰ Copyright 2011, John Wiley & Sons, Inc. b) Experiments to grasp different items in water by the soft robotic gripper. (P represents the liquid pressure inside the chamber of the soft actuators. Reprinted from Ref,⁹⁷ with permission from Elsevier.

Hydraulic actuators use similar mechanisms. Due to the demand of air supply and air compressors in pneumatic actuators, it can be quite challenging to use them for long-term underwater applications. Chen et al. addressed this problem by developing these biomimetic actuators that were powered by water hydraulic energy and controlled by the supplied voltage of the pump instead of the pressure measured by a pressure sensor (Figure 1.10(b)).⁹⁷ Using a mold casting and bonding method, they fabricated three types of actuators for different purposes. The strong water hydraulic soft bending actuators (SWBA) consisted of extensible and inextensible layers with small gaps between the chambers in the extensible layer; they were used for requiring a certain deformation and a large force output, such as grippers. The flexible water hydraulic soft bending actuators (FWBA) were similar but with larger gaps; they were suitable for systems with large deformation, such as a robot fish. The flexible water hydraulic extending soft actuator (FWEA) contained two extensible layers only; they were used for actuators that use elongation as a movement mode, for example, a biomimetic sea cucumber. They demonstrated the three biomimetic actuators and are exploring new materials, new designs, and new applications.

Interestingly, in 2018, Acome et al. used a liquid dielectric (commercially available Envirotemp FR3 that was formulated from vegetable oils and made for use in

high-voltage transformers) and developed self-healing actuators with muscle-like performance, using electrohydraulic mechanisms.⁹⁸ The so-called hydraulically amplified self-healing electrostatic actuators (HASEL) could generate a hydraulic pressure locally via electrostatic forces acting on liquid dielectrics distributed throughout a soft structure. The actuation resulted from an electrostatic Maxwell stress that pressurized and displaced the liquid dielectric in between the electrodes. When the voltage surpassed a threshold that a mechanical restoring force was not able to hold the structure shape, the liquid dielectric pulled together abruptly, causing a large deformation. The authors utilized this property and modified two stacks of donut HASEL actuators to operate as a soft gripper. The highlight of using a liquid dielectric is that self-healing can be achieved thanks to its liquid nature.

1.3.3.4 Light

As mentioned briefly before, light received a lot of interest for usage as a stimulus due to remote operation possibilities without the introduction of wires, electrodes, or solutions. Moreover, light is a versatile energy source that is inexhaustible and tailorable in terms of wavelength and intensity. The most common light-triggered actuation mechanism is using photoisomerization of chromophores. Azobenzene, a typical photochromic molecule, can undergo a reversible cis–trans photoisomerization with the irradiation light of a certain wavelength.⁹⁹ The rate of isomerization is proportional to the product of the incident light intensity and the concentration of cis- or trans-azobenzene. Azobenzene often is used in a liquid crystalline network (LCN). Yamada and coworkers fabricated a motor device using laminated films composed of an LCE layer and an unstretched low-density PE film (Figure 1.11(a)).¹⁰⁰ By irradiating the belt with UV light from the top right, a local contraction force was generated to act on the right pulley, driving it counterclockwise. Meanwhile, a visible light from the top left generated a local expansion force. As a result, both actions induced a rotation of the belt continuously. Lu et al. from Yue Zhao group also fabricated large-size polymer photo-actuators in the form of wheels and spring-like “motors”, using dynamic covalent bonds for chain crosslinking (Figure 1.11(b)).¹⁰¹ However, they pre-stretched the ALCE film (LCE film with an azobenzene mesogens incorporated) and laminated

it with a flexible transparent polypropylene film. They speculated that for the pre-stretched ALCEs network, upon UV irradiation, both the mechanical energy conversion upon the trans–cis photoisomerization of azobenzene mesogens and the prestored strain energy release can be used to generate mechanical forces. For demonstration purposes, the film was cut and rolled into a tube shape. Upon UV light irradiation, the right side receiving illumination had a tendency to flatten, which caused a shift of the center of mass to the left side. As a result, the wheel-shaped tube rolled away from the light. Due to the elasticity of the polypropylene film, the bilayer could recover the initial curvature when it “escaped” the UV light source. Moreover, the rolling direction could be altered by swapping the layer position, and the speed could be adjusted by adjusting the prestored strain energy. They also demonstrated a spring-like structure for forward and backward rolling. Ma et al. demonstrated photodriven swimmers, based on a bilayer structure of an azobenzene-containing liquid-crystalline polymer network (LCN) and Kapton. Upon UV irradiation, the LCN layer underwent trans-to-cis and cis-to-trans isomerization that induced changes in the molecular voids during the dynamic process.¹⁰² As a result, the bilayer structure exhibited deformation upon irradiation/removal of UV light. Just like a “dolphin kick”, the swimmer sheet could propel itself forward due to the deformation of the structure. However, most of the reported light triggered LCN systems were actuated by ultraviolet (UV) or visible light of short wavelength, which is not practical for safe applications. Jiang et al. addressed the problem by a red-light-controlled soft actuator that was driven by low-power excited triplet–triplet annihilation-based upconversion luminescence (TTA-UCL).¹⁰³ They used platinum(II) tetraphenyltetrabenzoporphyrin (PtTPBP) as the sensitizer and 9,10-bis(diphenylphosphoryl)anthracene (BDPPA) as the annihilator to prepare the red-to-blue TTA-based upconversion system. They incorporated the system into a rubbery polyurethane film and fabricated a bilayer structure using an azotolane-containing LCN film. When irradiated with a 635 nm laser at a low power density, the soft actuator was able to bend towards the light source. It is noted that the red light showed a negligible thermal effect and an excellent tissue penetration ability; this work opened the gate for light-responsive actuators to be implemented in biological systems.

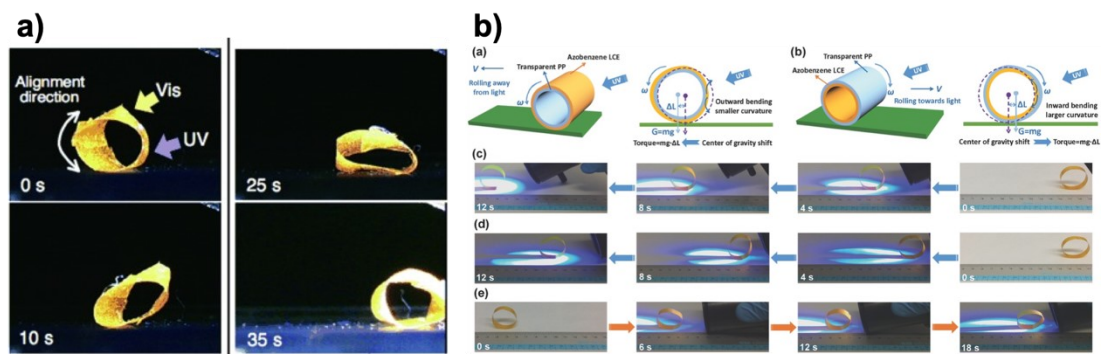


Figure 1.11. a) Photoinduced rolling motion of a continuous ring of LCE film. Reprinted with permission from Ref.¹⁰⁰ Copyright 2008, John Wiley & Sons, Inc. b) Schematic showing leftward and rightward shift of the center of gravity in the wheel due to the UV-light-induced asymmetric deformation. Adapted with permission from Ref.¹⁰¹ Copyright 2017, John Wiley & Sons, Inc.

Spiropyran is another photochromic molecule that undergoes C(spiro)–O bond cleavage upon UV light irradiation or at a low pH ($\text{pH} < 4$).^{104, 105} During isomerization, the molecule changes from a colorless, nonplanar, closed, and neutral form to the colored, planar, open, and charged form. Dunne et al. generated photo-actuator hydrogels using an N-isopropylacrylamide-co-acrylated spiropyran-co-acrylic acid (p(NIPAm-co-SP-co-AAc)) copolymer.¹⁰⁶ The pore size and density of the hydrogels, which had an impact on the response kinetics, were altered by changing the solvent. When the hydrogel was immersed in DI water and placed in the dark, protons from the AA comonomer protonated the SP unit to afford the hydrophilic MC-H⁺ form that induced expansion in the hydrogel. When the hydrogel was irradiated by a white light, deprotonation of MC-H⁺ happened, causing the gel to shrink due to hydrophobicity nature of the SP form. Based on the mechanism, the authors fabricated a bipedal hydrogel walker and actuated it with a white light on a ratcheted surface. Due to the expansion and contraction of the hydrogel, the walker was able to walk in a given direction.

Photothermal conversion is one way of using light as a trigger mechanism. However, the ultimate effect of this is increasing the temperature. For clarity purposes, all discussion on photothermal conversion used for biomimetic actuators were discussed in Section 1.3.3.1.

Despite many innovations and advancements in this research area, many challenges are to be addressed. For example, photothermal conversion efficiency

should be improved for better efficiency. Biocompatibility, maneuverability, feedback systems, as well as novel structure and programmable shape deformation designs should be developed for these actuators to expand their applications, such as in biological systems and smart robotics.

1.3.3.5 Magnetic Field

Magnetic materials are another class of materials that received great attention due to their fast response, remote actuation, and large penetration range. Due to the programmability of magnetic fields, actuators with multiple complex shape deformations could be achieved. A magnetorheological (MR) fluid consists of ferromagnetic microparticles suspended in nonmagnetic liquids.^{107, 108} Without a magnetic field, it behaves like a liquid but can form spiky and blade-like structures when actuated by magnetic fields. They can change viscosity quickly in response to an applied magnetic field. Jackson et al. demonstrated tunable field responsive mechanical metamaterials (FRMMs) that have a large dynamic range as well as a rapid and reversible mechanical response to magnetic fields.¹⁰⁹ They found an enhancement of effective stiffness when the MR fluid was infilled into 3D printed cuboctahedron unit cells with magnetic fields applied from the same direction as the compressive load. Song et al. developed a new soft magnetic composite material by incorporating magnetic microspheres (neodymium–iron–boron (NdFeB)) that were encapsulated in oligomeric polyethylene glycol (PEG) into an elastomeric matrix (Ecoflex 00-30).¹¹⁰ Due to the solid-to-liquid phase transition of this encapsulating oligomer, rearrangement of the magnetic particles in the microspheres was possible. As a result, the magnetization patterns could be rewritten into other forms by heating the structure to induce the phase transition. The authors demonstrated various interesting and complex transformations for a linear magnetic bar, a magnetic membrane, and a reconfigurable soft magnetic origami sheet under the applied magnetic fields. An in-situ reprogramming magnetization profile and various shape transformations also were realized by embedding a conductive heating layer. The reprogrammable soft magnetic actuator could copy even the surface curvature of an arbitrary object. Xie et al. used programmable alternating magnetic fields to manipulate magnetic microrobots.¹¹¹

They demonstrated that these magnetic microrobots could be reconfigured into multiple formations that also were reversible, for example, liquid, chain, vortex, and ribbon. Microrobotic swarms passing through narrow walls or handling large loads were demonstrated. Hopefully, these microrobots that are small enough to navigate blood streams can provide potential solutions for various biomedical applications, such as imaging and targeted drug delivery.

An interesting property of magnetic particles is the magneto-thermo effect. When placed in an alternating magnetic field, the magnetic particles can produce heat to the surrounding environment. This effect has found its application in various fields, such as drug release and hyperthermia cancer treatment.¹¹² It also provides insights that magnetic particles can be incorporated as a heat source for actuator applications, using the temperature change as an actuation mechanism. The benefit of utilizing this effect is eliminating the requirement for a water bath or heating elements that hinder the free floating of the actuators. Just like using light as a trigger mechanism, the afforded actuators can be manipulated remotely, and the actuation can be programmable thanks to the tailorability of alternating magnetic fields. Tang et al. synthesized a magnetic pNIPAm hydrogel, using hectorite nanoclay as crosslinkers and Fe_3O_4 magnetic particles as dopants (Figure 1.12).¹¹³ The magnetic hydrogels were shown to evolve from 2D-structured sheets into 3D shapes like lotus flowers.

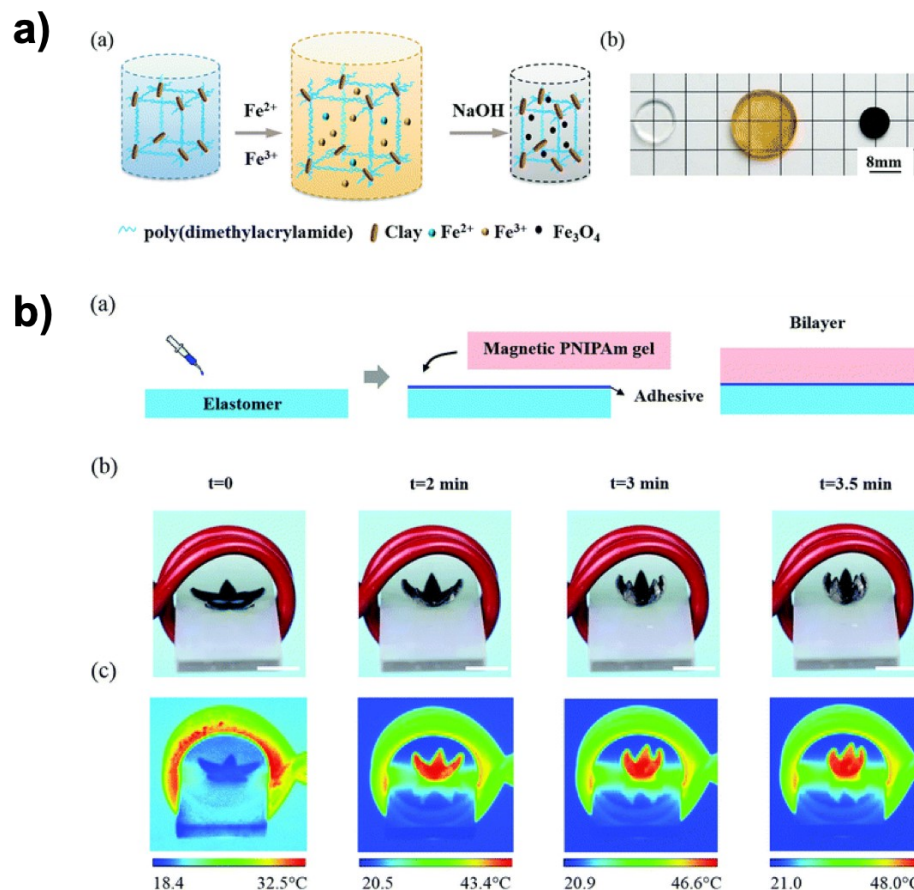


Figure 1.12. a) Highly stretchable PDMA/Fe₃O₄ magnetic NC hydrogel. Schematic of the preparation of magnetic hydrogels and Images showing three types of hydrogels. b) Remotely triggered shape morphing of magnetic hydrogels. Adapted with permission from Ref.¹¹³ Copyright 2018, Royal Society of Chemistry.

1.3.3.6 PH

Apart from the aforementioned spiropyran, polymers bear ionizable groups, such as pAAc, poly(methacrylic acid) and poly(dimethylaminoethyl methacrylate) (pDMAEMA), also are pH-responsive. Islam et al. synthesized pNIPAm-co-AAc microgels on a gold-coated substrate. After depositing poly(diallyldimethylammonium chloride) (pDADMAC) solution, a polycationic solution with a pH of 6.55, which is higher than the pK_a of AAc (~4.25).¹¹⁴ As a result, AAc groups in the microgels are deprotonated and establish a strong electrostatic interaction with pDADMAC. This offers a long-range interaction across the whole microgel-coated surface. When the microgels dry, the enhanced hydrophobic interaction due to the larger screening effect on the pDADMAC polymer chain, along with the long-range electrostatic interaction

pull the whole microgel surface together, which results in shattering the glass substrate or curling the plastic elastomer substrate. They later used this mechanism on a bilayer gripper actuation. As mentioned before in the temperature responsive actuator section, a temperature responsive gripper was fabricated. Using a similar design, they copolymerized AAc into the pNIPAm hydrogel. The protonation and deprotonation endowed the actuator with pH responsivity. When the pH is higher than the pK_a of AAc, the AAc groups are deprotonated and form strong electrostatic interaction with pDADMAC, causing the hydrogel to shrink and the gripper to bend toward the hydrogel side. When the pH is lowered, the AAc groups are protonated and pDADMAC groups are released and regain the free state to absorb a large amount of water, leading to the gripper bending towards PDMS side.

Lee et al. fabricated a pH-responsive actuator by combining an ionoprinting method and catechol-metal coordination chemistry (Figure 1.13(a)).¹¹⁵ Using electrochemistry with the presence of borate, Fe^{3+} ions were imprinted into a poly(N-hydroxyethyl acrylamide) hydrogel with catechol and dopamine methacrylamide copolymerized. When submerged in a basic solution, the crosslinking density increases and results in bending of the material. After soaking in acidic solution, phenol groups are protonated, releasing the captured Fe^{3+} , thus decreasing the crosslinking density. The bending shape can be recovered.

Dynamic phenylboronic acid (PBA)-diol ester bonds can provide pH-responsive crosslinks in the hydrogel network. Meng et al. utilized this mechanism and synthesized a pH-induced actuator (Figure 1.13(b)).¹¹⁶ At a basic pH, esterification happens between the PBA groups grafted on the alginate network and the hydroxyl groups in polyvinyl alcohol, which can lock the temporary shape. When the pH is lowered, the ester bonds are dissociated, resulting in the softening and shape recovery of the actuator. Zhang et al. reported a similar example that involved hydrogen bonding between PAAm and PAAc (Figure 1.13(c)).¹¹⁷ The authors could realize a hydrogel volume change, resulting from a hydrogen bonding disruption, by changing the pH.

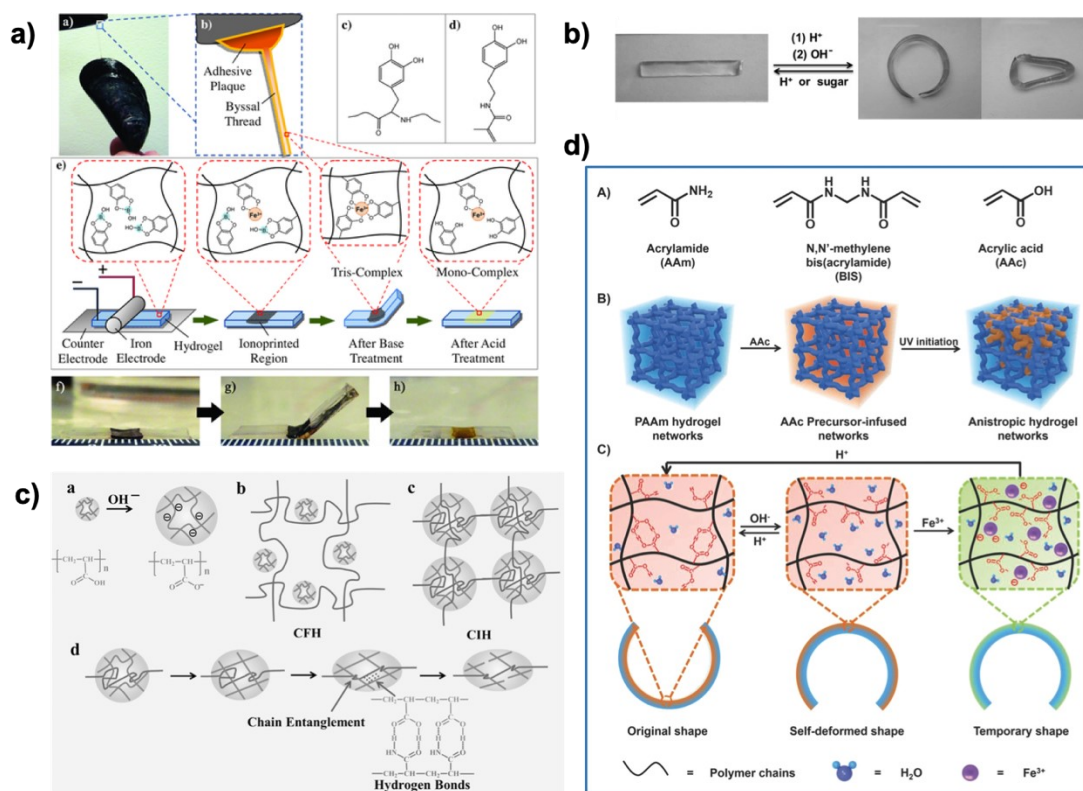


Figure 1.13. a) A photograph of a mussel attached to the shell of another mussel, Schematic representation of the adhesive plaque and byssal thread, and Schematic representation of the ionoprinting process. Adapted with permission from Ref.¹¹⁵ Copyright 2014, John Wiley & Sons, Inc. b) Shape memory effect of the Alg-PBA/PVA hydrogel. Reprinted with permission from Ref.¹¹⁶ Copyright 2015, John Wiley & Sons, Inc. c) Schematic illustrations of the structure of different hydrogels. Reprinted with permission from Ref.¹¹⁷ Copyright 2016, John Wiley & Sons, Inc. d) Schematic illustration of controllable self-driven hydrogel with shape memory effect. Reprinted with permission from Ref.¹¹⁸ Copyright 2018, John Wiley & Sons, Inc.

For the previous pH-responsive actuator examples, the actuation resulted from a crosslinking density change. Another type of pH responsiveness of the material is endowed by the ionizable groups in the polymer network. There are two main kinds of pH-responsive actuators, anionic and cationic type actuators. For the anionic type, there are ionizable groups that can undergo significant deprotonation when the pH is lower than the pK_a of the groups to form anions. Due to the electrostatic repulsion between the anions, the material can exhibit a volume expansion in aqueous media. Similarly, cationic type actuators can get mostly protonated and carry a positive charge, thus expand when the pH is lower than the pK_a of the pendant groups. Le et al. fabricated an anisotropic actuator by soaking a PAAm hydrogel in an AAc monomer solution, followed by photopolymerization with inhomogeneity across the depth (Figure

1.13(d)).¹¹⁸ The AAc groups can deprotonate after NaOH is added and can cause the hydrogel to expand. Adding HCl to protonate the AAc groups can shrink the hydrogel. They demonstrated this reversible actuation by fabricating a flower that can bloom and close upon pH changes.

1.3.3.7 Ions

Many ion-responsive polymer-based actuators are responsive to ionic strength change in the environment. Ionic strength has a great impact on the swelling and deswelling properties of an ionic hydrogel network. When the ionic strength is high, the electrostatic interaction will be shielded largely, thus changing the swelling properties of ionic hydrogels. Liu et al. fabricated a bilayer actuator by simply attaching two pre-made hydrogel sheets together.¹¹⁹ By incorporating dimethylaminoethyl methacrylate methylchloride (DMC) and 2-acrylamido-2methyl-propanesulfonic acid (AMPS) as comonomers into the AAm network, cationic and anionic hydrogels were made. The bilayer was assembled simply by putting two opposite charged hydrogel sheets together, utilizing electrostatic interactions between them. Due to the different response to ionic strength, the two layers can exhibit different swelling and deswelling properties. By changing the ionic strength with time, the bilayer actuator showed bending and unbending reversibly.

Huang et al. developed a 4D-shape changing material by using ionic strength as the fourth-dimension change.¹²⁰ Using a digital projector, a monomer mixture, including potassium 3-sulfopropylmethacrylate (PSPMA), was polymerized into a 2D hydrogel with a different crosslinking density pattern. PSPMA endowed the hydrogel with the responsivity to ionic strength change.

Because ionic polymer networks are involved, which is similar to pH responsive polymer-based actuators, ionic strength and pH always are used together to realize actuations. As discussed in the pH-responsive section, the pH-responsive actuator developed by Le et al. also had ion responsivity. Due to the coordination between carboxylate groups and Fe^{3+} ions, additional crosslinking can be formed to lock the temporary deformation. This crosslinking can be destroyed under acidic conditions due to the protonation of the carboxylate groups. Similarly, Ma et al. from

the Ximin He group designed an elastic-driven strong contractile hydrogel, using the coordination interactions between carboxylate groups and Fe^{3+} ions (Figure 1.14(a)).¹²¹ They pre-stretched the hydrogel and soaked it in FeCl_3 solution to afford a temporarily locked hydrogel. The hydrogel could be actuated by an HCl solution that destroyed the crosslinking points by protonating the carboxylate groups. As a result, the elastic energy was released and harnessed to power movements, such as lifting a heavy mass, bringing sheets with weights together, and withstanding heavy loads in a bridge form. Ma et al. fabricated a bilayer structured actuator assembled by a host–guest interaction (Figure 1.14(b)).¹²² A responsive hydrogel can undergo a volume change, thus causing the bilayer actuator to bend towards different directions under different pH and ionic strength.

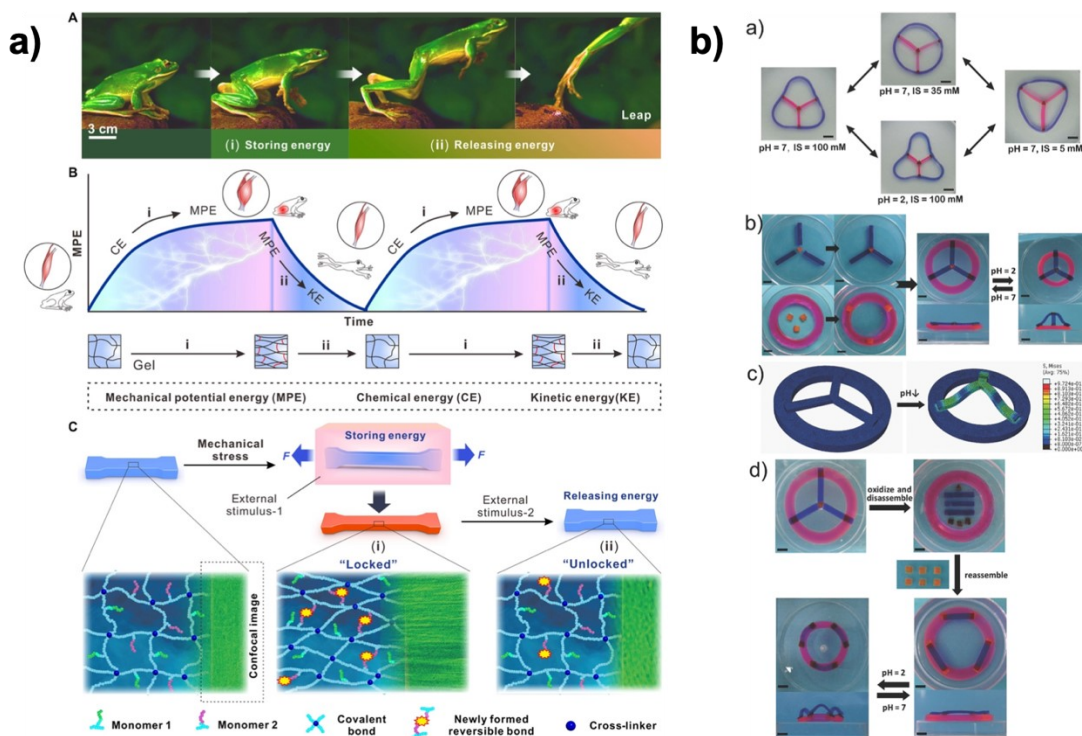


Figure 1.14. a) Conceptual scheme of the strong contractive materials based on mechanical energy storing method. Reprinted from Ref.¹²¹ Copyright 2020, Yanfei Ma et al. b) Complex shape transformations of the Lego hydrogels. Reprinted with permission from Ref.¹²² Copyright 2014, John Wiley & Sons, Inc.

1.4 Challenges and Outlooks

In this chapter, we gave an introduction on biomimicry and some of the history of its development. Billions of years' evolving has bestowed living creatures with the most efficient functions, which are hard for human beings to emulate in a short period of time. Scientists and researchers had been observing these creatures, trying to find out their secrets. However, it was way too difficult to understand the mechanism, let alone using them to fabricate products. They circumvented this problem by sorting approaches to mimic the functions, using different mechanisms since realizing the functions were the ultimate goal. Due to the enormous amount of living organisms and their various distinct traits and functions, biomimicry always will be fueled to continue developing, as long as we keep exploring. With the advancement of different technologies, such as electron/fluorescence microscopes that made smaller features visible to mimic, 3D printing technology for easier fabrication, and soft materials for more versatile and compliant applications, more novel inventions and technique breakthroughs were possible. Secondly, we provided a lot of examples of how biomimicry realized enormous applications that improved people's lives. Biomimicry could give people more information to better understand their situation. Also, scientists and researchers encompassed a lot of bio-inspired properties to afford products with exciting new features. Finally, we focused our discussion on biomimetic actuators since motion is essential for human beings. A lot of simple or complex tasks could be accomplished by the biomimetic actuators that ultimately could free our hands and help improve our life quality. Different mechanisms of the biomimetic actuators were discussed, and some insights were provided to inspire the readers to think about the future possibilities for each individual mechanism.

However, there are a lot of challenges to be addressed. How to make the biomimetic actuators more intelligent will always be the focus for generations to come. For the biomimetic actuators that can provide information, researchers should dedicate in combining artificial intelligence with these physical actuators, enabling more complete feedback loops for these actuators to work more independently with the ability to learn and make decisions. Research should also eliminate the barrier between the actuators and real biological systems by improving the biocompatibility of the

materials and realizing integration with the nervous systems. The vision for those accessibility actuators is that they can help amputees regain their senses, limb functions, and ultimately their normal life.

Biomimetic actuators need the cooperation among researchers from all different backgrounds. Chemists, biologists, engineers, computer scientists, and even designers and governors should come together to advance this area to benefit human beings and the society. There is a long way to go, and we are optimistic.

In this thesis, we will show three main projects, all of which are inspired by nature. The first one is a wireless swimming actuator inspired by an octopus. The device can swim both fast and slow, resembling an octopus swim slow when care-free and snap away when encountering danger. The second is a touch-responsive actuator mimicking the shy plant closing its leaves when touched. The last one is a cargo transporting actuator showing the ability of capturing, transporting, and releasing cargos. We hope that we can provide some insights and inspiration by showcasing some of the new designs and new actuation mechanisms using some well-studied materials.

Chapter 2

Octopus-Like Shape-Memory-Alloy-Based Bistable Metal Actuators^a

2.1 Introduction

For centuries, humans have been fascinated with studying nature and natural processes; this most certainly began out of curiosity, although in many cases it led to a desire for mimicry.^{65, 123, 124} For example, primitive, early humans would move, dress, and act like animals to improve their hunting successes, while modern day mimicry is focused on the development of new synthetic materials for improving human health and quality of life.^{125, 126} Of course, nature has the ability to adapt to changes in environmental conditions and added pressures via many years and generations of evolution, while humans are left primarily using rational thought, science, and engineering for adaptation. A great example of nature adapting to their environment for self-gain is the octopus. The octopus is an intelligent marine creature that has evolved the ability to change color and eject ink when in danger in order to escape and preserve its well-being. Octopus also exhibit high dexterity, capable of reaching,¹²⁷ grabbing,¹²⁸ swimming,¹²⁹ and walking.¹³⁰ Interestingly, they have the ability to swim slowly to disguise themselves as floating algae in ocean currents, while maintaining the ability to swim quickly away in a moment by contracting their bodies and whipping their tentacles. Here, we introduce a device composed of Nitinol wire (a shape memory material) and bistable metal strips to generate a device that is capable of mimicking the swimming behavior of an octopus by exhibiting the ability to swim slowly and “instantaneously” fast by simply changing how the device’s components are stimulated electrically.

^a The contents of this chapter have been copied and/or adapted from the following publication: “Y. Wan, K. Cuff, M. Serpe, *Adv. Intel. Syst.* **2022**, 210025.”

Nitinol, generated by alloying nickel and titanium, has many interesting uses and properties, e.g., shape memory, superelasticity, anticorrosion, and biocompatibility.⁶⁰ As a result of these interesting properties and attributes, it has been used for applications in aeronautical and space technologies, automobile industries, medical devices, and civilian products.⁵⁹ Of importance to this investigation is Nitinol's shape memory properties, which we propose harnessing for this new approach to actuation. Nitinol can be "trained" to adopt a desired permanent shape when it is fixed into that shape and heated above the austenite finish temperature (A_f), causing it to adopt a cubic and hard austenite (B2) state. Then, upon rapid cooling of the Nitinol to below the martensite finish temperature (M_f), it adopts a hexagonal, ductile, and twinned martensite (B19') state.⁶³ When the temperature is below M_f , the Nitinol can be reshaped by an external force into any temporary shape by conversion into detwinned martensite. Phase transformation does not occur at a particular temperature but within a range of temperatures. Thus, upon heating to above the austenite start temperature (A_s), a phase transition from martensite to austenite is initiated, and the Nitinol starts to recover its permanent shape slowly; the shape recovery completes at A_f . Importantly, when the temperature is lowered to the martensite start temperature (M_s), the phase starts to transform from austenite to twinned martensite, and the transition completes at M_f . At this point the Nitinol can be reshaped again. This shape memory behavior is the key to our actuation device. Heating of Nitinol can be achieved by direct heating or via resistive/Joule heating by applying a voltage to the wire that generates a subsequent current. For this study, we were interested in using Joule heating to trigger the shape memory behavior from the Nitinol.

Bistable materials are known to exist in two stable states that could differ in conformation dramatically. Very common examples of bistable materials are slap bracelets (a child's toy) and metal measuring tapes. In these examples, an external stimulus (force) can be used to trigger the metal strip to morph quickly from one stable state (e.g., extended state) to the other (e.g., coiled state) in what often is called "snap-through" behavior.¹³¹ This sudden and powerful actuation is intriguing if it can be harnessed and utilized, in our case, for shape changing devices^{95, 132} that can be used for swimming.

In this work, we propose harnessing the power of shape memory materials for actuation (and ultimately swimming) by coupling Nitinol wire to bistable materials in a device. By combining these two classes of materials in a device and utilizing the actuation afforded by Nitinol and the snapping power of bistable metal strips, we developed a novel actuator that mimics the slow and fast swimming behavior of an octopus. Furthermore, by controlling and moving the arms independently (via electrical stimulation), the device can navigate through space in any direction. Additionally, a wireless control system, equipped with a rechargeable battery, was designed to make the device totally autonomous and untethered from external wires that otherwise would be needed for control. Finally, we demonstrate that we can integrate etalon-based sensing devices¹³³ into the construct to monitor water pH and ionic strength. In this case, the etalons tethered to the swimming device change color (that can be captured with an on-board camera) as the water properties change. Successful integration of these sensing devices into the construct demonstrates the potential utility of these devices for environmental monitoring applications, as well as others.

2.2 Experimental Section

Bistable Metal Strip Characterization: Bistable metal strips were purchased from Amazon (Seattle, Washington, USA), originally sold as slap/snap bracelets. We removed the plastic covers to obtain the metal strips with 21 cm in length, 2.5 cm in width, and 0.15 mm in thickness. The metal strip has curvature on both the long and short directions; the curvature is 1.5 cm for the long side and 2.4 cm for the short side. A pair of tin snips was used to cut the metal strips into different shapes with different taper ratios. A small hole was punctured on the tip of the metal strip to allow us to fix a piece of commercially available fishing thread (Beadalon Supplemax JNX0.25W-F, Coatesville, Pennsylvania, USA) with 0.01 inch diameter. We then screwed a nail in the middle of the metal strip, which acts as a pivot and allows its fixture on the clamp. The other end of the thread was fixed onto a force sensor (Vernier Dual-Range Force Sensor, Beaverton, Oregon, USA). A pulley was used to adjust and fix the force angles. The thread is pulled until the metal strip snaps or resets, and the forces are recorded in the Logger Pro software for later analysis.

Nitinol Wire Permanent Shape Setting: Nitinol wire with 0.02 inch diameter was purchased from McMaster-Carr (Elmhurst, Illinois, USA). The Nitinol wire was coiled onto a 5 mm metal hex wrench with a pitch of 5 mm. The two ends were fixed using copper wire. Then, it was kept inside a furnace (Thermolyne FB1315M, Thermo Scientific, Waltham, Massachusetts, USA) preheated to 510 °C for 30 min. It was chilled quickly in room temperature (~24 °C) tap water until it cooled.

Nitinol Wire Characterization: The Nitinol phase transition temperature was tested both by DSC and water bath test with a 22.86 mg Nitinol sample that was cut from the pre-set Nitinol coil. Mettler Polymer DSC (Mettler Toledo, Columbus, Ohio, USA) using STARe software (version 16.10) was used to perform a DSC test by sweeping the temperature between 0 °C and 150 °C at a heating rate of 20 °C per min. For the water bath test, a beaker of water was heated while monitoring the temperature. The coiled Nitinol wire was stretched, immersed into a water bath at different temperatures, and the length change recorded.

Nitinol actuation voltage and durability tests were done with the same setup. Pre-stretched Nitinol wire was fixed one end to a monkey bar, the other to a force sensor. Powerstat (Staco Energy Products Co. Type 3PN1010, Miamisburg, Ohio, USA) was used to deliver power. The on/off operations were performed by hand, which can be inconsistent between repeats. The actual on/off can be interpreted from the force/time graph.

Fabrication of PAAm Hydrogel-Coated Nitinol Wire Coil: All the chemicals were purchased from Sigma-Aldrich (St. Louis, Missouri, USA) and used as received. Milli-Q water was used, unless otherwise stated. The PAAm hydrogel-coated Nitinol wire coil was fabricated by wrapping the hydrogel with a thin long channel in the middle onto the coiled-shaped Nitinol wire. First, a pre-solution for hydrogel was prepared; it contained 0.5331 g of acrylamide (AAm) as monomer, 1.156 mg (0.1 mol% of AAm) of N,N'-Methylenebis(acrylamide) (BIS) as crosslinker, and 13.5 mg of potassium persulfate (KPS) as initiator. Deionized (DI) water is added to afford a 2.5 mL solution mixture for later use. To prepare the long hydrogel with a thin channel inside, we used a commercially available fishing thread (Beadalon Supplemax JNX0.25W-F, Coatesville, Pennsylvania, USA) with 0.01 inch diameter as a template.

A plastic tube with a 3.20 mm inner diameter was used. We horizontally clamped the plastic tube, put the fishing thread inside, and fixed the two ends onto monkey bars. Then, we pulled the thread to give it a bit of tension to make sure it is straight inside the tube. The position of the tube and the thread were adjusted carefully so that the thread is going through the centre of the tube (Figure 2.1). A 20 μ L aliquot of N,N,N',N'-tetramethyl ethylenediamine (TEMED) as an accelerator was mixed with the prepared pre-solution. Some solution was taken using a syringe and slowly injected into the tube. After polymerization is completed and the hydrogel formed, we pulled the thread slowly to remove the hydrogel out of the tube, then gently removed the thread inside; this should leave a vacant channel inside. Lastly, the Nitinol wire is slid into the hydrogel through the channel.

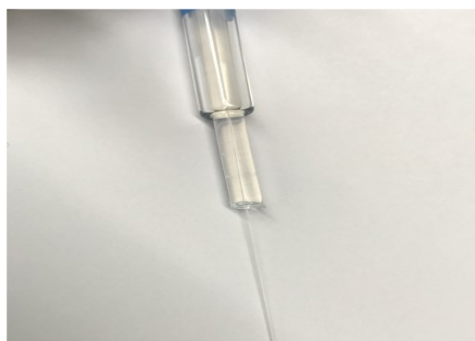
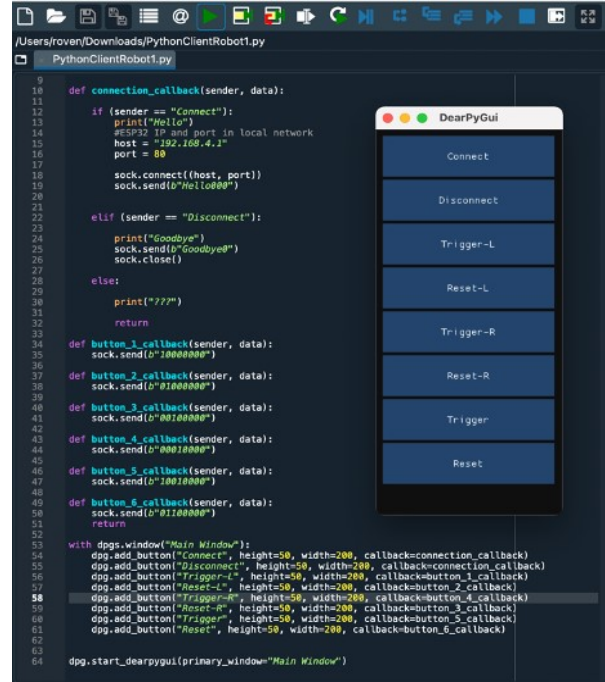


Figure 2.15. Hollow channel introduction. The outer layer is a straight glass tube, a plastic tube is inserted in the glass tube to get supported and avoid being bent, and a long fishing thread is placed in the middle of the plastic tube.

Fabrication of PDMS Fish Fins: SYLGARD™ 184 Silicone Elastomer Kit from Dow Inc. (Midland, Michigan, USA) was purchased from Sigma-Aldrich. A polymeric base and curing agent were mixed in a 10:1 ratio. Some glitter powder (purchased from Dollarama, Montreal, Québec, Canada) was added, together with some crystal violet (Sigma Aldrich) for easy visualization under water. It was mixed well, and the mixture poured into a large Petri dish. The Petri dish was placed on a heating plate overnight at 65 °C. A few 3 mm wide plastic strips were cut from a piece of transparency film (3M PP2950, Saint Paul, Minnesota, USA). The strips were placed onto the PDMS, and another layer of PDMS pre-solution was poured and cured overnight, similarly to the

previous steps. The cured PDMS sheet was cut into the fish fin shape, and the final fish fins were attached onto the two ends of the bistable metal strip using superglue.

Design and Assembly of the Wireless Swimming Device: A lithium ion polymer battery (FCONEGY 11.1 V 3S 7000 mAh 40 C Lipo RC Rechargeable Battery), a wireless Wi-Fi module with a camera (CANADUINO ESP32-CAM Wi-Fi Bluetooth Module with 2MP Camera), a voltage limiter (KeeYees MP1584EN Mini Step Down Buck Converter Adjustable DC to DC 4.5–28 V to 0.8–20 V Voltage Regulator Module), and four electronic switches (Mosfet Driver Module Dual High-Power 0–20 kHz FET PWM Trigger Switch Driver Module DC 5 V-36 V 15 A) were purchased from Amazon. One outlet from the battery was connected with the voltage limiter and then connected to the wireless Wi-Fi module. Then, the Wi-Fi module was connected to four electronic switches, which also are powered directly by the battery through the second outlet. The electronic switches had wires to connect with the four pieces of Nitinol wires. The Wi-Fi module was programmed using Spyder 4.2.5 on Anaconda Navigator (Figure 2.2).



```

PythonClientRobot1.py
PythonClientRobot1.py
9
10 def connection_callback(sender, data):
11
12     if (sender == "Connect"):
13         print("Hello")
14         #ESP32 IP and port in local network
15         host = "192.168.4.1"
16         port = 80
17         sock.connect((host, port))
18         sock.send(b"Hello000")
19
20
21
22     elif (sender == "Disconnect"):
23
24         print("Goodbye")
25         sock.send(b"Goodbye0")
26         sock.close()
27
28     else:
29         print("???")
30
31     return
32
33
34 def button_1_callback(sender, data):
35     sock.send(b"00000000")
36
37 def button_2_callback(sender, data):
38     sock.send(b"01000000")
39
40 def button_3_callback(sender, data):
41     sock.send(b"00100000")
42
43 def button_4_callback(sender, data):
44     sock.send(b"00010000")
45
46 def button_5_callback(sender, data):
47     sock.send(b"10010000")
48
49 def button_6_callback(sender, data):
50     sock.send(b"01100000")
51     return
52
53 with dpg.window("Main Window"):
54     dpg.add_button("Connect", height=50, width=200, callback=connection_callback)
55     dpg.add_button("Disconnect", height=50, width=200, callback=connection_callback)
56     dpg.add_button("Trigger-L", height=50, width=200, callback=button_1_callback)
57     dpg.add_button("Reset-L", height=50, width=200, callback=button_2_callback)
58     dpg.add_button("Trigger-R", height=50, width=200, callback=button_3_callback)
59     dpg.add_button("Reset-R", height=50, width=200, callback=button_4_callback)
60     dpg.add_button("Trigger", height=50, width=200, callback=button_5_callback)
61     dpg.add_button("Reset", height=50, width=200, callback=button_6_callback)
62
63
64 dpg.start_dearpygui(primary_window="Main Window")

```

Figure 2.16. Programming and coding. Arduino and Spyder is used to upload the code and program the Wi-Fi module. DearPyGui is used as a control panel to actuate the swimming device.

3D Printing of the Device Parts: The parts were designed using FreeCAD. A hollow design was adopted to hide the connecting wire in order to avoid cluster and keep the swimming device neat (Figure 2.3). A Prusa 3D printer (Prusa Research Company, Prague, Czech Republic) was used for printing using polylactic acid (PLA) as the printing material.

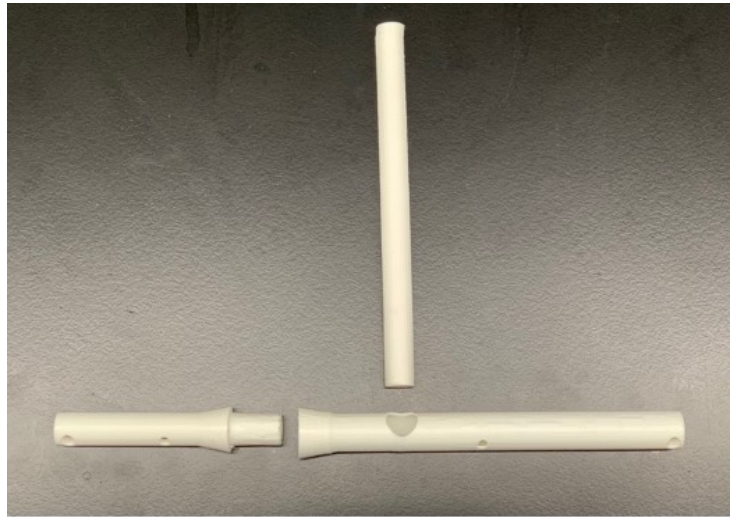


Figure 2.17. Layout for the 3D printed parts of the swimming device. All connecting wires can go inside the parts to avoid cluster and entanglement.

Design and Assembly of the Sensing Platform: The holder was designed using FreeCAD and 3D printed using a Prusa 3D printer. The holder was attached to the styrofoam boat and adjusted so that the etalon chips could be immersed fully in water. The camera and LED lighting system were included in the wireless Wi-Fi module and were integrated and programmed into the whole control system so that the picture taking and lighting can work together to get good quality pictures.

Salt and pH sensing: Etalons were fabricated based on a previous procedure (Figure 2.4). For the salt response investigation, the swimming device was put into DI water with the etalons fully immersed under water overnight. Pictures were taken to record the initial color. Then, the media was changed to a 0.5 M NaCl solution, and pictures taken every minute to record the color change. Similarly, for pH sensing, pH 6.02 was used to record the initial color. Then, the media was adjusted to pH 2.69, then 10.99, and color evolution was recorded by the camera system.

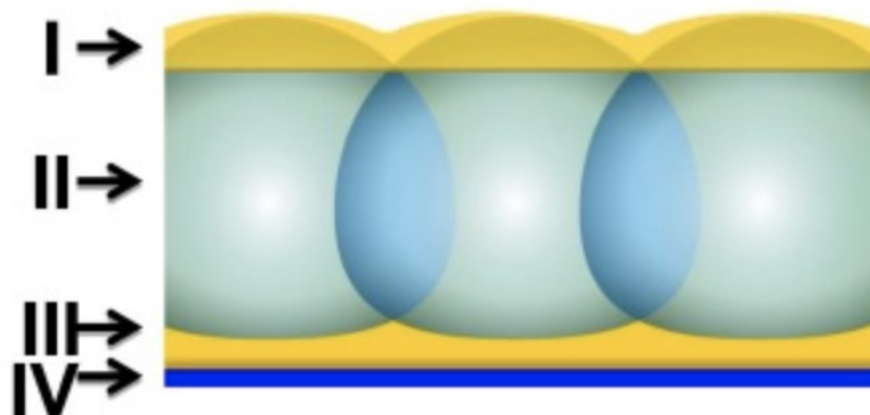


Figure 2.18. Picture shows the basic structure of pNIPAm microgel-based etalon composed of a monolith of microgel layer (II) sandwiched between two gold layers (I and III) on a support glass substrate (IV). To fabricate etalon chips, first, PNIPAm-based microgels containing 10% acrylic acid (AAc) (pNIPAm-co-10%AAc) were prepared by free radical precipitation polymerization of the monomer NIPAm with N,N' -methylenebis(acrylamide) (BIS) as the crosslinker and AAc as a comonomer. The resulting microgels have a size about 750 nm in diameter. For the etalon chip, 2 nm Cr and 15 nm Au were subsequently coated on to the glass slides using thermal evaporator. A layer of microgel was coated, and then another 15 nm Au layer was deposited.

2.3 Results and Discussion

For this study, in order to generate devices capable of exhibiting slow and fast swimming behavior upon electrical stimulation, the power of Nitinol and bistable strips needed to be harnessed using careful device design principles. The design we converged on after many iterations is shown schematically in Figure 2.5. As can be seen, four pieces of pre-set short helical Nitinol wires were stretched and attached to the tip of a bistable metal strip. When a voltage is applied to the Nitinol wires, e.g., the front left (FL) piece, the FL Nitinol wire heats up and will shorten, thus pulling the tip of the bistable metal strip, causing it to snap and coil (trigger process). This snapping process results in lengthening/straightening of the back left (BL) Nitinol wire. The shortening/contraction of the BL Nitinol wire can be triggered further by application of a voltage/heat pulling the tip of the bistable metal strip to uncoil and return it to a flat state (reset process). This reset process once again lengthens the FL Nitinol, which prepares the device for its next trigger process. Thus, by carefully (and independently) controlling the conformational state of the four pieces of Nitinol wires with voltage, the state of the bistable strip can be manipulated and controlled, allowing slow and fast

movement of the device's arms, much like the control an octopus has over its tentacles. To understand how all of the pieces of the device work together to achieve the desired behavior, a detailed examination of the device's components is required, as detailed below.

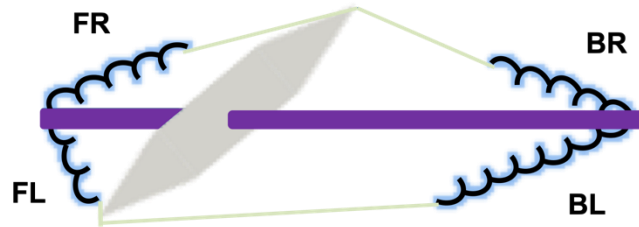


Figure 2.19. Conceptual design of the swimming device. The gray piece is a bistable metal strip; black coils are Nitinol wires (FL: front left; FR: front right; BL: back left; BR: back right); blue highlights around the coils are hydrogels; purple rod is a central pivot supporting plastic piece; light green lines connecting metal strip and nitinol coils are nonelastic threads.

2.3.1 Bistable Metal Strip

2.3.1.1 Metal Strip Shape and Trigger/Reset Angle

Initial studies focused on investigating how the shape of the bistable metal strip and trigger/reset angles impacted its triggering and resetting force. Here, “trigger force” refers to the force required to cause the bistable metal strip to coil rapidly, doing work in the process. “Reset force” refers to the force required to bring the bistable metal strip back to its extended state so that it is ready to be triggered again. In terms of “shape”, we focused on changing the taper ratios of the bistable metal strips while fixing the total length, as shown in Figure 2.6. To measure the forces generated from the snapping action of the bistable strip, an inelastic thread attached to the tip of the bistable metal strip was attached to a force detector, and the trigger/reset forces were measured by pulling the thread (Figure 2.7). When the thread was pulled, a force-time curve was recorded, as shown in Figure 2.8, indicating how forces evolved during the trigger/reset processes. Different pulling rates were tested, and we found that pulling rates had no effect on the minimum force required for trigger and reset (Figure 2.9). A pulling rate of ~5 cm/s was chosen for these experiments due to the ease of reproducibility of this rate. The minimum forces required for trigger and reset were plotted against the taper ratio. We concluded from the data in Figure 2.10 that bistable metal strips with larger

taper ratios yielded smaller trigger and reset forces. When the metal strip had a larger taper ratio, we noticed a flatter surface at the tip, which results in easier actuation due to a smaller force required to transform the tip from one curvature to the other.

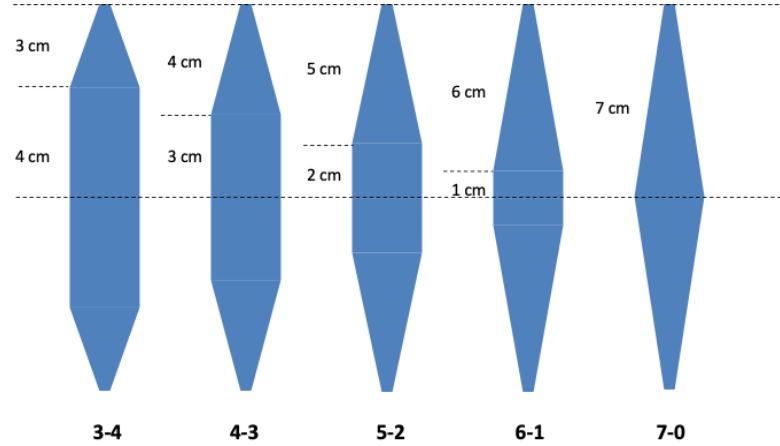


Figure 2.20. Different shape designs of the bistable metal strips. The tips were tapered to a different extent. From left to right, the taper ratio becomes larger. The number below represents the shape of the strip: taper ratio (first number: tapered length; second number: untapered length).

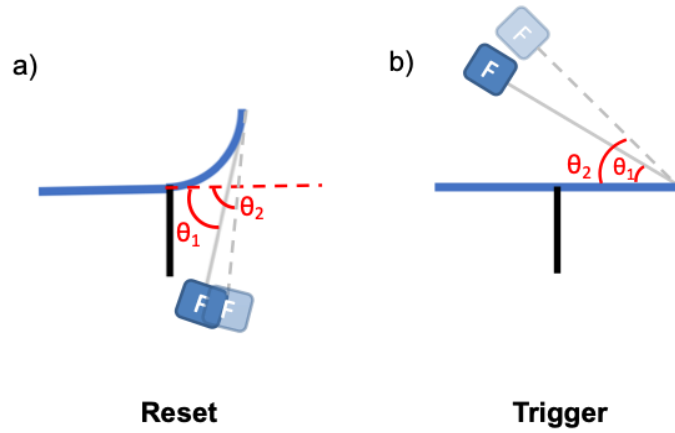


Figure 2.21. Side view illustration of a) reset and b) trigger force tests. The angles are all in reference to the extended position of the metal strip. Theoretically, the angle (θ) can range from 0° to 180° . However, restricted by the device design, the angle is below 90° . (Blue: bistable metal strip; black: pivot fixed onto the middle of the metal strip; silver: pulling thread; box with “F”: force sensor.)

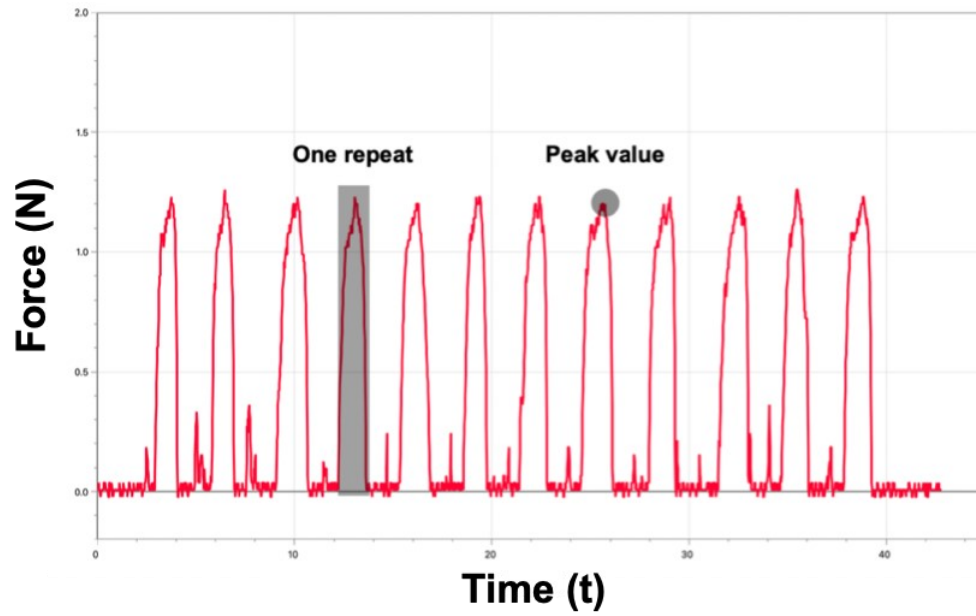


Figure 2.22. Force-Time diagram recorded on Logger Pro software (Reset for 4–3 taper ratio at 60° angle). Each spike represents the force evolution for one test repeat (e.g., dark rectangle). The peak values are picked (e.g., dark circle) and analyzed to represent the force required to reset the metal strip.

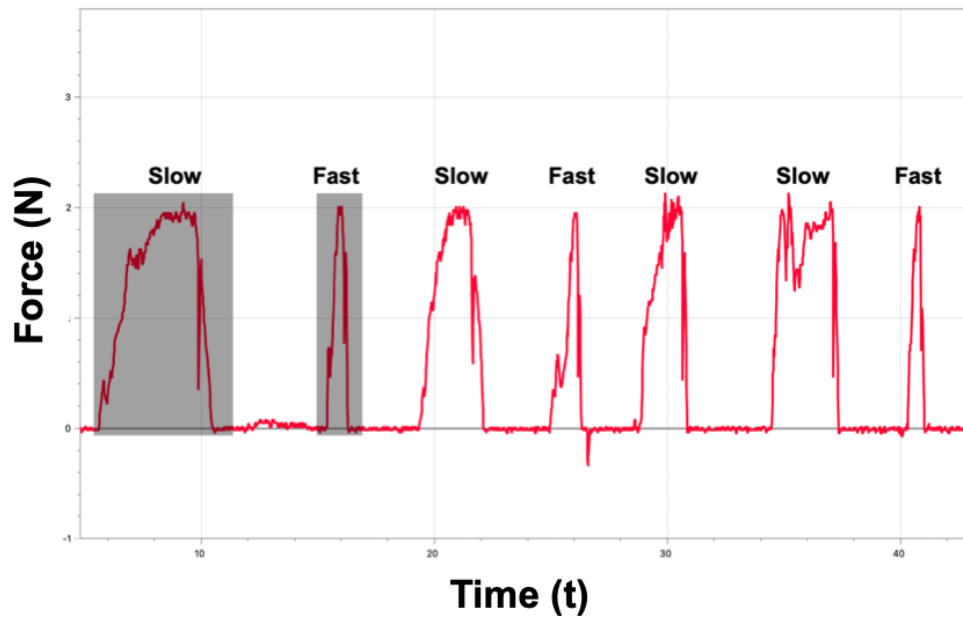


Figure 2.23. Force-Time diagram recorded at different pulling rates. Slow rate was about 2 cm/s, fast rate was about 10 cm/s. Different pulling rates yielded similar peaks indicating similar forces.

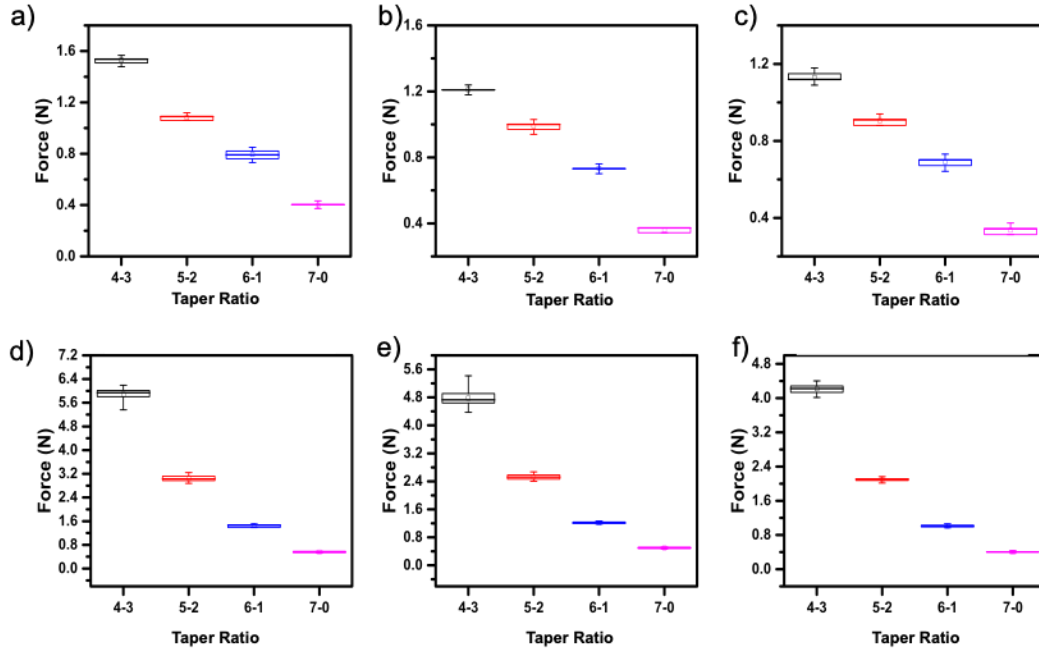


Figure 2.24. Boxplot of reset forces for different taper ratios at certain trigger/reset angles **a)** 50°, **b)** 60°, and **c)** 70°. Box plot of trigger forces for different taper ratios at certain trigger/reset angles **d)** 25°, **e)** 35°, and **f)** 45°. For all the angles, both reset and trigger forces decrease with more tapering on the tip.

Meanwhile, we investigated how the angle that the force was applied to the bistable metal strip, via the thread, impacted the magnitude of the trigger and reset forces. As shown in Figure 2.7, using the extended state of the bistable metal strip as a reference, we varied the angle of force application to trigger/reset the bistable metal strips. Three different angles were investigated for both the trigger and reset processes. As can be seen in Figure 2.11, larger trigger/reset angles led to smaller forces required for triggering and resetting. This could be explained from the force analyses of the process. When the angle of the applied force is large, the effective normal force, which is the projection of the vector force applied onto the tip of the metal, is likewise large. As a result, if the normal force required to trigger or reset the metal strip remains the same, larger angles lead to a smaller vector force required. From this result, we concluded that we can minimize the force by maximizing the angle of force application approaching 90°. However, the angle was limited by the actual reasonable dimensions of the device. For our device design, considering the dimensional constraints and aesthetic aspects, we used 45° for triggering and 60° for resetting.

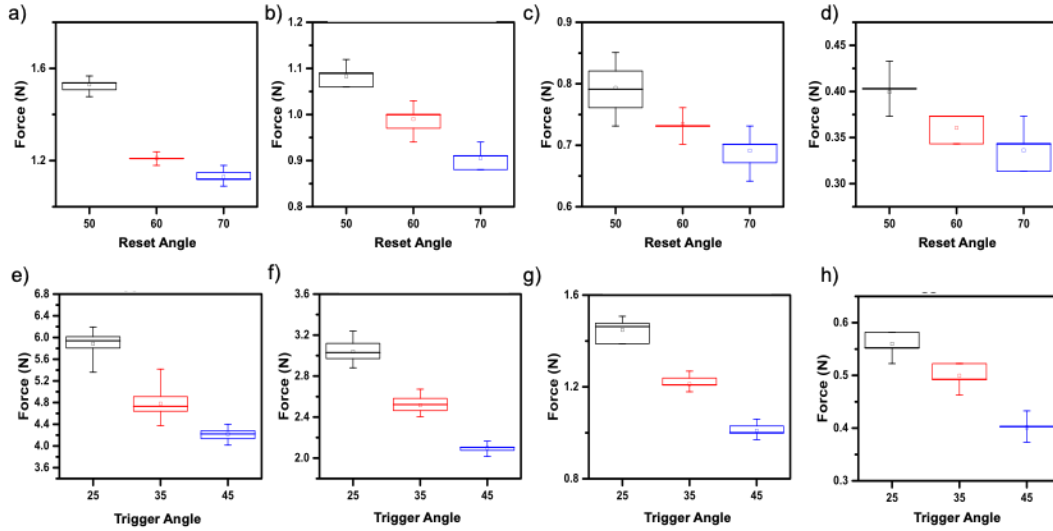


Figure 2.25. Boxplot of reset forces with different angles at certain taper ratios **a)** 4–3, **b)** 5–2, **c)** 6–1, and **d)** 7–0. Box plot of trigger forces with different taper ratios at certain angles **e)** 4–3, **f)** 5–2, **g)** 6–1, and **h)** 7–0. For all the taper ratios, both reset and trigger forces decrease with larger angle.

2.3.1.2. Energy Output

While the previous investigation revealed the impact of the taper ratio of the bistable metal strip on the trigger and rest forces, it also revealed that the taper ratio impacted the energy that can be generated as a result of the snapping process. To better understand the relationship between snapping energy output and taper ratio, we performed energy output tests. Specifically, the benefit of using bistable metal strips for device propulsion is their fast and powerful snapping behavior, which it was hypothesized would lead to fast movement of the device developed here. Hence, we wanted to retain good snapping performance while minimizing the magnitude of the trigger and reset forces. To accomplish this, we used a regular ping pong ball that was hung over the top side of the bistable metal strip, as shown in Figure 2.12. By triggering the tip of the bistable metal strip, the strip snapped, coiled, and struck the center of the ping pong ball, sending it into motion. The ping pong ball then moved in a circular path, like a pendulum, and eventually reached its highest point before swinging back. Assuming no energy loss during the process, the energy output of the bistable metal strip is directly proportional to the maximum height reached by the ping pong ball.

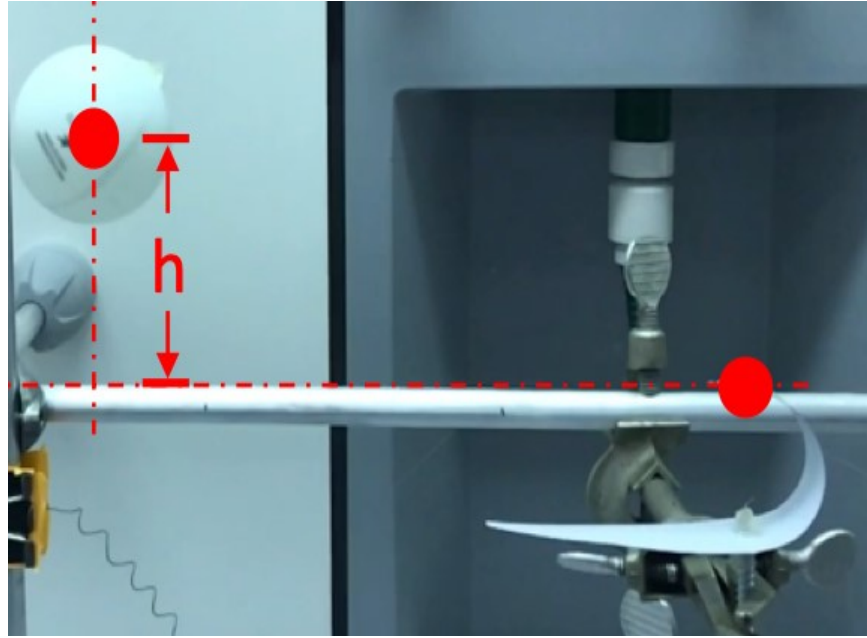


Figure 2.26. Ping pong ball test apparatus for determining bistable metal strip snapping energy output. (Bottom right red dot represents the initial position of ping pong ball; top left red dot represents the highest position the ping pong ball reaches; the height elevation is marked by the vertical height difference between the two positions.)

Analysis of the height the ping pong ball reached as a function of the bistable metal strip taper ratio allowed us to determine the relationship between energy generation and bistable metal strip taper ratio. Figure 2.13 shows the height the ping pong ball can reach (and the energy generated) greatly decreased with larger taper ratios; i.e., larger taper ratios yielded lower snapping energy output. In fact, the 7–0 taper ratio metal strip did not have enough energy to move the ping pong ball. Since snapping energy is essential to the performance of the swimming device, we decided to maximize the energy output by adopting a 4–3 taper ratio design for our future devices.

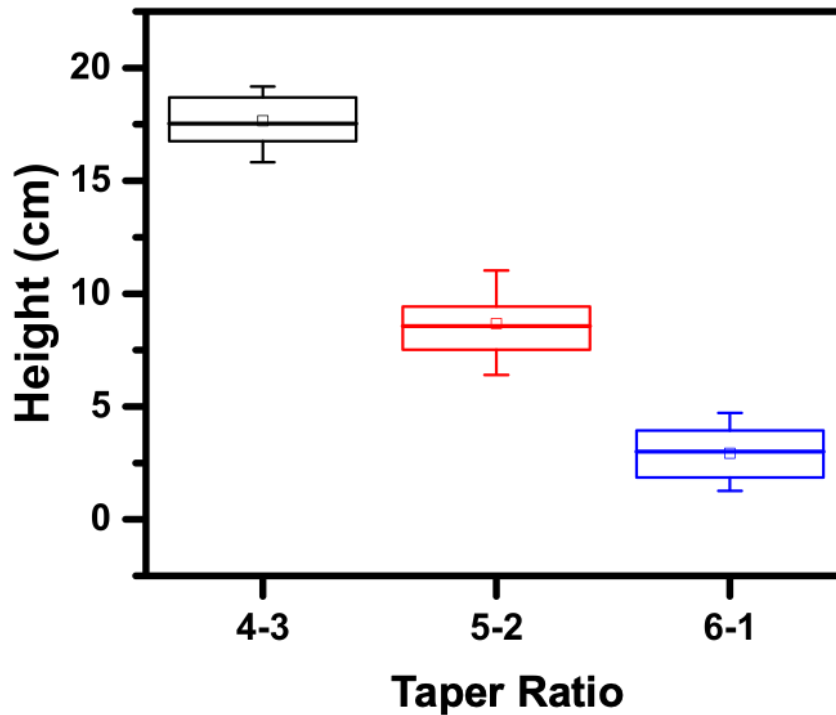


Figure 2.27. Snapping energy of different taper ratios. The figure shows the height the ping pong ball reached for different taper ratios. 7-0 is not included here because the snapping is difficult to reproduce and did not have enough force to move the ping pong ball.

2.3.2 Nitinol Wire

2.3.2.1 Phase Transition Temperature

We first investigated the phase transition process using differential scanning calorimetry (DSC), as shown in Figure 2.14. From the DSC, we observed the phase transition to be ~ 60 °C. We also performed a water bath test on the Nitinol (Figure 2.15(a)). Specifically, the Nitinol was set into a helical structure (contracted state) in a furnace and subsequently stretched into an extended state. Then, the extended Nitinol wire was immersed into a beaker of water for 10 s at various temperatures and taken out for length determination. From the data (Figure 2.15(b)), we observed a sharp length change at ~ 60 °C, which was consistent with the DSC test.

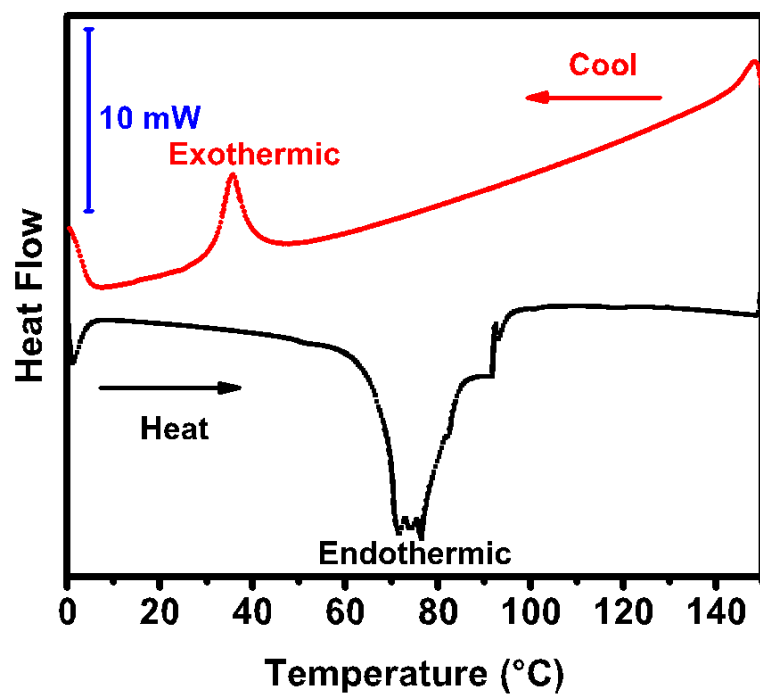
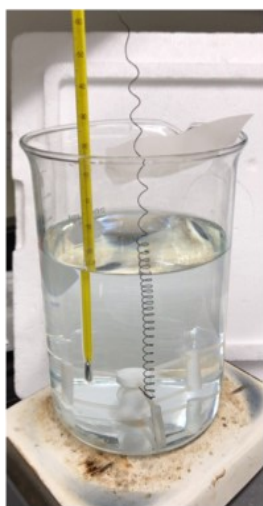


Figure 2.28. Differential scanning calorimetry result for a piece of Nitinol. The black curve is the heating process and red for cooling. The blue scale bar for y-axis represents 10 mW heat flow difference.

a)



b)

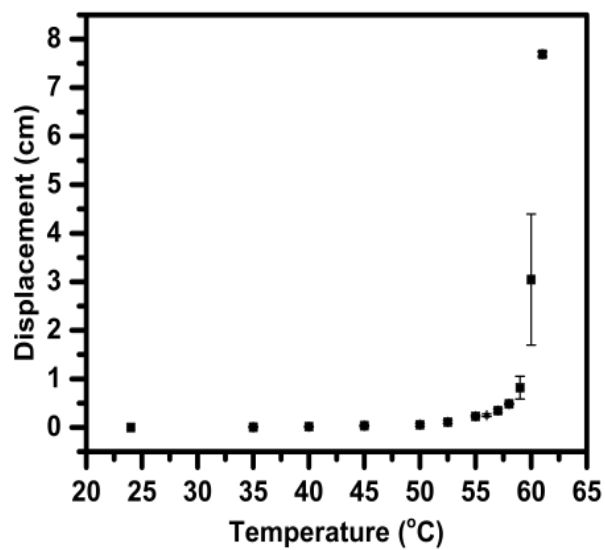


Figure 2.29. a) Setup for water bath actuation temperature test. b) Plot of displacement of Nitinol coil at the indicated temperatures.

2.3.2.2 Actuation Force Output at Different Voltages

The forces that the Nitinol wire can exert upon temperature-induced contraction/shortening determines its ability to apply force to the bistable metal strip for triggering and resetting. Hence, we investigated the force output of the Nitinol wire when stimulated to contract upon application of a voltage, which induced a temperature change above the phase transition temperature. For these experiments, the Nitinol wire was connected to a force sensor and was not allowed to contract upon stimulation (Figure 2.16(a)). Different voltages were applied until the force reached 4.2 N, which was the minimum triggering force for the 4–3 taper ratio bistable metal strip; the 4–3 taper ratio was determined to have optimal performance (see above). Once the mentioned force was reached, the applied voltage was removed, and the Nitinol wire was allowed to cool. As can be seen in Figure 2.16(b), higher voltages applied to the Nitinol decreased the time required for the actuation force of 4.2 N to be reached, which indicated faster actuation, although the higher applied voltage led to an increase in the time required for the Nitinol to cool after removing the applied voltage. This could be explained by considering the Joule heating effect. Assuming that Ohm's Law applies and that the resistance of the Nitinol does not change during the process, when the voltage was higher, the current was higher; thus, more heat was produced in a unit time, allowing the Nitinol to reach its phase transition temperature relatively fast. This excess heat needs to be dissipated from the Nitinol wire to allow for its reversibility (Figure 2.16(c)).

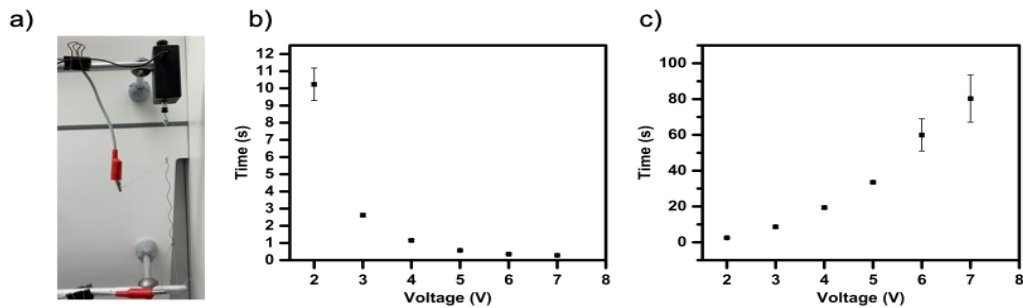


Figure 2.30. **a)** Setup for no displacement actuation test (stretched Nitinol wire tied one end to the hood accessory bar, the other to a force sensor (black); red alligator clips with copper wire to apply voltage onto the Nitinol wire). **b)** Time needed for actuation at different voltages. **c)** Normalized cooling time for different voltages per unit time of heating.

The higher applied voltage led to an increase in the time required for the Nitinol to cool after removing the applied voltage. This could be explained considering the Joule heating effect, which is shown in Equations (1-4).

$$I = U/R \quad (1)$$

$$H = I^2 R t \quad (2)$$

$$\Delta T = Q/(mc) \quad (3)$$

$$Q = H \quad (4)$$

where I is the current flowing through the Nitinol wire; U is the voltage applied; R is the resistance of the Nitinol wire; t is the time period the voltage is applied; H is the heat produced; ΔT is temperature change; m is the mass, and c is the specific heat capacity of the Nitinol wire.

2.3.2.3. Actuation Durability

Durability, such as the number of times the Nitinol can contract/extend upon stimulation before failure, is an important parameter to study for the devices being fabricated here. Here, two sets of consecutive tests were performed using the same setup as in the previous actuation force test (Figure 2.16(a)). The voltage was applied for 10 s and removed to allow the Nitinol wire to cool. From Figure 2.17(a), we observed an ~8.3% force decrease within the first four actuations, followed by a relative stabilization of the force decrease, i.e., an additional 14.8% decrease was observed after the subsequent 82 cycles. Then, the same piece of Nitinol was used to determine its ability to reach the requisite 4.2 N force needed to trigger the 4–3 taper ratio bistable metal strip. From Figure 2.17(b), we can see that the Nitinol wire was able to reach 4.2 N after 222 repeats with no observable failure. Combining two consecutive tests, the Nitinol wire could endure at least 300 cycles of successful actuation. The exact number of cycles to reach failure was not investigated but could be informative if determined in the future.

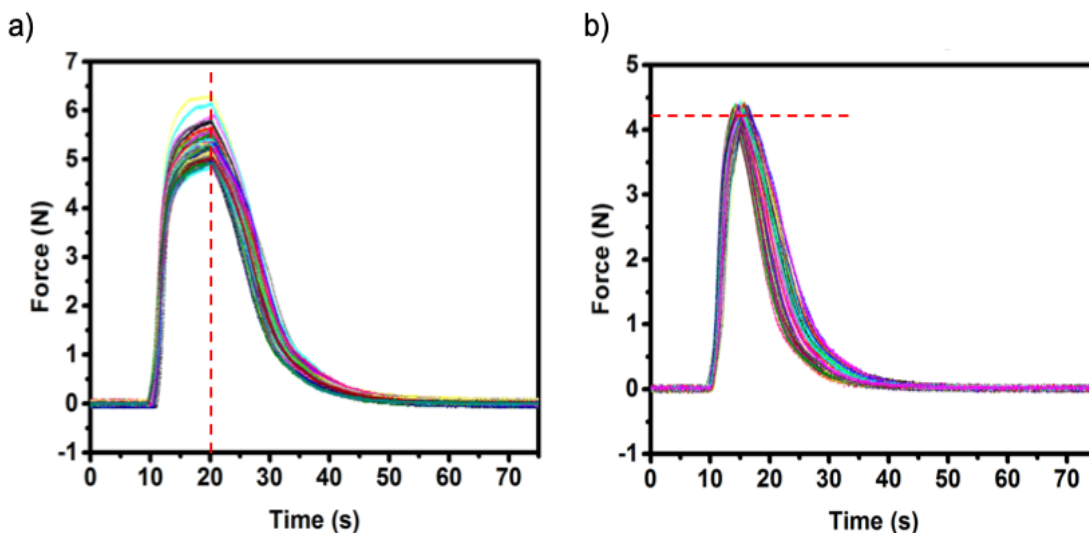


Figure 2.31. a) Force diagram of 10 s of actuation, followed by cooling. Red dashed line represents roughly where the voltage is stopped; 86 repeats were performed. **b)** Force diagram of actuation until reaching 4.2 N (red dashed line) followed by cooling; 222 repeats were performed.

2.3.2.4. Under-Water Actuation

To generate a swimming device, it must be able to operate immersed in water under various water conditions, e.g., temperature and currents. One advantage of having water present is the quick cooling of the heated Nitinol compared to Nitinol in air. This is due to the fact that water has four times larger heat capacity and 25 times larger heat conductivity than air, which is beneficial for multiple consecutive actuations. However, the drawback is that water brings the Nitinol wire temperature down too quickly when the water temperature is low or when there is turbulence. Hence, we performed some actuation tests by immersing the Nitinol wire under water at room temperature and heating by application of a voltage. The results showed that a much higher voltage was required to achieve a similar Nitinol contraction compared to when the Nitinol was heated in air. Also, we clearly can see water convection on the surface of the Nitinol wire, indicating quick and large heat loss (Video S1^b). With a slight turbulence in the water, the Nitinol was not able to actuate at all, even at much higher voltage due to faster heat loss (Video S2^c), which made the actuation process unpredictable and

^b <https://youtu.be/Omji9J9idpA>

^c <https://youtu.be/IKmwzB1BLm8>

uncontrollable. In order to hinder this heat loss process, and to provide the Nitinol wire with a stable, controllable and predictable actuation environment, we coated the Nitinol wire with a layer of polyacrylamide (PAAm) hydrogel (Figure 2.18(a)). A hydrogel was chosen as the coating material because it acts as a physical barrier to hinder the heat loss, but at the same time it can still dissipate the heat since it is a water-rich gel. As seen in Figure 2.18(b-c), with this hydrogel coating, the actuations were observed successfully and were stable even in turbulence, while the one without hydrogel coating completely failed to actuate (Video S3^d-S4^e).

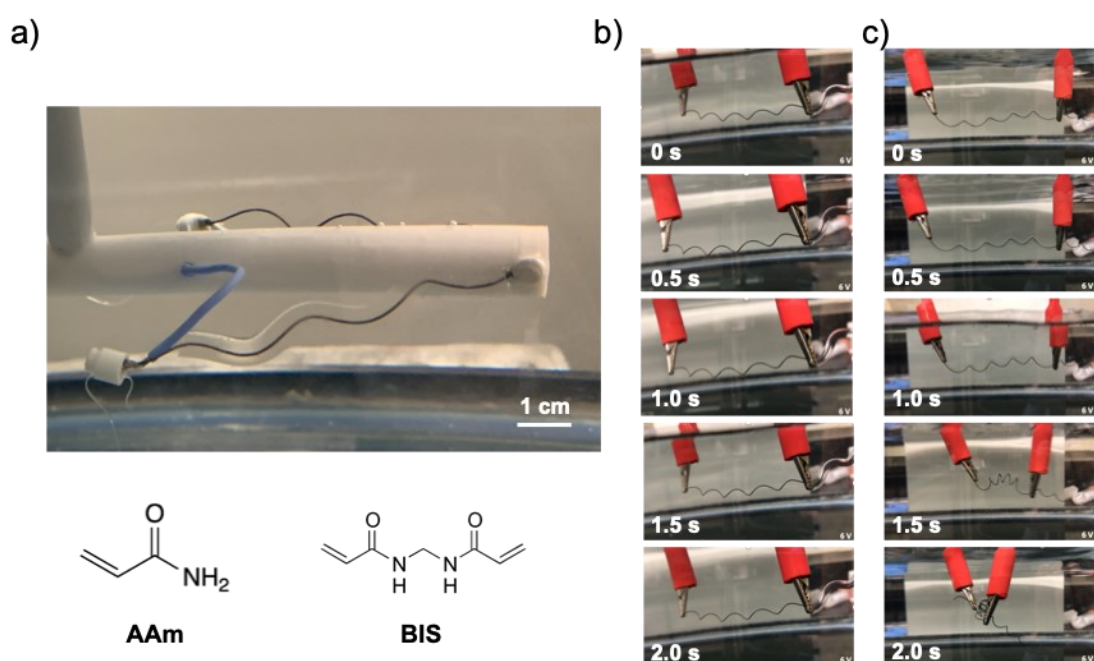


Figure 2.32. a) Polyacrylamide hydrogel coated Nitinol wires (bottom) monomer and crosslinker structures. Snapshots of Nitinol wire actuation under water **b)** without hydrogel coating **c)** with hydrogel coating (see Video S6^f/7^g).

^d <https://youtu.be/mKmGnBUbKsI>

^e https://youtu.be/7g6Vbt_m8-4

^f <https://youtu.be/1KS4wvi23Ek>

^g <https://youtu.be/Ya5AZBZVP8k>

2.3.3. Swimming Device

2.3.3.1. Assembly of the Device

The device was fabricated based on the aforementioned test results. The main body of the device was composed of a bistable metal strip with a pivot point going through the strip perpendicularly. Nitinol wires were connected at both tips of the metal strip against the pivot to set the angle required for triggering and resetting. A wireless control system was designed and assembled, as shown in Figure 2.19(a). To increase the propelling ability, polydimethylsiloxane (PDMS) sheets with rigid plastic (3M PP2950 film) strips embedded were fabricated; these were inspired by fish fins. A lithium ion polymer battery was used as a portable power source.

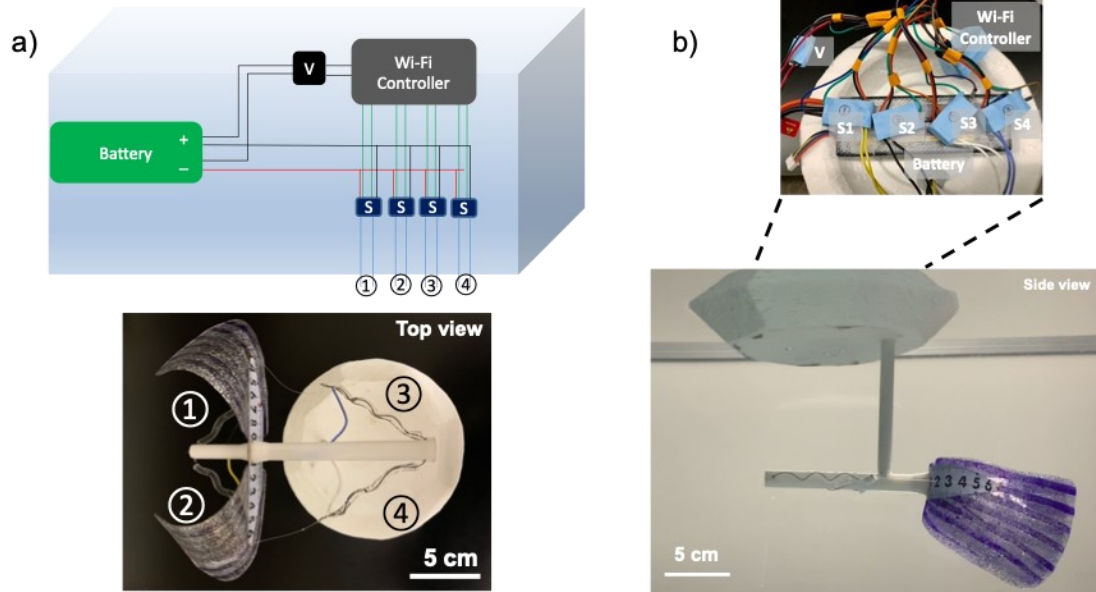


Figure 2.33. a) Illustration of the electronic components and (bottom) top view of the device. b) Device side view in water tank (top: electronic components; bottom: side view of the device).

2.3.3.2 Swimming Demonstration

Swimming behavior was achieved with wireless control and multiple swimming modes (Video S5^h-S7). The swimming device was immersed under water with a styrofoam box floating on water carrying all the electronics (Figure 2.19(b)). By controlling the individual electronic switches, slow movement and faster snapping actions could be

^h <https://youtu.be/HWUxc-8AQSQ>

realized. When both arms were working together, the swimming device could swim forward. When triggered to swim slowly, we determined the swimming speed to be 1.2 cm/s that was calculated based on 4.42–6.04 s in Video S8ⁱ, while it was increased to 5.5 cm/s for fast swimming based on 5.83–7.03 s in Video S9^j. With only one arm working, the device could turn. In the slow swimming speed regime, we observed the device could turn 180° within 10 s, calculated based on 6.36–16.34 s in Video S10^k. By combining different modes of actuation, the swimming device could navigate a water tank easily by swimming straight, speeding up, changing direction, as well as slowing down.

2.3.4 Sensing Application

Microgel-based etalons were constructed by sandwiching poly(N-isopropyl-acrylamide) (pNIPAm)-based microgels between two thin Au layers. In addition to the native thermoresponsivity of pNIPAm, further responsivity can be imparted to microgels via copolymerization. For example, pNIPAm-based microgels can collapse and swell upon heating and cooling, respectively, while also exhibiting pH-and ionic strength-dependent solvation states by incorporating acrylic acid (AAc) into the pNIPAm microgels. Such responsive microgels in etalons allows their visual color and peaks in reflectance spectra to shift upon application of any of these stimuli, allowing the color to be correlated to the composition of the water and its temperature. This is due to the microgel solvation state mediating the distance between the etalon's Au layers, which are responsible for the etalon color; by changing the Au–Au distance, the color of the device changes. We can predict the etalons' optical properties by Equation (5):

$$\lambda = 2nd\cos\theta/m \quad (5)$$

where λ is the wavelength of light being reflected, n is the refractive index of the microgel layer, d is the distance between the two Au layers (thickness of the

ⁱ <https://youtu.be/PXi2tR8L79M>

^j <https://youtu.be/BLofxO30NqQ>

^k <https://youtu.be/B4sMxuI26LI>

microgel layer), θ is the angle of incident light, and m is the order of the reflected peak (e.g., 1, 2, 3,...). As mentioned above, the Au–Au distance (d) can be tuned by exposing the microgel-based etalons to different stimuli. In the work here, we focused on detecting pH and ionic strength changes, yielding a shift in the wavelengths of light reflected from the etalon, and a concomitant visual color change.¹³⁴

2.3.4.1 Device Integration

A 3D printed holder was made to accommodate etalon devices, a camera, and a lighting system. The camera and lighting system were connected to the wireless control module and could take pictures of the etalons to monitor its color change as the water changes pH and ionic strength. The holder was attached to the styrofoam boat body and immersed in water (Figure 2.20(a)).

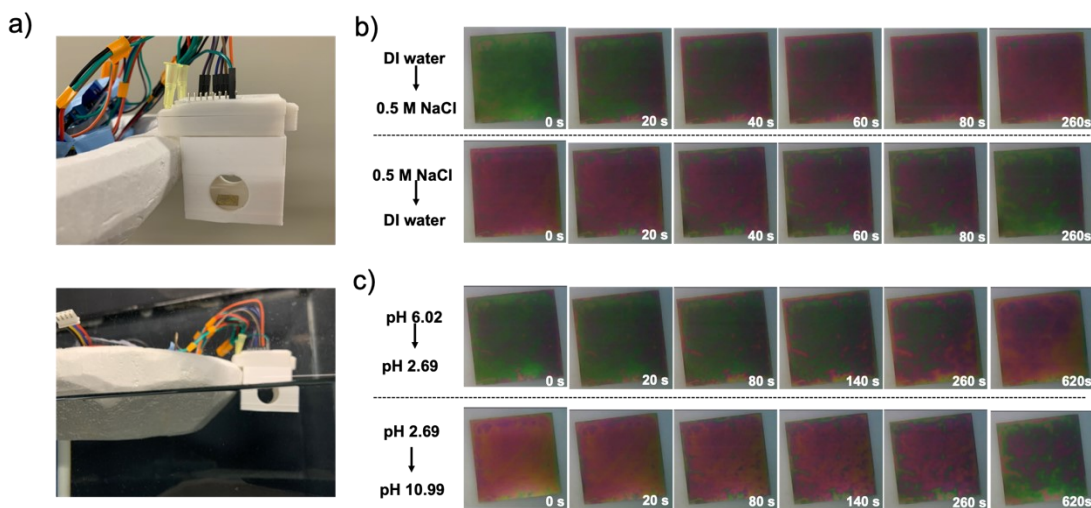


Figure 2.34. a) Pictures of 3D printed etalon holder and assembly (top: in air; bottom: in water). Photographs of etalons b) upon salt addition to water and c) a pH change.

2.3.4.2 Salt and pH Sensing

Etalons with salt and pH responsivity pNIPAm-co-10% acrylic acid (AAc)) were prepared following the group's previous fabrication procedure. After we changed the solution media from DI water to a 0.5 M sodium chloride (NaCl) solution, the color of the etalon chips changed from green to red in 260 s and could return back to green in 260 s when put back in DI water (Figure 2.20(b)). Similarly, when the pH was changed from 6.02 to 2.69, the color of the etalon chips changed from green to red in 620 s and

could change from red to green in 620 s (Figure 2.20(c)). The swimming device served as a platform for different technologies and potentially could be applied in more research areas.

2.4 Conclusions

The first aim of our work was to present an innovative design using bistable metal strip and shape memory alloy Nitinol to fabricate a biomimetic actuator as a swimming device, which exhibited both slow moving and fast snapping capability like an octopus. We hope to inspire more research on combining different materials to achieve novel designs for more applications. Sensing application is just one of the many applications this device can achieve. Remote sampling collecting, video recording, humidity, temperature, and air quality monitoring potentially can all be realized with thoughtful integration. However, we do need to consider the long-time memory loss of Nitinol wire after more repetitions; this was not investigated exhaustively in this work. Future research should look into this and come up with an estimate time for Nitinol wire memory exhaustion. Problems such as how to recharge the battery when the device is far away in the field and how to make sure we do not lose connection when battery runs out should be investigated. More importantly, bio-fouling can be a big challenge for devices that are deployed and immersed in a water environment for long periods of time. Special protective coatings or antifouling design for the device should be investigated.

In summary, a wirelessly controlled, programmable, swimming device was developed. The properties of the Nitinol alloy, bistable metal strips were investigated to find out the optimum design. A hydrogel coating was chosen to provide a stable under-water environment for the Nitinol wires, which facilitates under-water actuation. A fish fin like PDMS flipper also was designed and increased the swimming ability. The swimming device could navigate in all directions, could be controlled wirelessly, and was programmable easily thanks to the untethered design with a portable battery and wireless control module. We also showcased its successful integration with an etalon-based sensing platform, which potentially can inspire more innovative future applications.

Chapter 3

Mimosa Pudica-like Touch-responsive Actuators

3.1 Introduction

Actuators are devices that can convert a source of stimulus into movement; the stimulus can be either physical or chemical in nature, e.g., physical stimuli include pressure,^{93, 97, 113} and electricity,^{135, 136} while chemical stimuli include redox reactions¹³⁷ and pH changes.⁷⁰ Responses of such actuators include expansion,¹³⁸ contraction,¹³⁹ and rotation,¹⁴⁰ which can transform the input stimulus into mechanical energy. By utilizing the mechanical energy generated as a result of the different forms of responses, actuators can do work¹¹⁴ and accomplish complicated tasks.¹⁴¹ Actuators can be used in smart robotics,⁹⁴ switches,¹⁴² and drug delivery systems.¹⁴³ Many research groups have shown that actuators can undergo shape morphing in response to different stimuli, for example, muscle movement by pneumatic tubes,¹⁴⁴ window opening by light,^{145, 146} and drug release by pH changes.¹⁴⁷ However, biomimetic actuators have not been reported on as extensively. *Mimosa pudica* L. (*M. pudica*), also known as the shy plant, can fold its leaves upon physical touch or agitation. Wong and co-workers reported an *M. pudica*-like strip that can fold quickly by adding one drop of water.¹⁴⁸ However, it did not mimic the “touch-responsive” behavior of the plant. In this chapter, we developed an *M. pudica*-like touch-responsive actuator.

In our lab, a *M. pudica*-like touch-responsive actuator was prepared by integrating breakable capsules containing triggering chemicals with stimuli-responsive hydrogels. Specifically, we synthesized a polyacrylamide (PAAm) hydrogel copolymerized with acrylic acid (AAc) using *N, N*-methylenebisacrylamide (BIS) as the crosslinker. Then, the gel was crosslinked secondarily by iron (III) chloride (FeCl₃) to form a second crosslinked network. A *M. pudica*-shaped actuator was fabricated with “leaves” that were constrained by a piece of pre-stretched and Fe³⁺-fixed hydrogel. A wax capsule containing the HCl solution was sandwiched in between. Upon pressing, the wax capsule broke and released the HCl solution, which protonates the acrylate groups, and releases the Fe³⁺. The dissociation of the crosslinking points rendered the

network partially broken and shape recovery of the pre-stretched hydrogel. The opened leaves slowly closed like an *M. pudica* plant, folding its leaves when touched. The detailed mechanism of how this actuation works is shown in Figure 3.1. The elasticity of the hydrogel originates from the resistance of each polymer chain to stretching. According to entropy theories, elastic hydrogels are like rubbers, their polymer chains are treated as entropic springs. When the polymer chain is unstrained, there are many configurations of the chain due to the rotation of the molecules. However, when the long-chain polymer changes from unstrained to the strained state upon application of an external force, configurational entropy of the system decreases dramatically. As a result, when the external force is removed, the spontaneous entropy increase tendency will drive the chains to return to the unstrained state, which is preferable. However, if an intermediate state is introduced between the preferred unstrained state and the unfavored strained state, the strained state can be locked temporarily. To realize this locking effect, the coordination chemistry ($\text{Fe}^{3+}/\text{COO}^-$) provides the solution.¹⁴⁹⁻¹⁵¹ When coordination crosslinking points are formed when the polymer network is strained, the network is crosslinked and fixed in this state locally; the coordination interaction prevents the chain from returning to the unstrained state. However, if the coordination crosslinking points are destroyed by other chemicals (HCl solution here), the network is hinderance free, which can return to the unstrained state automatically driven by entropy increase.

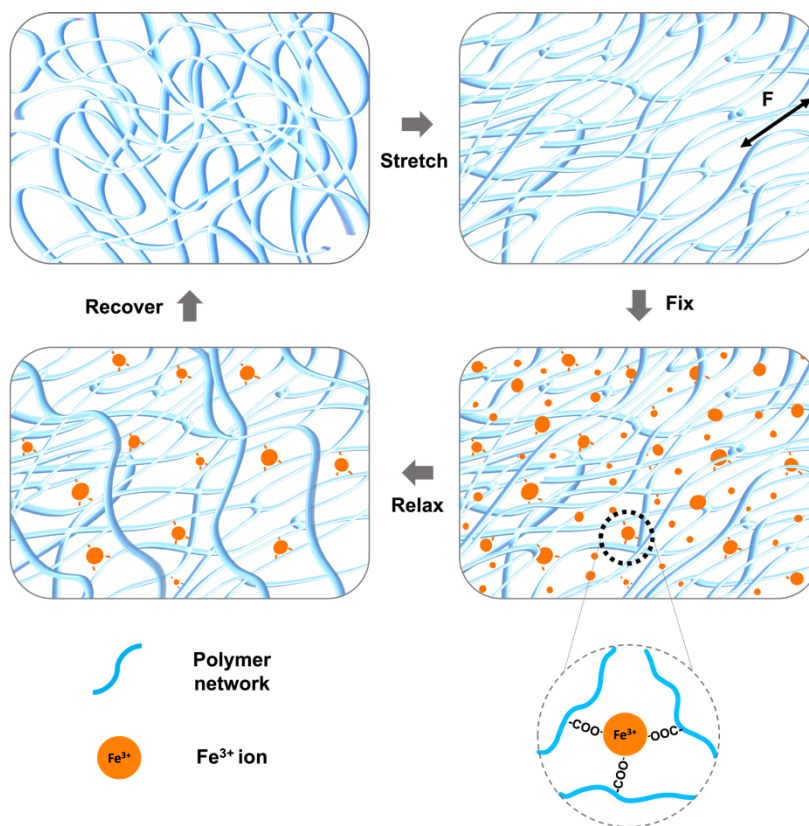


Figure 3.1. Schematic illustration of the actuation mechanism. The polymer network is stretched under an external force. While fixed in the stretched state, the gel is crosslinked by FeCl_3 solution by coordination interaction. The gel is relaxed in DI water, but the coordination interaction prevents the crosslinked area to return to the unstretched state. Finally, when immersed in HCl solution, Fe^{3+} ions are removed, which causes the network to recover to the original shape.

3.2 Experimental Section

Materials: Granular paraffin wax was obtained from ACROS Organics (Fisher Scientific, Waltham, Massachusetts, USA). Hydrochloric acid (HCl, FW/PM: 36.46) was purchased from Caledon Laboratories (Georgetown, Ontario, Canada). Crystal violet (CV, >90.0% anhydrous basis), acrylamide (AAm, >99% (HPLC)), acrylic acid (AAc, 99%), *N, N*-methylenebisacrylamide (BIS, 99%), ammonium persulfate (APS, >98.0%), *N, N, N', N'*-tetramethylethylenediamine (TEMED, 99%), and iron (III) chloride (FeCl_3 , 97%) were purchased from Sigma Aldrich (St. Louis, Missouri, USA). All the chemicals were used as received without further purification, unless otherwise indicated. A hole puncher set was purchased from Owden (Ningbo, Zhejiang, China). Acrylic tape (3M VHB™) and transparency film for plain paper copiers

(PP2950) were purchased from 3M (Saint Paul, Minnesota, USA). Parafilm was purchased from Bemis (Neenah, Wisconsin, USA). The dual-range force sensor and the sensor interface LabPro were purchased from Vernier (Beaverton, Oregon, USA).

Fabrication of Wax Capsules with Entrapped Solution: The fabrication process is shown in Figure 3.2. 100 mL deionized water (DI water) was added to a 250 mL beaker and 5 g wax (paraffin) beads added. The solution was heated until all the wax beads melted and formed a thin layer of liquid wax. 1.0 M HCl solution was taken by a syringe and slowly pushed out of the syringe until a droplet formed at the end of the needle. The droplet was dipped gently into the wax layer that formed a wax layer encapsulating the solution. The wax capsule was removed and cooled until the wax shell was hardened. The needle was rotated slowly to break apart from the wax and left a pore. Then, a blade was heated on the surface of a hot plate and was pressed against the pore that melted the wax and eventually sealed the pore after the wax was cooled. The size of the wax capsule could be controlled by the size of the droplet on the needle.

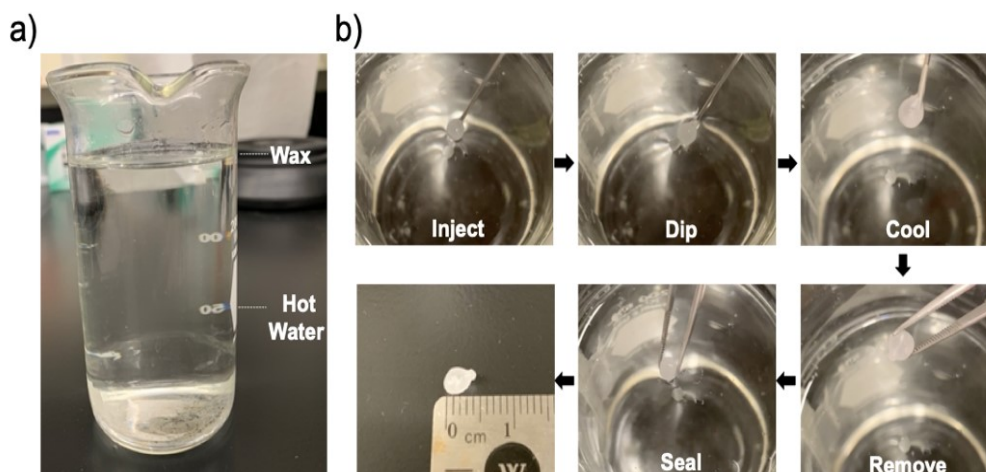


Figure 3.2. Wax capsule fabrication. a) The set up for the fabrication process: a beaker containing hot water and a layer of melt wax; b) the process of fabrication: inject; dip; cool; remove; seal.

Wax Capsule Weight Change Measurement: Individual wax capsules were placed in different Petri dishes and weighed immediately after they were made. Then, the wax capsules were left in ambient air at room temperature for 12 days, and the weight changes were monitored using an analytical balance.

Wax Capsule Break Force Test: A force sensor connected to Logger Pro software was set up before the measurement. Then, the force sensor was handheld upright with the sensor tip at the bottom touching the wax capsule in a Petri dish. A force was applied onto the wax capsule at a rate about 2.3 N/s until the wax capsule broke; the force was recorded during the process. The force diagrams (example shown in Figure 3.3) were analyzed by MATLAB, and the force required for the wax capsule breakage was obtained.

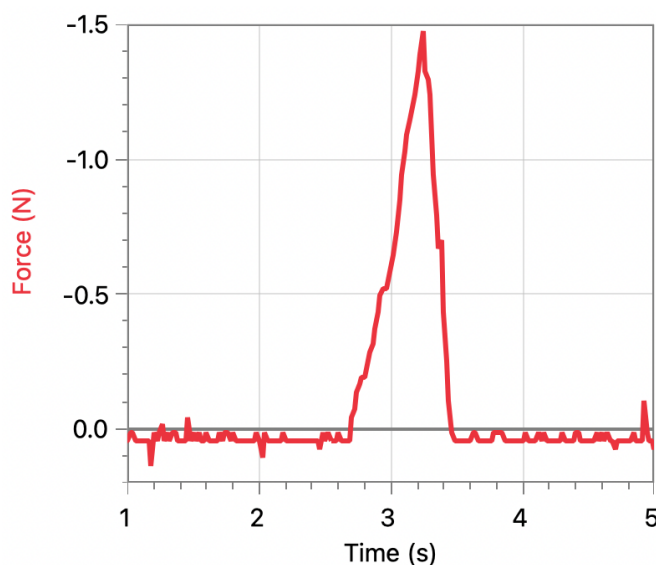


Figure 3.3. Wax capsule break force test. This is one of the capsule force test experiments, which was screenshot directly from the Logger Pro software. x-axis is the elapsing time; y-axis is the force exerted onto the sensor.

Wax Capsule Solution Releasing Test: Before the test, wax capsules with crystal violet solution (visual indicator) incorporated were fabricated using the aforementioned wax capsule fabrication method. One wax capsule was placed into a Petri dish with DI water. The camera was set up to record the releasing process. Then, the wax capsule was pressed till rupture using manual pressing.

Hydrogel Synthesis: Poly(acrylamide-co-acrylic acid) (P(AAm-co-AAc)) hydrogels were synthesized by free radical polymerization. Briefly, 6 g of AAm, 1.5 g of AAac, 30 mg of APS, 8.28 mg of BIS, and 30 mL of DI water were mixed in a test tube and bubbled with nitrogen gas for 5 min. A piece of Teflon™ sheet was cut with a rectangle in the middle to afford a Teflon™ gasket. Then, the Teflon™ sheet was

sandwiched between two pieces of glass slides. One side of glass was slid towards the side and the premade solution was injected into the gasket. The glass was moved back and secured with binder clips. The whole piece was placed on a heating plate at 60 °C overnight. The glass slides were removed, and a piece of P(AAm-co-AAc) hydrogel was obtained.

Hydrogel Stretch and Iron Solution Fixation: The previously synthesized hydrogel was cut it into rectangular shapes using razor blades. Some were made into a ring shape using different sizes of hole punchers. As shown in Figure 3.4, the rectangular hydrogels were placed on a glass slide, stretched towards the end of the glass slide, and fixed in place using binder clips. The ring-shaped hydrogels were hooked onto the tip of an Eppendorf tube and slowly slid until stretched and secured in place around the lid. An iron solution was prepared by dissolving 0.487 g FeCl_3 powder into 50 mL of DI water. The stretched rectangular and ring-shaped hydrogels were soaked in the solution for 30 min. Then, they were transferred to DI water for 3 h. The fixed hydrogels were taken out from the DI water and removed from the clippers and the Eppendorf tube. The resulted hydrogels were ready for further experiments. The hydrogel dimensions before and after the fixation process also were measured.

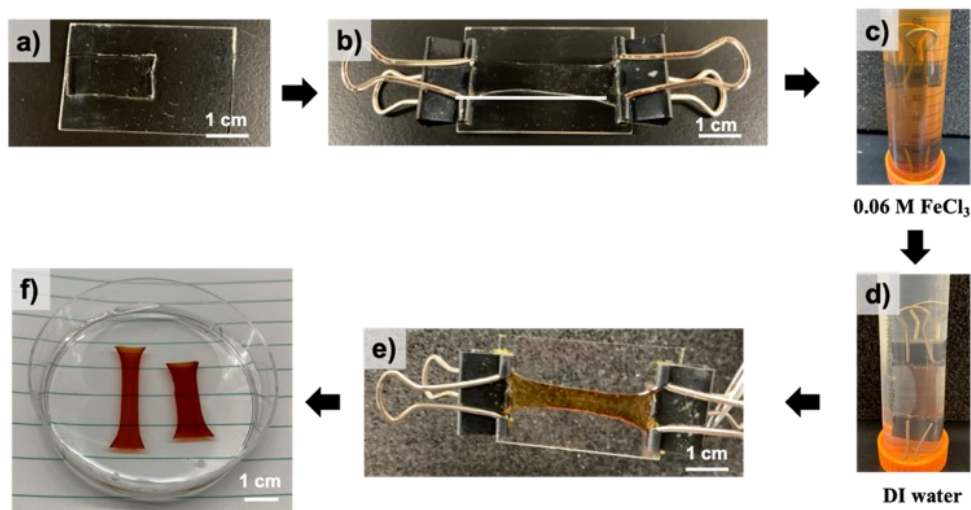


Figure 3.4. Hydrogel fixation process. a) A piece of rectangular hydrogel was placed on top of the glass slide; b) the hydrogel was stretched and fixed using clips; c) the fixed hydrogel was soaked in an 0.06 M FeCl_3 solution for 30 min; d) the hydrogel was transferred to DI water to remove excess Fe^{3+} ions. The crosslinking was rearranged and strengthened during this process; e) the hydrogel was removed from the tube and f) stored in DI water.

Hydrogel Actuation Reversibility and Repeatability Test: The previous mentioned ring-shaped hydrogel was chosen for the reversibility and repeatability test due to less external destruction to the gel during the fabrication process. The rectangular gel fabrication used clips to fix the hydrogel, which could cause cracks, affecting the subsequent fixation process. The Eppendorf was used for the expansion of the hydrogel, which could be performed in a consistent manner. Following a similar experiment procedure as before, the ring-shaped hydrogels were hooked onto the tip of an Eppendorf and slowly slid until stretched and secured in place around the lid. The ring-shaped hydrogels were soaked in the iron solution for 20 min. Then, they were transferred to DI water for 20 min. The hydrogels were taken out from the DI water and removed from the Eppendorf. Then, the gels were soaked in a 0.1 M HCl solution for 20 min. The expansion, fixation, relaxation, and actuation were performed five times; the dimensions of the hydrogels at different stages were measured and analyzed.

Hydrogel Characterization: The hydrogels before FeCl₃ fixation, after FeCl₃ fixation, and after HCl actuation were characterized by scanning electron microscopy (SEM). Three samples from different reaction stages underwent freeze drying process using lyophilizer (brand) for hours (add later). The sample were imaged using (SEM model)

Hydrogel Actuator Fabrication: The previously synthesized rectangular hydrogels were put onto the top of a clean glass slide. Two to three wax capsules were placed onto the hydrogels, and the whole device was wrapped with 3M tape/parafilm. After the wrapping process, some holes were punctured on the 3M tape/parafilm on the wax capsule side to allow DI water to flow, which facilitated the HCl solution diffusion process.

Hydrogel Actuation Test: The whole process was recorded using a camera. A Petri dish with DI water was used as a container. Then, the previously fabricated actuator was immersed into the DI water. A force was applied gently on the wax capsules with the index finger until they break and release the solution inside. The hydrogel actuator was kept free floating, and the shape shifting process was recorded.

***M. pudica* Plant Actuator Fabrication:** A transparency film for plain paper copiers (PP2950) was used to draw and cut out the *M. pudica* shaped actuator. Then,

the actuator was folded in the middle to adopt a permanent half-folded shape. Two pieces of the pre-stretched hydrogels were cut on the two ends with a wax capsule wrapped in the middle. The hydrogel was fixed on the two pieces of leaves, ready for actuation demonstration.

M. pudica Plant Actuator Actuation in Air: The camera was set up to record the actuation demonstration. First, the actuator was put on a piece of paper. Then, the index finger was used to apply the force to break the wax capsule and release the HCl solution inside.

3.3 Results and Discussion

In this chapter, we aimed to mimic the behavior of *M. pudica*, whose leaves fold when touched. The final design we converged on is shown in Figure 3.5. The stimuli-responsive hydrogel was pre-stretched, fixed at a temporary stretched shape using FeCl_3 solution, and attached to a plastic “stem” with two “leaves”. A wax capsule with a trigger solution encapsulated was sandwiched between the stretched hydrogels. Once the wax capsules were broken by a force applied, the trigger solution was released and interacted with the hydrogels, causing the stretched hydrogel to shorten. The shortening of the hydrogels brought the “leaf” closer, resembling the *M. pudica* closing its leaves. Many different designs and actuation scenarios were investigated and discussed in detail as follows.

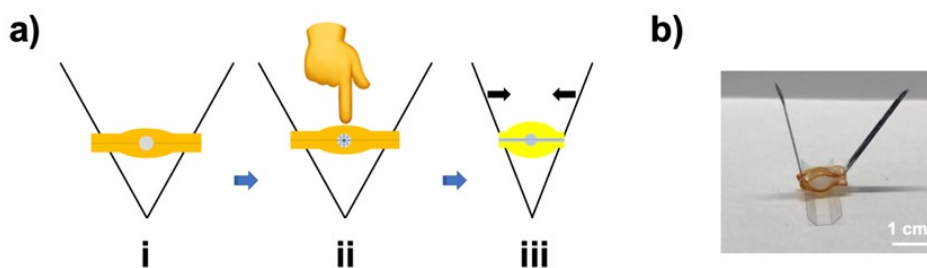


Figure 3.5. Illustration of the touch-responsive actuator. a) Sideview of the actuation process: (i) two pieces of pre-stretched and Fe^{3+} -fixed hydrogel sandwiching a wax capsule containing HCl solution; the two ends of the hydrogel attached to a V-shaped 3M plastic film, mimicking *M. pudica* plant leaves; (ii) fingertip applied pressure onto the hydrogel piece to break the wax capsule; (iii) the wax capsule releasing HCl solution, actuating by shrinking and pulling the two leaves closer; b) the real object of the actuator assembled with the 3M plastic film, pre-stretched and Fe^{3+} -fixed hydrogel, and wax capsule containing HCl solution.

3.3.1 Wax Capsules

3.3.1.1 Trigger Solution Incorporation Amount

The amount of the trigger solution incorporated was not controlled strictly in this study as this process was executed purely by hand. However, the estimated amount can be controlled during the fabrication process and can be inferred from how many drops of liquid were injected from the same syringe and needle. To estimate the incorporation amount more accurately, the wax capsules were weighed before and after they ruptured, and liquid was removed. From Figure 3.6, the majority of the wax capsule trigger solution incorporation was estimated to be ~ 0.0232 g (~ 23.5 μL) per wax capsule.

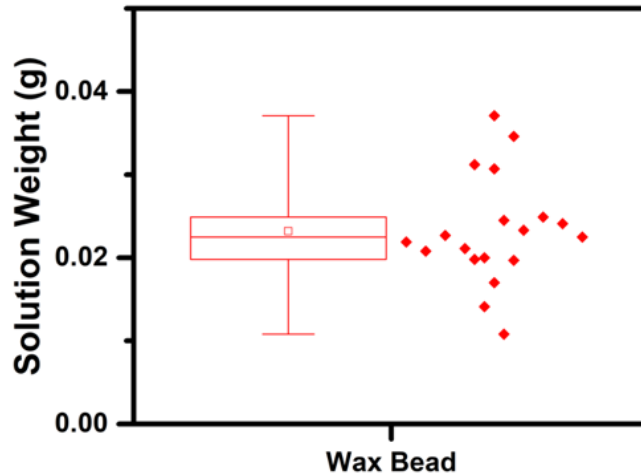


Figure 3.6. Trigger solution incorporation amount of the wax capsules. Left in the graph is the boxplot indicating the data distribution; right is the real data cluster from all the measurements.

3.3.1.2 Sealing Capability

How well the trigger solution is sealed inside the wax capsules before a force is applied to release is an important parameter to control. Since the trigger solution is used to actuate the device, it should not be released before a force is applied. The main reason for using wax as an encapsulation material is its hydrophobicity and low porosity. As a result, the aqueous solution inside will be sealed efficiently inside the capsules. As shown in Figure 3.7, we can see that the weight of the wax capsules with trigger solution inside only decreased by about 2% in 288 h in ambient air. We speculated that the small amount of loss was due to the evaporation of solution through the pores and the possible cracks during wax capsule fabrication and handling. However, some of the

wax capsules, such as capsule #5 and #9, did lose the solution inside faster than others; much faster for capsule #7 and #8. After this weight analysis experiment, visual inspections on the wax capsules were performed. Some large pores and cracks were found on the wax capsules, which might have formed during the manual fabrication process and worsened during the ambient air exposure that resulted in faster drying of the wax capsules.

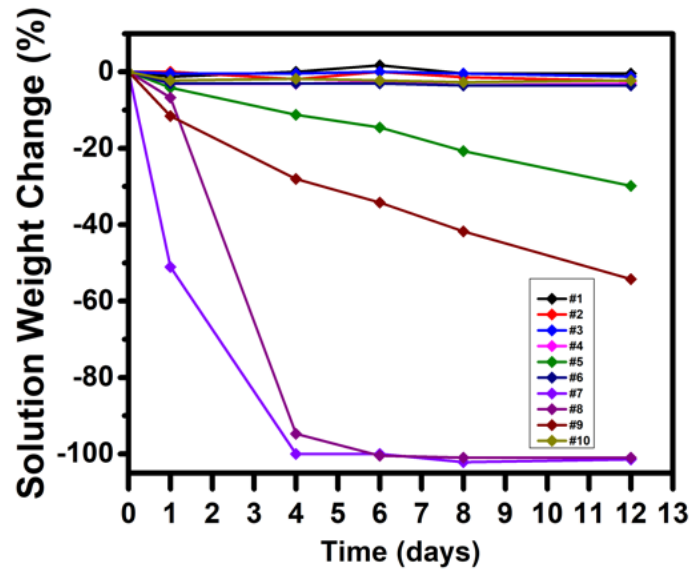


Figure 3.7. A graph showing the solution weight change over time. Different colors representing different wax capsule samples.

3.3.1.3 Wax Capsules Breaking Force

Many factors can affect the force needed to break the wax capsules. For example, the size of the wax capsules, the thickness of the wax shell, how uniform the wax shell is, and what type of surface the wax capsules are pressed against. We noted that first three factors were controllable but inevitable since all the wax capsules were made by hand and the inconsistencies always existed. Considering that the actuator demonstration would be done in a Petri dish, we performed the wax capsule breaking force test in the Petri dish as well. The tests aimed to give an overall understanding of how much force is needed to break a wax capsule. As shown Figure 3.8, we can see that the force required to break the wax capsule was around 1.3 N but with relatively large variations.

As mentioned before, the wax capsule inconsistencies contributed to the variations. If the wax capsule fabrication process can be improved, the variations could be minimized significantly. However, this break force is not crucial to the successful actuation as long as the force is not outside the reasonable force range a human finger can exert.

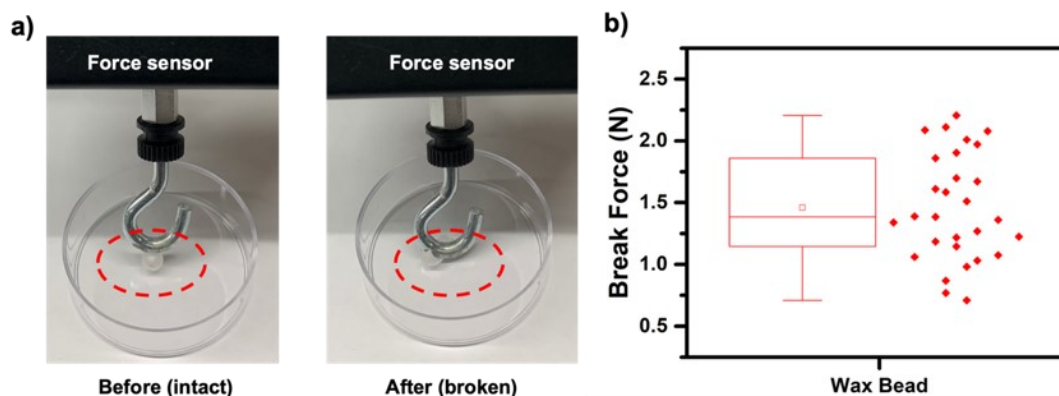


Figure 3.8. Wax capsule breaking force. a) Experimental setup before and after the breakage of the wax capsule (the metal hook is part of the force sensor); b) wax capsule breaking force. On the left in the graph is a boxplot indicating the data distribution; right is the real data cluster from all the measurements.

3.3.1.4 Trigger Solution Releasing upon Force

To better observe the releasing behavior, we performed a releasing test in water using crystal violet as an indicator. From the releasing picture shown in Figure 3.9, we can see that once the force is exerted onto the capsule, rupture happened, and the crystal violet solution was released, giving a vibrant violet color to the water, indicating that the solution inside the wax capsule can be released once the wax capsule is broken.

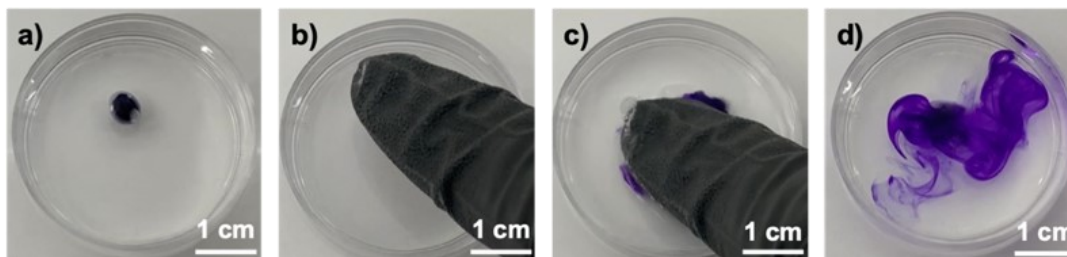


Figure 3.9. Pictures of the press and release process of the wax capsule containing crystal violet indicator solution. a) A wax capsule containing crystal violet was floating on the surface of water in a Petri dish; b) a finger was placed on top of the wax capsule; c) a force was exerted onto the was capsule and ruptured it; d) the crystal violet solution continued to release in water.

3.3.2 Stimuli-Responsive Hydrogel

3.3.2.1 Hydrogel Fixation and Recovery

Hydrogels capable of size/shape fixation by Fe^{3+} solution and actuated upon exposure to HCl solution was an important parameter for the success of actuator design. To understand the hydrogel fixation and recovery behavior, a series of experiments were designed and carried out. The dimensions of the hydrogels were measured before and after the fixation, after DI water soaking, and after HCl solution actuation. As shown in Figure 3.10, for the control group with no stretching, the hydrogel length shortened due to osmotic pressure and Fe^{3+} crosslinking. After DI water soaking, the hydrogel expanded again also due to osmotic pressure that resulted in uptake of DI water. However, after soaked in HCl solution, the hydrogel expanded even more. This could be explained by the breakage of Fe^{3+} crosslinking points, which resulted in further network swelling. For all the hydrogels with different stretching extents, the overall behaviors were the same.

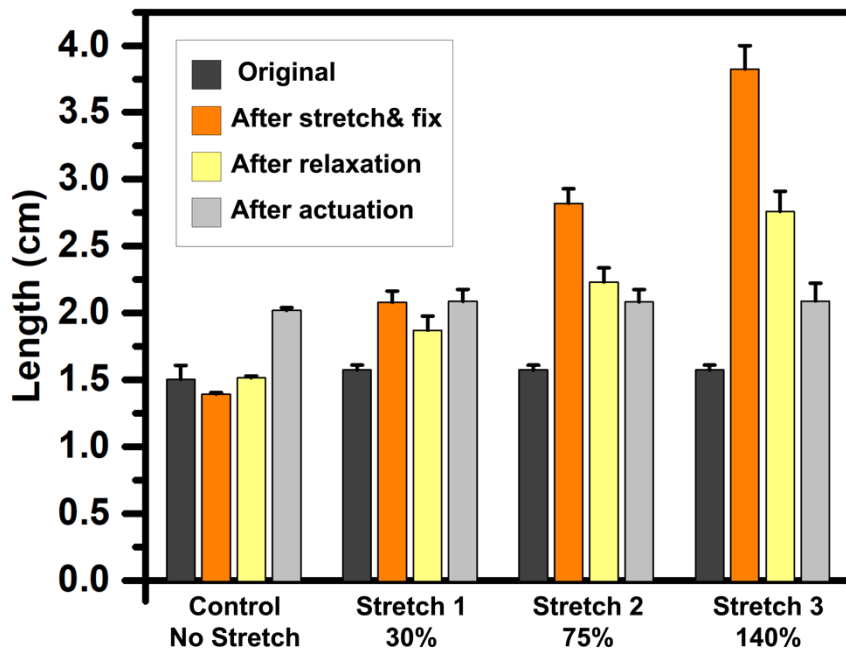


Figure 3.10. Hydrogel dimension changes for different stretching extent after the process of stretch & fix, relaxation, and actuation, respectively. The dark gray bars are the original lengths of the hydrogels; yellow bars are the lengths after FeCl_3^{3+} solution soaking; light yellow bars are the lengths after DI water soaking; light gray bars are the lengths after actuation in HCl solution.

To report the fixation and recovery more quantitatively, the following equations were used.

$$\alpha_{\text{fix}} = L_{\text{DI}}/L_{\text{fix}} \quad (1)$$

$$\alpha_{\text{rec}} = L_{\text{adj}}/L_{\text{HCl}} \quad (2)$$

$$L_{\text{adj}} = L_{\text{orig}} \times a_{\text{swell}} \quad (3)$$

$$a_{\text{swell}} = (L_{\text{HCl}} - L_{\text{orig}})/L_{\text{orig}} \quad (4)$$

where α_{fix} is the fixation ratio; L_{DI} is the length after DI water soaking; L_{fix} is the length after fixation in FeCl^{3+} solution; α_{rec} is the recovery ratio; L_{adj} is the adjusted length based on the swelling behavior of the control samples; L_{HCl} is the length after soaking in HCl; L_{orig} is the original length of the samples, and a_{swell} is swelling ratio of the control samples.

For the control samples, the swelling ratio is about 34%. The fixation ratios for 30%, 75% and, 140% stretch extent were 90%, 80%, and 72%, respectively. We can see that with larger shape change before fixation, a smaller fixation ratio was obtained. This can be explained by the elastic network relaxation. When the shape change is small, the polymer network displacement and stretching is small, thus, a smaller internal elastic energy. When the hydrogel was stretched too much, the internal elastic energy would overcome the Fe^{3+} crosslink fixation, which led to a low fixation ratio. It is worth noting that the recovery ratios were calculated to be 97% for all three different stretching extents. This meant that despite the different stretching extents, all the hydrogels were able to recover to their original shapes, which indicated that no network breakage happened during stretching process, given the stretching extent is kept below 140%.

3.3.2.2 Hydrogel Actuation in HCl Solution

The hydrogel actuation behavior was investigated. As shown in Figure 3.11, hydrogels immersed in HCl solution slowly recover to their original shape. For these ring-shaped hydrogels, the recovery process was completed within 30 min. The color change from dark orange to light yellow during the process indicated that the Fe^{3+} ions were removed from the network. The shrinkage of the ring inferred the elastic energy being released upon actuation.

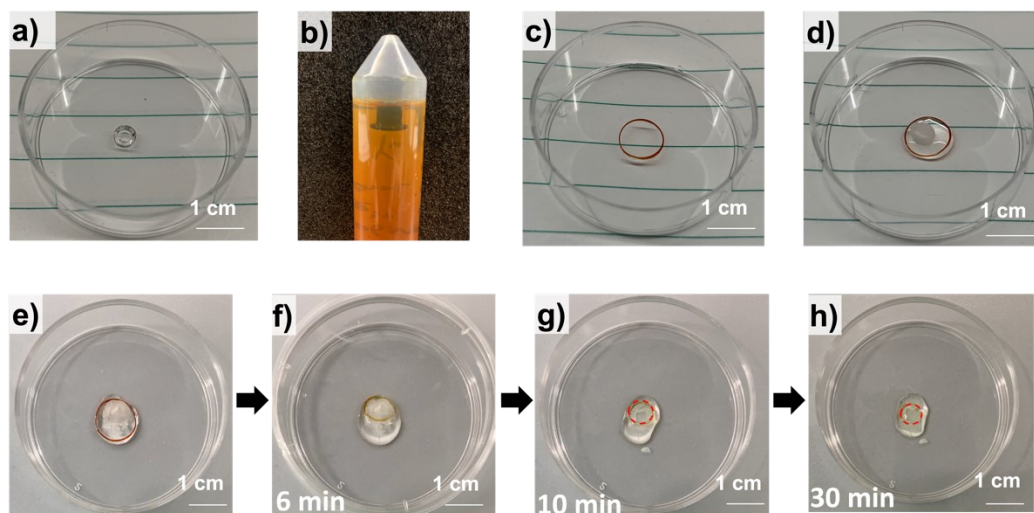


Figure 3.11. Hydrogel fixation in FeCl_3^{3+} solution and actuation in HCl solution. a) A ring-shaped hydrogel was cut from a big piece of hydrogel using the hole punch tool; b) the hydrogel was expanded on a cap and immersed in FeCl_3^{3+} solution; c) the fixed ring-shaped hydrogel; d) some DI water was dropped in the ring, and a wax capsule containing HCl solution was placed in the middle; e) the wax capsule was pressed till rupture; f–h) the ring-shaped hydrogel in contact with the HCl solution released from the wax capsule after 6 min, 10 min, and 30 min, respectively. (In g and h, hydrogels were outlined by a red circle to better visualize since the orange color faded.)

3.3.2.3 Hydrogel Actuation Reversibility and Repeatability

The hydrogel actuation behavior was investigated in terms of reversibility and repeatability. As shown in Figure 3.12, hydrogels can expand reversibly and recover after Fe^{3+} fixation and HCl actuation. The process could be repeated without a noticeable performance drop over at least five cycles. In the first cycle, the freshly made hydrogel was used. As seen at the end of the first cycle, the final dimension is about 33% larger than the original dimension, which agreed with the hydrogel fixation and recovery calculation in Section 3.3.2.1. After the first cycle, the dimension stayed the same for all cycles after HCl actuations.

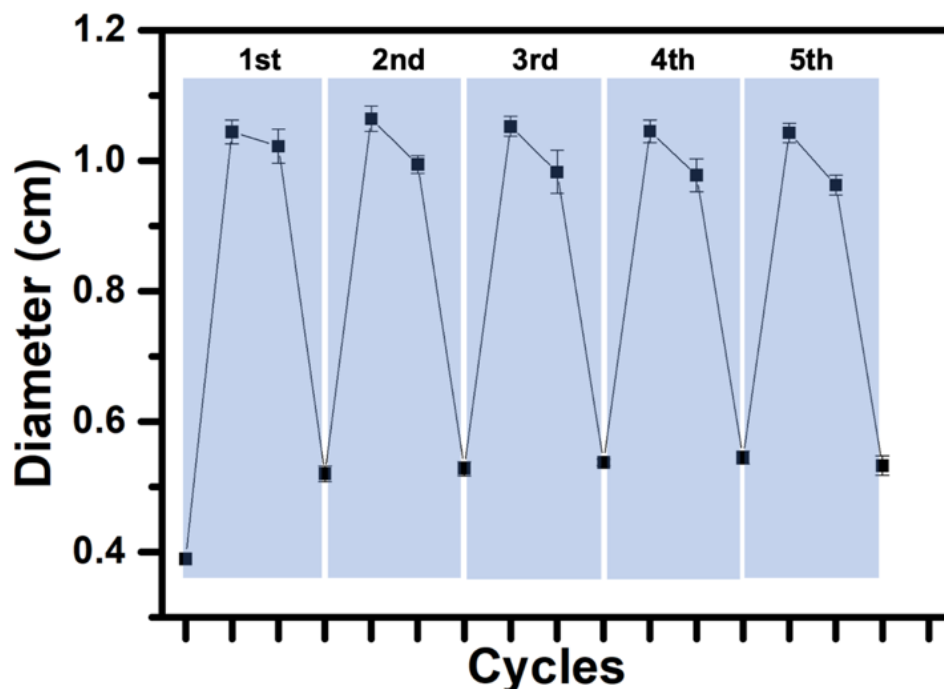


Figure 3.12. Ring-shaped hydrogel actuation repeatability. The first cycle was tested starting with the freshly made hydrogels; the hydrogels were hooked onto an Eppendorf and fixed in Fe^{3+} solution; the fixed hydrogels were soaked in DI water for relaxation and polymer chain rearrangement; the hydrogels were soaked in HCl solution for actuation. For the rest of the cycles, the same hydrogels were used repeatedly.

3.3.2.4 Hydrogel Morphology Change

The hydrogel samples from different reaction stages were imaged using SEM. As shown in Figure 3.13, hydrogels showed different morphologies. The freshly made hydrogel showed undistorted mesh structure (Figure 3.13 a). However, after stretching and Fe^{3+} -fixation, the hydrogel showed elongated mesh structure (Figure 3.13b). After HCl solution soaking, the hydrogel recovered to its original morphology, showing undistorted mesh structure again. The SEM images of the hydrogels at different stages provided a deep understanding of the morphology change of the hydrogels from a microscopic point of view. It also indicated that the hydrogel mesh structure was fixed by the Fe^{3+} ions at a microscopic level. Meanwhile, the structure was not destroyed during the stretching, fixation, and recovery process, which accounted for the repeatability of the actuation process even after multiple repeats.

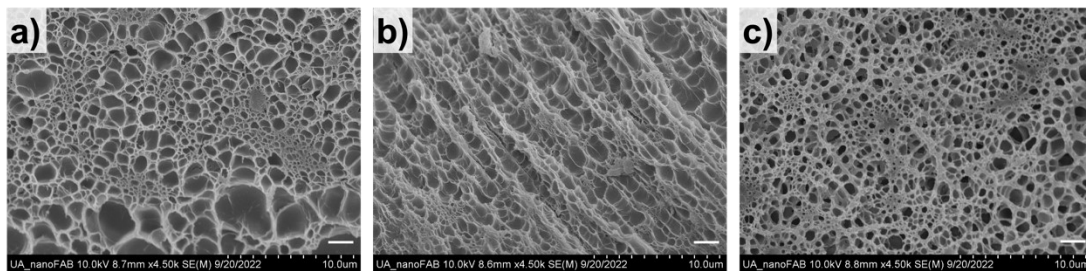


Figure 3.13. SEM images of the morphology of the hydrogel at different actuation stages. a) Freshly prepared hydrogel sample before stretching and Fe^{3+} -fixation; b) the hydrogel after stretching and Fe^{3+} -fixation; c) the hydrogel after HCl solution soaking and recovery. (Scale bar represents 1 μm for all the pictures.)

3.3.3 Touch-Responsive Actuator

3.3.3.1 Actuator Assembly

For the rectangular shaped hydrogel, the key step for a successful actuator assembly was the incorporation of round shaped wax capsules into/onto a thin layer of hydrogel in a way that the capsules can stay in contact with the hydrogel, and the trigger solution inside can interact directly with the hydrogel upon breakage. The first method was to use Parafilm. As shown in Figure 3.14, the film wrapped around the hydrogel closely with wax capsules inside. The second method was to use 3M VHB tape. Similarly, we wrapped the tape around the hydrogel with wax capsules inside. The two methods yielded similar actuator constructions.

3.3.3.2 Actuation Demonstration

To mimic the actuation process of a touch-responsive plant, the as-assembled actuators were tested under a similar process. The actuators were placed in DI water, floating to mimic the leaves of the plant that are free of constraints. A force was applied by fingertip to break the wax capsules inside the actuators, and the actuation process was observed.

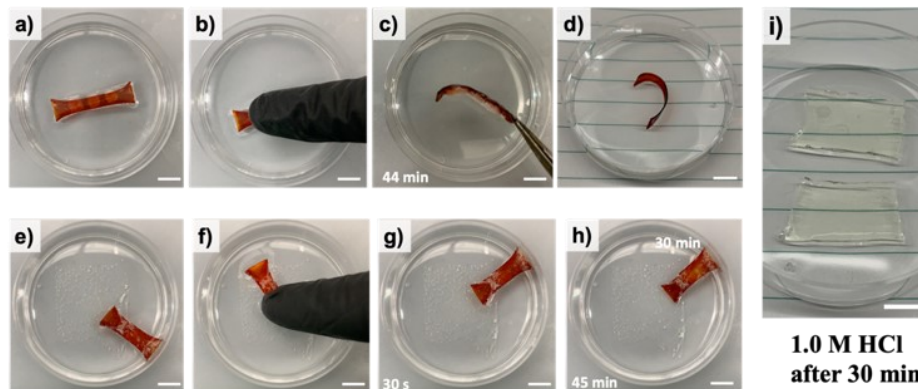


Figure 3.14. The actuation process for actuators wrapped in Parafilm and VHB tape. a-d) Actuator wrapped in Parafilm; e-h) actuator wrapped in VHB tape; i) the two pieces of hydrogels were unwrapped from the film and soaked in 1.0 M HCl solution after 30 min. (Scale bar represents 1 cm for all the pictures.)

Interestingly, the actuation processes were different between the two actuators. As shown in the Figure 3.14, we can see different behaviors in terms of shape morphing. The VHB tape wrapped actuator shortened slowly during the actuation process, while the Parafilm one bent slowly towards the side with wax capsules attached. To explain these distinct behaviors, we should understand how hydrogel shape deformation works. In this case, from the microscopic view, the recovery of pre-stretched hydrogel resulted from Fe^{3+} ions dissociating from the network that served as crosslinkers in the polymer network. When wax capsules broke and released HCl solution to the hydrogel, a relatively high concentration of protons started to protonate the acrylates, displacing the multivalent Fe^{3+} ions, which led to a breaking of the crosslinks. The previously locked polymer chains started to move back to the conformation that they were at before the stretching process due to the elastic energy stored. We can observe that the hydrogel in contact with HCl solution started to shorten. However, the HCl dissipation is a diffusion process, which takes time and can be affected by the surrounding environment. Water media can facilitate this ion exchange process. When the actuator was wrapped in VHB tape, water can move freely across both sides of the hydrogel, facilitating the Fe^{3+} displacement process. As a result, the actuator shortened equally on both sides that showing an overall shortening behavior. However, the actuator wrapped by Parafilm was not able to do effective ion exchange on the side with no capsules. As a result, the actuator was able to shorten only on one

side. Due to the imbalance caused by asymmetric strain, the actuator bent towards the side with wax capsules.

3.3.4 *M. pudica*-like Touch-responsive Actuator in Air

3.3.4.1 Actuator Design and Assembly

An actuator that needs to be immersed in water during the whole actuation process is not practical and does not resemble the actual *M. pudica* plant in real life. To mimic the realistic *M. pudica* plant appearance and its behavior best, we came up with a design as shown in Figure 3.15. The design was a large piece of leaf composed of a stem and a pair of small leaves. The pair of leaves was connected by a piece of “turgor”, which was made from two layers of pre-stretched and Fe^{3+} -fixed hydrogels fabricated previously. Sandwiched in between was a wax capsule containing trigger solution. The leaves stay unfolded before actuation.

3.3.4.2 Leaf Folding Demonstration

As shown in Figure 3.15, upon touch and breakage of the wax capsules, the leaves of the plant started to fold. Due to a capillary force, the released trigger solution slowly spread and wet the whole piece of the hydrogel slowly, shortened the stretched hydrogel, and brought the small leaves on the opposite sides closer. This whole process resembles the *M. pudica* plant’s leaf folding behavior when touched. As can be seen in the picture, the dark orange yellow hydrogel turned light yellow upon interaction with HCl solution; the color change was drastic in the first five min. The angle measurement in Figure 3.15 (i) agreed with the observation, showing a faster response in the beginning, which slowed down gradually. At the end of the actuation process, the hydrogel was detached from the leaf, causing a large angle change. This inferred that the hydrogel was pulling the two leaves together, withstanding the elastic energy of the leaves trying to open.

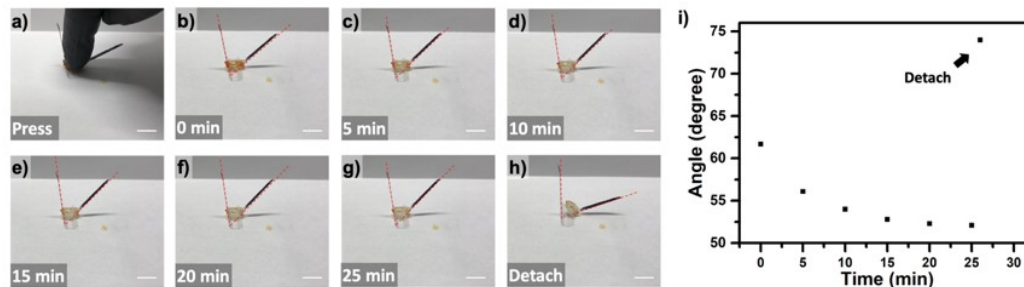


Figure 3.15. *M. pudica* leaf folding demonstration. a) Fingertip applied pressure to break the wax capsule inside; b-g) the HCl solution released to trigger the leaf folding for 0 min, 5 min, 10 min, 15 min, 20 min, and 25 min, respectively; h) manually detaching the hydrogel from the leaf, resulting in the leaf unfolding due to the intrinsic elastic properties of the 3M plastic film; i) the angle measurement between the two leaves during the actuation process. (Scale bar represents 1 cm for all the pictures.)

3.4 Conclusions

In this chapter, we explored the touch-responsive actuators to mimic the behavior of *M. pudica* plant, whose leaves fold when touched. We fabricated an AAm hydrogel with AAc as comonomer, which can be stretched and fixed at the stretched state using FeCl^{3+} solution. Due to the strong coordination interactions between Fe^{3+} ions and acrylate functional groups, the pre-stretched hydrogel could remain in the stretched state without recovery. During this process, the elastic energy was stored in the network. When HCl solution was used as a competitive reagent to displace Fe^{3+} ions from the network, the crosslinking points broke, resulting in elastic energy release and recovery of the hydrogel shape. The stretching, fixation, and recovery processes were reversible and could be repeated. We managed to explore different constructions of the actuators and demonstrated the actuation both in water and in ambient air. The final constructs resembled the *M. pudica* plant, showing the touch-responsive behavior.

However, there still are many problems to solve before a highly optimized Mimosa Pudica plant like actuator can be obtained, for example, the hydrogel drying issues. The hydrogel, if not isolated from ambient air, will dry out slowly, which will result in failure for actuation. In our research, we investigated both 3M acrylic tape and parafilm as a wrapper to protect the hydrogel. However, they only solve the problem partially as both materials can hinder only the water loss instead of 100% prevention, let alone the tedious and finicky wrapping process during fabrication. Moreover, how to achieve a reversible behavior of the *M. pudica* plant is a difficult problem to solve.

As we know, after the touch, when it is “safe” again, the plant will reopen its leaves. In this research, we could re-stretch the hydrogel, fix it with FeCl^{3+} again, and incorporate another wax capsule; the actuator will be ready for the next touch-responsive actuation. However, how to achieve this opening without an external force intervention still remains a difficulty in biomimetic actuator research area.

Our research provided some insights in how to use known chemistry to design and construct actuators to mimic *M. pudica* plants. With a discussion of the opportunities and challenges, hopefully, this could inspire more novel research in related areas.

Chapter 4

Temperature- and Magnetic Field-responsive Actuators for Cargo Transportation

4.1 Introduction

Stimuli-responsive materials are capable of responding to changes in their environment, such as temperature, electric field, magnetic field, redox reaction, light, pH, and salt.^{70, 93, 97, 113, 135-137}

Hydrogels, which are defined simply as three dimensional networks of cross-linked polymer chains with high water content, can be made into an important subset of stimuli-responsive (smart) materials. Stimuli-responsive hydrogels undergo changes in volume in response to external stimuli, corresponding to a reversible phase transition from a swollen, solvated state to a de-swollen, collapsed state. This reversible volume change can be harnessed for various actuation applications.

Temperature-responsive hydrogels composed of poly (N-isopropylacrylamide) (pNIPAm) are the most studied stimuli-responsive hydrogels. PNIPAm is attractive to use due to its tunable properties, such as swelling extent, hardness, and additional functions when copolymerized with other monomers, biocompatibility, and physiologically relevant lower critical solution temperature (LCST) at around 32 °C where the hydrogel undergoes the swollen to de-swollen transition.⁷⁸ This volume decrease that occurs in response to heating the gel above the LCST is the basis for pNIPAm-based actuators.

However, significant challenges still prevent pNIPAm-based hydrogels from mainstream use. First, the volumetric rate of change of pNIPAm is limited by the slow diffusion of water in and out of the gel.^{152, 153} To increase the response rate, researchers have synthesized porous gels with a higher surface area for diffusion of water. However, many methodologies are often complicated.¹⁵⁴⁻¹⁵⁶ Besides, these approaches create pores that are too small for macroscopic usages, such as cargo capturing. Thus, there is still a need to develop accessible methodologies for producing fast responding porous hydrogels as well as endowing the hydrogels with additional functions. In this

chapter, we propose an inexpensive and simple way to produce porous pNIPAm hydrogels using wax template beads. Different sizes of pores also were prepared and characterized to investigate the cargo capturing capability when the gel undergoes expansion and shrinkage.

Secondly, in this chapter, we demonstrated that external fields can be utilized to heat the pNIPAm hydrogels. This is to provide another triggering mechanism, as opposed to heating of the hydrogel's bulk solution, which is inefficient and impractical. To accomplish this, a temperature- and magnetic field-responsive material was synthesized by incorporating magnetic particles into the pNIPAm hydrogel. The materials can be heated via the magneto-thermo effect when placed in an alternating magnetic field (AMF).¹¹³ Since the magnetic field is highly penetrative, actuation of the hydrogel can be triggered remotely by an AMF. On the other hand, due to the magnetic particles embedded inside, the hydrogel can be guided remotely by an external magnetic field to navigate through space.

Ant man in the Marvel movie can change his size freely. He could seize a target, shrink into a small size, navigate through obstacles, and release the target when it's safe. The goal of this chapter is to mimic this behavior by synthesizing a porous temperature- and magnetic field-responsive pNIPAm hydrogel actuator capable of cargo capture and release. The porous structure of the hydrogel that was intended originally for enabling a faster response now also serves as a vacant channel for cargo capturing; the cargoes first move to the pores of the swollen hydrogel. The hydrogel can undergo volume shrinkage that captures the cargoes via local heating above the LCST by AMF. A magnet can be used to guide the shrunken gel through space. At the destination, the AMF is removed, rendering the hydrogel swollen and the cargo released.

4.2 Experimental Section

Materials: N, N-methylene bisacrylamide (BIS, 99%), potassium persulfate (KPS, 99%), N, N, *N'*, *N'* - tetramethylethylenediamine (TEMED, 99%), and iron (III) chloride (97%) were purchased from Sigma Aldrich (St. Louis, Missouri, USA). Iron (II) chloride tetrahydrate (98%) was purchased from Fisher Scientific (Waltham,

Massachusetts, USA). The N-isopropylacrylamide monomer (NIPAm) (MW = 113.16 g/mol) was obtained from TCI Chemicals (Tokyo, Japan) and was recrystallized in hexane before use. Granular paraffin wax was obtained from ACROS Organics (Fisher Scientific, Waltham, Massachusetts, USA). Sylgard 184 silicone elastomer base and Sylgard 184 curing were obtained from Dow (Midland, Michigan, United States). All the chemicals were used as received without further purification, unless otherwise indicated.

PDMS Mold for Wax Template Beads: Plastic beads and glass beads were purchased from Dollarama (Montreal, Quebec, Canada). A PDMS pre-solution was prepared by mixing the pre-polymer solution and the crosslinking agent solution at a 10:1 ratio from SYLGARD™ 184 Silicone Elastomer Kit. The beads were packed in a Petri dish. Then, the pre-solution was poured into the Petri dish, and the beads were immersed completely. The Petri dish was put into an oven heated at 65 °C overnight. The cured PDMS mold was removed from the Petri dish, and a sharp razor was used to cut from the side of the PDMS until the beads were exposed. The beads were popped out from PDMS and left empty pores inside.

Wax Template Bead Fabrication: Irregular paraffin beads, purchased from Sigma Aldrich, were put into a glass beaker. The beaker with wax was heated until the wax was melted. Then, the PDMS mold was immersed into the melted wax. A pair of tongs was used to squeeze the mold and remove the air from the pores in order to infill the pores with wax. After the air was removed, we clamped the PMDS and transferred the mold quickly into an ice water bath to solidify the wax inside. After that, gently, we popped the wax beads out and stored them in a Petri dish for later experiments.

Porous Hydrogel Fabrication: Free radical polymerization of NIPAm was used to synthesize the hydrogels (Figure 4.1, step 1–3). The formula of the polymer solution was optimized to maintain a workable durability of the hydrogel. An illustration of the procedure is shown in Figure 4.1. At room temperature, 8.48 g NIPAm monomer were dissolved in 50 mL of DI water. Then, 58 mg of BIS cross linker were added to the monomer solution. After the solution was homogenized, 135 mg KPS were added as an initiator, and the solution was bubbled under nitrogen for 15 min. Before pouring into the mold, 200 µL TEMED were added as an accelerator to speed up the

polymerization. To introduce a porous structure inside the hydrogels, a silicone mold (32mm x 32mm x 32mm) packed with wax template beads was used for polymerization for 24 h. The polymerized hydrogel was removed from the mold and soaked in DI water at room temperature for a minimum of 48 h. During this process, the wax template beads were removed manually by gently jiggling the hydrogel under water. The unreacted monomer also was dissolved into the surrounding DI water. Samples used for swelling and deswelling characterization did not have their dimensions altered after polymerization.

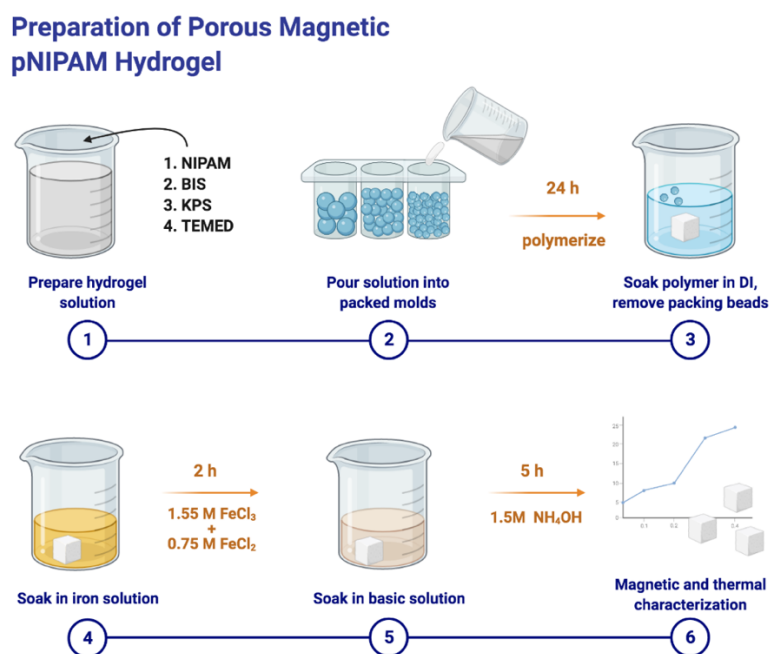


Figure 4.1. Preparation of porous magnetic pNIPAm hydrogel samples at room temperature. Figure created on BioRender.com.

Magnetite Incorporation: PNIPAm hydrogels were magnetized via a co-precipitation method at room temperature (Figure 4.1, step 4–5). First, the hydrated gel was soaked in a solution with 1.55 M Fe^{3+} and 0.75 M Fe^{2+} for 2 h. The solution was prepared using FeCl_3 and $\text{FeCl}_2 \cdot 4\text{H}_2\text{O}$. Then, the hydrogel was soaked in a 1.5 M NH_4OH solution for 5 h. Magnetized samples were washed and stored in DI water at room temperature. The soaking times and concentrations of this method were optimized previously by the Serpe group. The amount of magnetite co-polymerized on the hydrogel was determined gravimetrically as a percentage of the dry polymer weight.

Unmagnetized samples were dried at room temperature for 24 h, then dried at 70 °C in an oven to achieve a constant mass. The dry mass was measured using an analytical balance. After rehydrating at room temperature for 24 h, the samples were incorporated with magnetite and dried again for 24 h at room temperature, then 70 °C in an oven to achieve a constant mass. The magnetized dry mass was determined using an analytical balance. The magnetite incorporation percentage was determined using the formula:

$$\% M = (W_{\text{mag}} - W_{\text{dry}})/W_{\text{dry}} \quad (1)$$

where W_{dry} and W_{mag} are the weights of the dried unmagnetized gels and dried magnetized gels, respectively.

Swelling and Deswelling Rate Characterization: Fully hydrated hydrogel samples equilibrated at room temperature were submerged in a 40 °C DI water bath. The dimensions of the shrinking hydrogel over time were recorded using a camera. Then, the shrunken sample was transferred from the 40 °C water bath into a 22 °C water bath, and the dimensions of the swelling hydrogel over time were recorded using a camera. The experiment was done in triplicate for each pore size hydrogel.

LCST Determination: Magnetized and non-magnetized non-porous hydrogel samples were equilibrated at 25 °C for 30 min, and the dimensions of the hydrogel were recorded using a camera. The temperature was ramped from 25 °C to 40 °C, with the dimensions collected using a camera with 2 °C increments in between.

Equilibrium Swelling Ratio: Hydrogel samples were dried at room temperature for 24 h, then at 70 °C in an oven for 2 h and weighed on an analytical balance. The samples were equilibrated with DI water for a minimum of 24 h until fully hydrated. Excess water was removed gently from the gel with a wet filter paper, then the hydrated gel was weighed. The equilibrium swelling ratio (Q) was determined using the formula:

$$Q = (W_{\text{hyd}} - W_{\text{dry}})/W_{\text{dry}} \quad (2)$$

where W_{dry} and W_{hyd} are the weights of the dried gels and the fully hydrated gels, respectively.

Alternating Magnetic Field Testing: The alternating magnetic field (AMF) source used throughout this work is powered by an induction heater with a 24 V DC/15 A output and a frequency of approximately 120–150 kHz (Figure 4.2). The power source is connected to a copper coil, 5.19 cm long, with seven turns, and is internally

cooled with running tap water. An IR camera (Imaging IR Thermometer, TG165, FLIR, Wilsonville, Oregon, United States) was used to visualize the hydrogel heating process induced by the AMF.



Figure 4.2. Alternating magnetic field apparatus. Output of inductive heater is 24 VDC/15 A, and ~ 120 –150 kHz. Copper coil has 7 turns, length of 5.19 cm, and is internally cooled with cold water.

Cargo Capture Experiments: A porous magnetized hydrogel was placed in a 150 mL beaker of DI water with some floating paraffin wax template beads representing the cargos. A piece of magnet was used to direct the magnetized hydrogel towards the cargo, and the AMF was initiated to heat the gel above the LCST.

4.3 Results and Discussion

For this study, we aim to demonstrate a cargo capture and transport system using shape morphing actuators. The final design we converged on is shown in Figure 4.3.

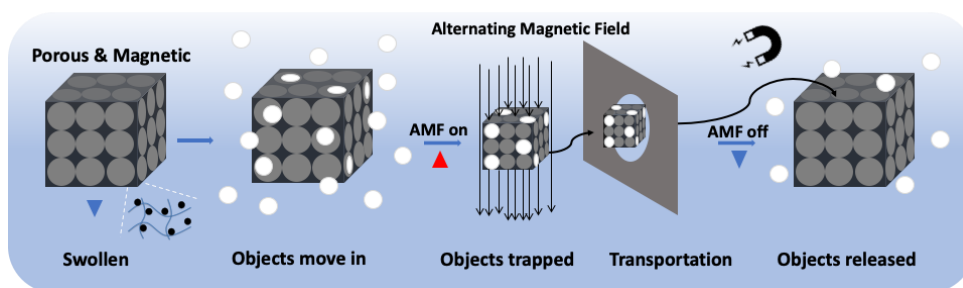


Figure 4.3. Illustration of temperature- and magnetic field-responsive hydrogel on an “Ant man mission”. A porous hydrogel with magnetic bead embedded; objects move into the vacant pores of the swollen hydrogel; with AMF on, the hydrogel is heated and traps the objects inside; the external magnetic field guides the hydrogel with cargo through space; the AMF is switched off, the hydrogel cools and swells releasing the cargo in the pores.

4.3.1 Wax Template Beads

A significant amount of experiments focused on how to create wax template beads easily (Figure 4.4). Paraffin wax was selected as an alternative material for the glass and plastic beads used initially, which were too heavy and ripped the hydrogel. Paraffin wax is light, buoyant, highly moldable, and inexpensive, making it an ideal material for wax template beads. However, spherical paraffin wax beads with certain dimensions were not available. As such, a method was developed to make them in the laboratory.

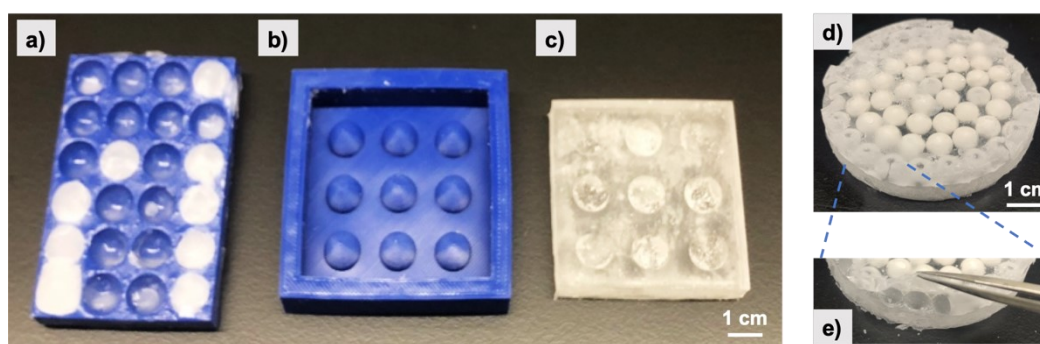


Figure 4.4. Pictures of the different molds. a) 3D printed PLA hemisphere mold with some hemispherical wax beads; b) 3D printed PLA negative hemisphere mold; c) PDMS hemisphere mold made from negative PLA mold; d) PDMS mold made from bead templating; e) the pores left inside.

The first attempt was to use two hemisphere plastic molds created with a 3D printer (Prusa Research Company, Prague, Czech Republic). The molds were filled with hot wax and pressed against each other to create spheres. However, the wax beads were hard to remove from the mold and were broken easily. A second approach was to 3D print negative hemisphere molds and fill them with PDMS (1:10 Sylgard 184 curing agent: Sylgard 184 base) to create flexible molds where the wax beads would be removed easily. This method worked fine for the beads of larger diameters, but at smaller diameters, the hemisphere molds had the printed texture from the 3D printing process that makes the beads irregular.

The approach that we finally adopted was to pack a petri dish with the aforementioned glass or plastic beads. Then, PDMS mixture was poured into the dish to cover the beads fully. Once the PDMS was cured, the beads were removed from the PDMS mold leaving vacant spherical pores. The PDMS mold can be submerged in

molten wax to fill the pores and then cooled to solidify the wax beads inside. The wax beads were taken out from the PDMS mold for later characterization and usage.

4.3.1.1 Dimension and Uniformity

Different sizes of wax beads were fabricated and characterized. As shown in Figure 4.5, different diameters of wax beads are fairly uniform. In fact, uniformity is not extremely crucial for the application here, as long as the pores in the hydrogels made from the templates are similar and adjustable.

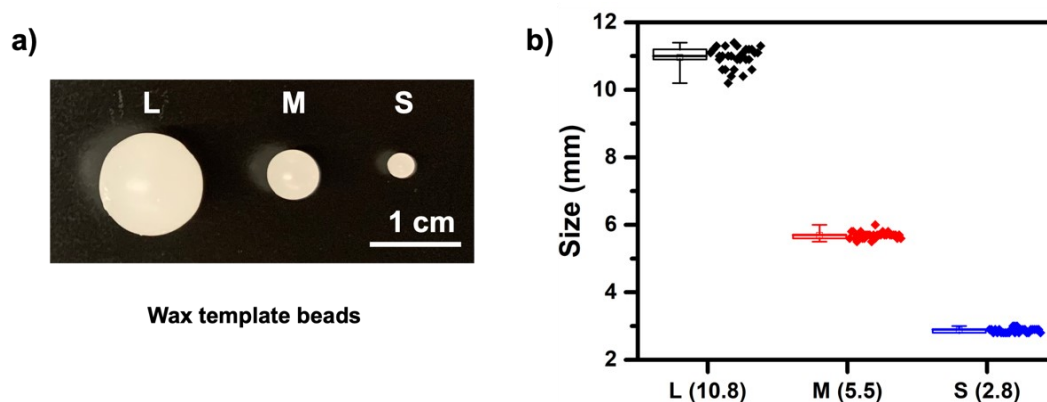


Figure 4.5. Wax template beads with three different sizes. a) A picture of the wax beads on a bench; b) a box plot of the wax template bead size distribution with both boxplot (left) and real data (right).

4.3.1.2 Packing Density

Due to the known dimension and uniformity of the wax template beads, the packing for different diameters can be analyzed. Since the pores are resulting from the wax beads, the surface area of the hydrogels can be analyzed. For the hydrogel cubes with the same dimension but different sizes of beads incorporated, the surface area per unit volume of hydrogel was calculated by the following equation:

$$A\% = NA_w/V \quad (3)$$

where N is the total wax beads packed inside, A_w is the surface area for the wax bead, and V is the volume of the cubic hydrogel, which are the same for all the three samples with different wax bead sizes.

As shown in Figure 4.6, for hydrogels with the same dimension, the smaller the wax template beads, the more surface areas there are inside the hydrogel.

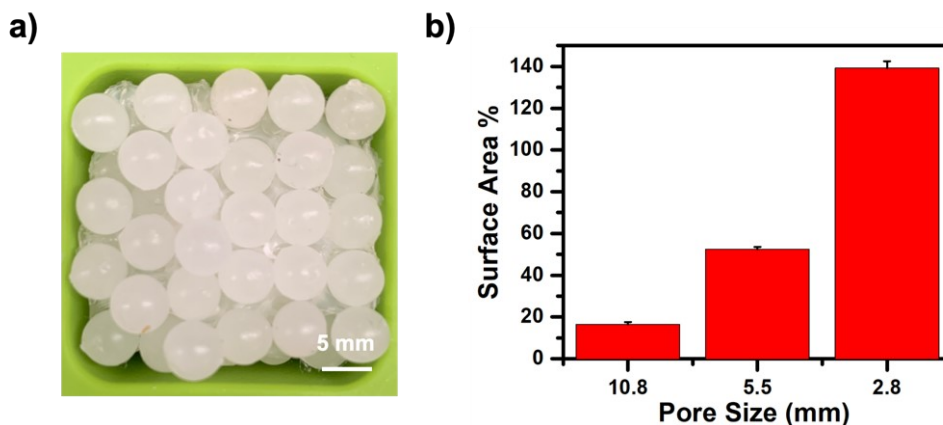


Figure 4.6. A bar graph showing the different surface area for hydrogels with different sizes of wax template beads. With smaller wax beads, the hydrogels have larger surface area per unit volume of hydrogel.

4.3.2 Porous pNIPAm Hydrogels

Soft pNIPAm actuators were synthesized at room temperature through facile free radical polymerization. Many methods have been described in the literature to synthesize high surface area, fast responding porous hydrogels. Typically, these methods are laborious, and the pores generated are small and not designed for the purpose of capturing and releasing cargo. The paraffin wax templating method we developed to create porous pNIPAm hydrogels has the advantage of being simple, inexpensive, and easily tailorable to create different pore sizes corresponding to desired response rates or cargo sizes.

4.3.2.1 Pore Size and Thermal Response Rate

Changes in the pore size in a hydrogel can affect its thermal response rate. The shrinking rate was investigated by submerging the swollen hydrogels equilibrated in 22 °C DI water into a 40 °C water bath and capturing the volume change over time with a camera. Similarly, the swelling rate was investigated by submerging shrunken hydrogels equilibrated in 40 °C DI water into a 22 °C water bath and capturing the volume change over time. The analysis was done by dimensions rather than by weight because the highly porous hydrogels were difficult to move without any breakage. Figure 4.7 shows both the shrinking and swelling response rates for various pore sizes. As shown in the graph, the porous hydrogel actuators shrink and swell faster than their

non-porous counterparts. Furthermore, the speed of response increases with decreasing pore size. This can be attributed to the high surface area of samples with small pore sizes, resulting in faster diffusion of water in and out of the gel, thus a faster thermal response rate.

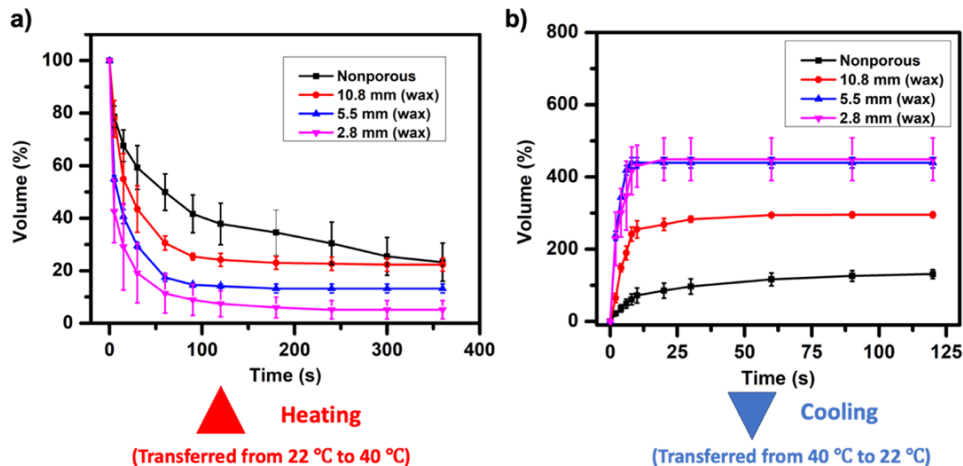


Figure 4.7. Hydrogel volume change in response to temperature change over time. a) Heating process: hydrogel is transferred from 22 °C DI water into a 40 °C water bath; b) cooling process: hydrogel is transferred from 40 °C DI water into a 22 °C water bath.

Moreover, changes in volume between the hydrated and shrunken state also increase with decreasing pore sizes. As investigated previously, samples with a smaller pore size have a higher total surface area, which could retain more water at the swollen state. This is discussed further in 4.3.2.2. Therefore, when the hydrogel was heated above the LCST, more water was expelled from the hydrogel network.

Among all samples, the swelling rates were slower than the deswelling rate, with deswelling occurring within 5 min and swelling taking up to 48 h. This is a typical feature of pNIPAm swelling kinetics and has been described well in the literature. Briefly, for the deswelling process, the polymer chains collapse, form hydrophobic interactions, and drive the water out of the network. However, once the hydrogel shrank, there are fewer void channels for water to move freely, resulting in slow diffusion into the center of the hydrogel. The other reason is that the hydrophobic interactions among the collapsed hydrogel make it hard for water molecules to break, form clathrates, and swell the hydrogel. As a result, the swelling rates are slower than the deswelling rates.

4.3.2.2 Equilibrium Swelling Ratio

Equilibrium swelling ratios (Q) for the hydrogel samples were assessed at 22 °C, and the results are shown in Figure 4.8(a). For the unmagnetized, non-porous hydrogel, the equilibrium swelling ratio was about 8.9. The swelling ratio increases as the pore size decreases, indicating that higher surface area samples are able to hold more water. For more porous hydrogels with larger surface area, they tend to swell more near the surface, as the polymer chains are less entangled on the surface than in the center. As shown in Figure 4.8(b), when hydrogel was equilibrated below LCST, the surfaces of the hydrogel swelled more than the center areas, showing stretched and more transparent surfaces around the hydrogel.

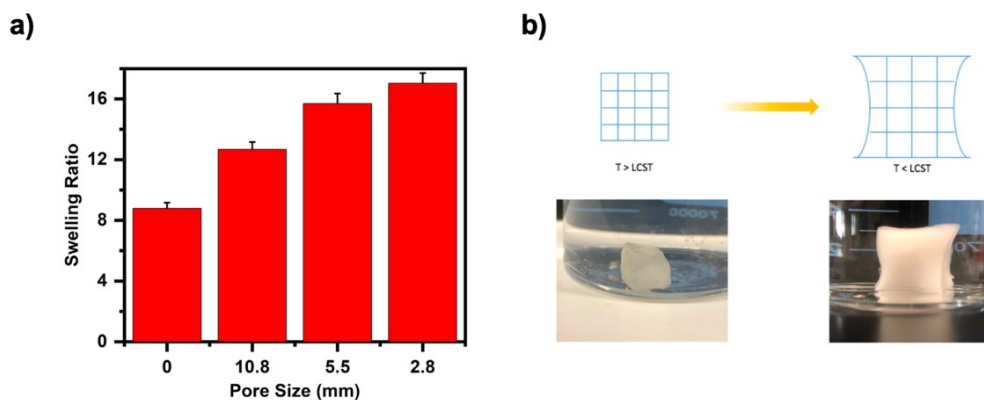


Figure 4.8. Equilibrium swelling ratios for hydrogels with different porosities. a) A graph showing the different swelling ratios for different porosities; b) top: illustration showing the hydrogel network swells more around the surfaces; bottom: pictures showing the hydrogel morphologies.

4.3.3 Magnetized Hydrogels

4.3.3.1 Magnetite Deposition

PNIPAm hydrogels were magnetized successfully via a co-precipitation method optimized previously by the Serpe group, as shown in Figure 4.9. The mass of magnetite deposited into the gel was determined gravimetrically by weighing the hydrogel before and after the deposition process. About 27% of magnetite in relative to the original mass of the unmagnetized hydrogel was incorporated according to the calculation.

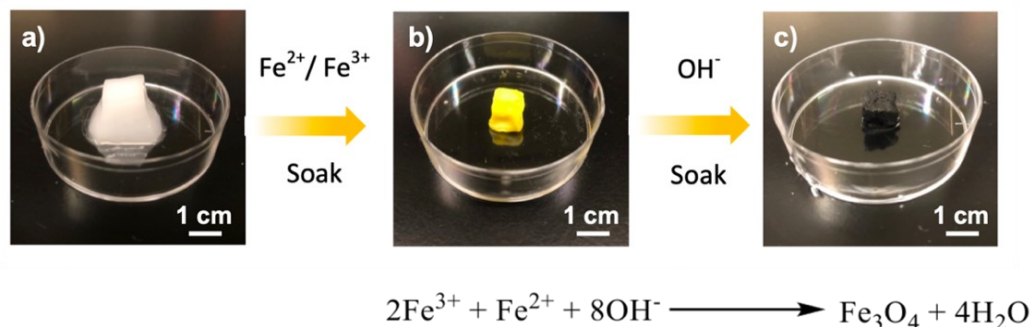


Figure 4.9. The magnetization process. a) The picture of the pNIPAm hydrogel; b) the picture of the pNIPAm hydrogel saturated with iron solution; c) the picture of the magnetized hydrogel after the co-precipitation synthesis.

4.3.3.2 Impact of the Magnetite on the LCST

The dimensions of the magnetized and unmagnetized non-porous hydrogels were recorded with a camera at temperatures ranging from 25 °C to 40 °C to investigate the impact of the magnetite on the LCST. As shown in Figure 4.10, both of the magnetized and unmagnetized hydrogels showed a sharp phase transition from the solvated, swollen state to the shrunken, dehydrated state at around 30 °C, which falls into the typical range for pNIPAm hydrogels. This suggested that the presence of the magnetite did not impact the LCST of the pNIPAm hydrogels.

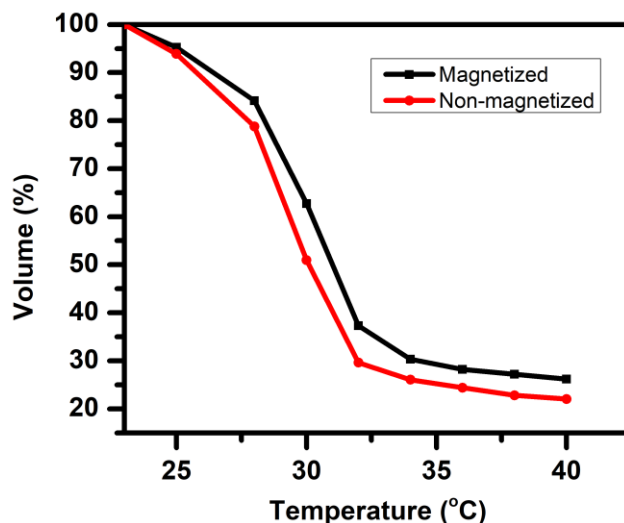


Figure 4.10. Volume changes of both the magnetized (black) and non-magnetized (red) pNIPAm hydrogels when the temperature increased from 25 °C to 40 °C. Note: the point on the curve where the slope changes sharply often is referred to as the phase transition; the corresponding temperature is referred to as the LCST.

4.3.3.3 Magneto-Thermo Effect

An inductive heater connected to a copper working coil was used to produce an alternating magnetic. Ampere's Law for a solenoid can be used, assuming ideal conditions, to calculate the magnetic field in the center of the coil:

$$B = \mu_0 IN/l \quad (4)$$

where B is the magnetic field strength in the center of the coil, μ_0 is the permeability of free space, I is the current, N is the number of turns, and l is the length of the coil. The magnetic field strength was about 2.5 mT in the center of the coil after the measurement and calculation. Eddy currents were not considered, given the small magnetic field of the incorporated magnetite.

Magneto-thermo effect of the magnetic particles that were collected from the co-precipitation process were investigated first. As shown in Figure 4.11a, the particles sat at the bottom of the centrifugation tube. After the AMF was started for 20 s, the bottom of the tube started to heat up giving a bright yellowish orange color, as shown in the IR camera image (Figure 4.11b). This indicated that superparamagnetic nanoparticles were synthesized and were able to exhibit the magneto-thermo effect.

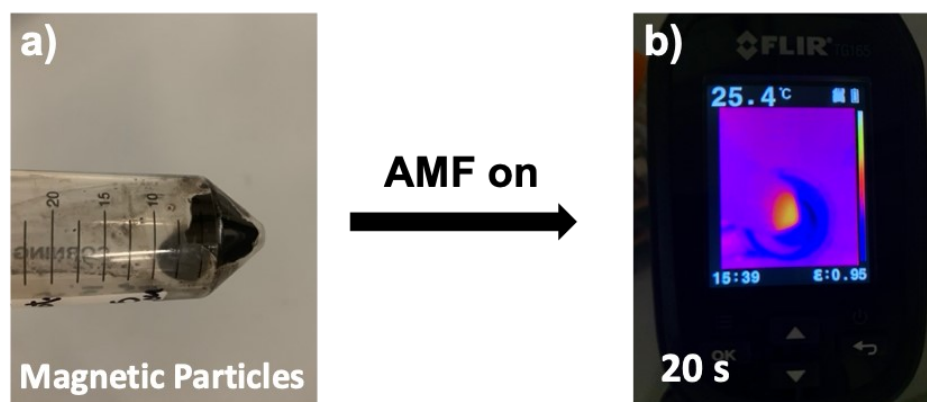


Figure 4.11. Magneto-thermo effect of the magnetic particles. a) Magnetic particles collected at the bottom of a centrifuge tube; b) a picture of an IR camera image of the magnetic particles in a centrifuge tube. The red part at the center of the screen is where the magnetic particles sit.

To demonstrate the magneto-thermo effect of magnetic particles in the hydrogel, the magnetized hydrogel was placed inside the coil to induce hyperthermia. As shown in Figure 4.12, the gels with a black color in the IR image heated slowly and turned into a brighter yellow color. However, the hydrogel produced from this method

was unable to heat to above the LCST within a reasonable time frame when it was placed inside a beaker of water at room temperature. On the contrary, the hydrogel even swelled a bit (Figure 4.13).

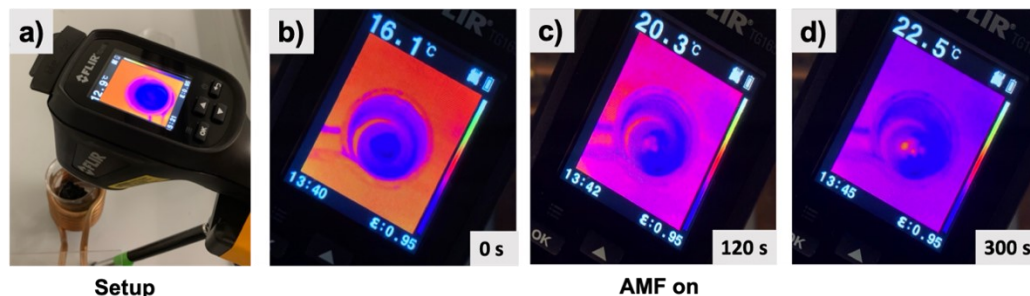


Figure 4.12. Magneto-thermo effect of the magnetic hydrogel. a) The setup for monitoring the temperature using an IR camera; b) a picture of an IR camera image of the magnetic hydrogel at 0 s; c) a picture of an IR camera image of the magnetic hydrogel at 120 s; d) a picture of an IR camera image of the magnetic hydrogel at 300 s.

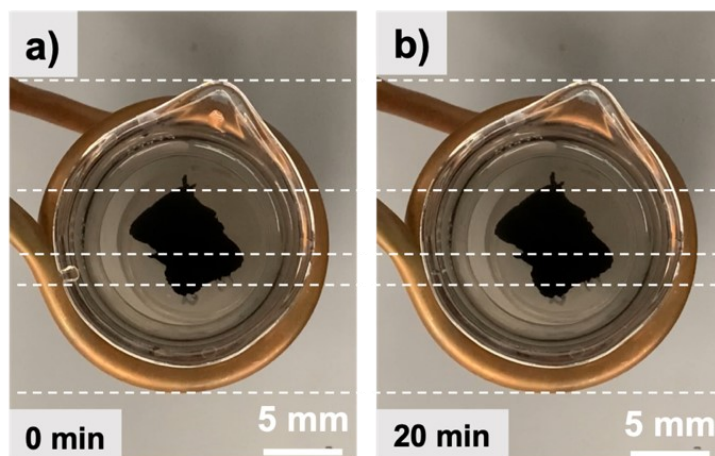


Figure 4.13. Magneto-thermo effect of the magnetic hydrogel in a water bath at room temperature. a) Magnetic hydrogel before AMF was turned on; b) magnetic hydrogel after AMF was turned on for 20 min. The dotted lines are the reference lines for better size inspection.

The possible explanation is that the hydrogel still was swelling in the water after the magnetic particle introduction. Meanwhile, the surrounding room temperature constantly took away the heat produced. Moreover, the magneto-thermo effect might be too small due to either not enough magnetic particles or the AMF set up not powerful enough, which could lead to slow hydrogel internal heating, thus little shrinkage and failure to overcome the expansion and heat loss to the surrounding water. One possible solution is to equilibrate the hydrogel completely before magneto-thermo effect

demonstration. The second solution is to repeat the coprecipitation process a few times to introduce more magnetic particles. Another possible approach is to try using a more powerful output source to produce stronger AMF, thus heating the hydrogel within a short period of time.

4.3.4 Cargo Transportation

Before the AMF heating efficiency problems are addressed, due to the low efficiency of the AMF heating for the current hydrogel, the cargo transportation demonstration was done in a water bath and using an external heating method just as a proof of concept. The success of the transportation demonstration could validate the feasibility of this actuating system and provide incentives for further developments and improvements.

4.3.4.1 Cargo Capture Demonstration

Cargo capture was demonstrated first using the simple water heating method. The porous hydrogel was placed in a beaker full of water. Some wax beads were floating on the surface as cargos. The hydrogel was guided by a piece of magnet to the surface. The wax beads moved to the pores of the hydrogel during movement and agitation. Then, the water was heated above the LCST to shrink and capture the wax beads inside. As shown in figure 4.14(a-c), the wax beads were inside the pores and stuck after hydrogel shrinkage. Using the magnet to agitate the hydrogel, the wax beads still were stuck inside strongly. The hydrogel with cargo could be guided and moved freely in the water media.

4.3.4.2 Cargo Release Demonstration

As shown in Figure 4.14(d), the cargos were released slowly due to the expansion of the pores of the hydrogel when the hydrogel cooled below the LCST. When the water cooled, the wax beads were loosened and no longer stuck inside the pores. Due to their buoyancy, the wax beads were released slowly from the hydrogels and floated to the surface of the water.

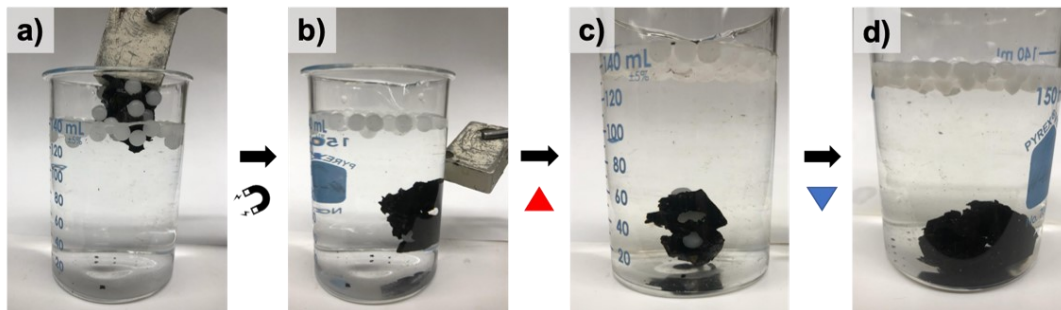


Figure 4.14. Cargo capture and release demonstration. a) A piece of magnet was used to direct the movement of the porous hydrogel towards the surface of the water with wax beads floating; b) the wax beads moved into the pores of the hydrogel; c) the wax bead were trapped inside of the hydrogel when the water was heated above the LCST; d) The water was cooled to room temperature; wax beads were released due to the expansion of the pores of the hydrogel.

4.4 Conclusions

In this chapter, we explored the possibility of using porous temperature- and magnetic field-responsive pNIPAm hydrogel to realize cargo transportation. The macroscopic pores introduced not only increased the actuation speed but also served as vacancies for cargo capture and release. We adopted an innovative wax bead templating method for porous hydrogel synthesis, which was efficient and controllable. The effects of different pore sizes on the actuation response speed were investigated. Using the co-precipitation method, we incorporated magnetic particles into the hydrogel. Also, we demonstrated the magneto-thermo effect of both the magnetic particles alone and the magnetic particles inside the hydrogel. The cargo capture and release also were demonstrated in a simple water bath. However, the magneto-thermo effect of the magnetic hydrogel in a room temperature water bath was not significant enough to actuate the hydrogel to the extent that cargo capture could be demonstrated. A few possibilities were discussed, and future solutions were provided.

Meanwhile, the primary disadvantages of the method are the time spent to create the beads from PDMS molds, the time to remove the beads manually from the hydrated gel, and the lower size limit of the wax beads. However, if a supply of premade spherical wax beads were available from a supplier and did not need to be reused, the wax beads could be melted out of the samples at a temperature higher than the melting temperature of the wax beads with no damage to the hydrogels.

There are many promising applications, provided that the aforementioned issues are addressed. The remote control and multi-responsiveness capability of the actuator could inspire more research in many areas, for example, algae removal tasks, marine investigations, and miniaturized robot operations.

Chapter 5

Conclusions and Future Outlook

This thesis was focused on developing biomimetic actuators. Inspired by mother nature, biomimetic actuators have the advantage of realizing functions or behaviors without the need for an in-depth understanding of the mechanisms. With limited resources and instrumentations, research on biomimetic actuators is more accessible and easier to realize functionalities. We developed primarily three bio-inspired actuators, including an octopus-inspired swimming actuator, a shape morphing cargo-transporting actuator, and a *Mimosa Pudica* plant-inspired touch-responsive actuator.

Firstly, we developed a swimming device inspired by the swimming motion of octopuses. By observing closely how an octopus swims, we see that it curls its tentacles and straightens them to propel the water. As a result, they can swim in the opposite direction due to the reaction force. To realize similar motions, two materials were investigated. The first is a bistable metal strip, which can be found in kids' toys called "slap bracelets". The strip can be straightened and triggered to snap, exerting a powerful snapping recoil force. The easy and robust transformation between two states provides the tentacle propelling form and enough energy to move forward. To control the snapping movements, we introduced the second material, Nitinol, a shape memory alloy. We set a permanent spring-like shape for the Nitinol wire at a high temperature. After it is attached to the bistable metal strip, the Nitinol spring can provide the trigger and reset force for the metal strip by heating the Nitinol through applied electricity. When the metal strip is reset all the way to the straight position, the next trigger from the Nitinol can cause a quick snapping motion, just like an octopus escaping the predators. However, if the Nitinol triggers only half-way, the metal strip will coil back automatically, displaying a slow swimming motion like an octopus swimming care-free.

We demonstrated that the actuator developed here also can swim in multiple directions, all controlled by a wireless module. Furthermore, an onboard sensor can be incorporated for potential environmental monitoring applications. The fact that the

device developed here has no mechanical parts, makes this an interesting potential alternative to more expensive and energy consuming boats.

The device was fabricated using materials available in the laboratory, which might not be the best choices. Besides, a lot of the assembly and connection designs were not optimized. The improvement of the swimming device should be focused on finding better materials and coming up with new designs to make the device more robust and easier to assemble or alter.

A lot of new opportunities are possible with the device. For example, we can add a buoyancy control to make the device into a submarine that is sturdy in various weather conditions. Moreover, we can add solar cell panels and GPS so that the device can be charged to work continuously, and be locatable if lost in the wild. We can even imagine a swarm of these devices working together by communicating with each other to accomplish more complex tasks, such as on-site sensing, monitoring, and surveillance.

Secondly, we presented a touch-responsive actuator mimicking the shy plant *Mimosa Pudica*. This shy plant can close its leaves if touched or agitated to protect itself. We demonstrated an actuator that can actuate by a fingertip touch. How a fingertip touch can exert stimulus is the biggest challenge. The first thing that came to our mind is the force. As a result, we sought an indirect trigger mechanism, using a fingertip touch to induce a chemical stimulus. The idea is to incorporate chemicals embedded in the device, which upon touch, causes chemicals to be released to actuate the device to close. The mechanism we arrived at was using acrylate-Fe³⁺ coordination as crosslinking points that can be destroyed by an HCl solution. We synthesized a P(AAm-co-AAc) hydrogel, pre-stretched it, and fixed it with FeCl₃ solution. The elastic energy stored can be released when the hydrogel reacts with HCl solution. The next critical design was to achieve an HCl solution release upon a fingertip touch. We managed to realize this mechanism by fabricating breakable wax capsules with an HCl solution encapsulation.

We demonstrated successfully the *Mimosa Pudica* plant inspired actuator. After cutting out pant-like leaves from plastic sheets, we fixed a piece of hydrogel onto the leaves with a wax capsule embedded. When we pressed the gel, the wax capsule broke

and released the HCl that reacted with the gel by destroying the crosslinking points. The gel softened, shortened, and brought the leaves closer to each other. The whole process resembled the behavior of a shy plant being touched. The gel can be pre-stretched and fixed; a wax capsule can be embedded again; the actuation process can be repeated.

However, the problem with this biomimetic actuator is that the “touch” here is not a touch, but a “press” instead. The real shy plant is much more sensitive compared to our actuator. The future avenue of this research should focus on achieving much a smaller force for actuation. One possible approach is to fabricate wax capsules with thinner shells. However, the problem is that it will be a much more delicate system that does not withstand handling. Hopefully, some new fabrication technology and new materials for the shell can emerge in the near future. The other approaches could be new mechanisms, such as a stimulus from the fingertip, for example, the fingertip temperature. Maybe the fingertip touch can cause some changes, like a phase separation or precipitation. However, this is the difficulty for touch-responsive actuators. Hopefully, in the near future, some mechanism similar to the real shy plant actuation that can be utilized.

The advancement of this area should integrate with feedback loops, biological systems, or some artificial intelligence. For example, the touch can set off the alarms to indicate danger, or the touch actuation can send signals to the nervous systems and actions can be taken or suggested.

Lastly, we developed a cargo transporting actuator. To transport cargos, we need to realize capturing, moving, and releasing sequentially. In order to achieve this, we proposed to synthesize porous PNIPAm hydrogels with magnetic particles incorporated. The pores inside the hydrogel can trap floating cargos. Due to the magneto-thermo effect of the magnetic particles, the hydrogel system can be heated by applying an alternating magnetic field externally. The heat produced by the magnetic particles can be utilized to heat the temperature-responsive PNIPAm hydrogels. As a result, the hydrogels shrink in size and capture the cargos tightly inside. Since the hydrogel contains a lot of magnetic particles, it can be guided by an external magnetic field to travel around. When the actuator arrives at the destination, the alternating

magnetic field is turned off, and the hydrogel cools off and swells; the cargos trapped inside can be released by jiggling the hydrogel gently with a magnetic field.

We synthesized the porous hydrogels successfully using a wax bead templating method. By varying the wax bead sizes, we afforded hydrogels with different pore sizes. We demonstrated that hydrogels with smaller pore sizes respond faster upon temperature change. Magnetic particles were introduced, using a facile in-situ coprecipitation method. The magnetic hydrogels showed successful magneto-thermo effects characterized by an IR camera in an alternating magnetic field produced by an induction heater.

We also showcased cargo capturing, moving, and releasing demonstrations using a water bath for temperature changes and floating wax beads as cargos. However, we did not observe an obvious size change when using an induction heater on the porous hydrogel immersed in water. We speculated that the reason for this behavior is that the heat produced dissipated too fast to the surrounding water so that the heat could not be accumulated to heat up the hydrogel up to LCST. We could increase the output power of the induction heater or increase the density of the magnetic particles incorporated. Moreover, some different magnetic particle incorporation methods should be investigated so that the magneto-thermo effect can be more pronounced.

Our future research should focus on the remote power transmission technology so that the alternating magnetic field can be applied remotely and more efficiently. Moreover, different designs and architectures of the actuators should be investigated for various application scenarios. Hopefully, these cargo transporting actuators can be used for water cleaning, dissemination, and sample collection.

Biomimetic actuator research is a big topic. Due to the inexhaustible resources from mother nature, there are a lot of opportunities for future developments in this area. In addition, with the fast advancement in different areas, such as 3D printing technology, gene technology, material science, artificial intelligence, and brain-computer interface, researchers from all backgrounds should all come together to cooperate. We should always keep our curiosity, creativity, and perseverance.

References

1. Reed, P. A., A paradigm shift: Biomimicry. *Technology and Engineering Teacher* **2003**, 63 (4), 23.
2. White, M., *Leonardo: the first scientist*. Macmillan: 2001.
3. Postiglione, R. A., Velcro & Seed Dispersal. *The American Biology Teacher* **1993**, 55 (1), 44-45.
4. Robotics Today BR23C Bee. <https://www.roboticstoday.com/robots/br23c-bee> (accessed Oct 11, 2022).
5. Rosenhouse, G., Bio-mimics for Sound and Vibration Technologies. *WIT Transactions on Ecology and the Environment* **2004**, 73.
6. Fish, F. E., Biomimetics and the Application of the Leading-edge Tubercles of the Humpback Whale Flipper. In *Flow Control Through Bio-inspired Leading-Edge Tubercles: Morphology, Aerodynamics, Hydrodynamics and Applications*, New, D. T. H.; Ng, B. F., Eds. Springer International Publishing: Cham, 2020; pp 1-39.
7. Xie, Z.; Domel, A. G.; An, N.; Green, C.; Gong, Z.; Wang, T.; Knubben, E. M.; Weaver, J. C.; Bertoldi, K.; Wen, L., Octopus Arm-inspired Tapered Soft Actuators With Suckers for Improved Grasping. *Soft Robotics* **2020**, 7 (5), 639-648.
8. Sfakiotakis, M.; Kazakidi, A.; Tsakiris, D. P., Octopus-inspired Multi-arm Robotic Swimming. *Bioinspiration & Biomimetics* **2015**, 10 (3), 035005.
9. Ahmed, F.; Waqas, M.; Shaikh, B.; Khan, U.; Soomro, A. M.; Kumar, S.; Ashraf, H.; Memon, F. H.; Choi, K. H., Multi-material Bio-inspired Soft Octopus Robot for Underwater Synchronous Swimming. *J. Bionic Eng.* **2022**, 19 (5), 1229-1241.
10. Spinks, G. M., Advanced Actuator Materials Powered by Biomimetic Helical Fiber Topologies. *Adv. Mater.* **2020**, 32 (18), 1904093.
11. Curcio, C. A.; Sloan, K. R.; Kalina, R. E.; Hendrickson, A. E., Human Photoreceptor Topography. *J. Comp. Neurol.* **1990**, 292 (4), 497-523.
12. Naughton, R. Hargrave Aviation and Aeromodelling—Interdependent Evolutions and Histories. <https://www.ctie.monash.edu/hargrave/tihanyi.html> (accessed 10/22).
13. National Aeronautics & Space Administration JAMES WEBB SPACE TELESCOPE GODDARD SPACE FLIGHT CENTER. <https://webb.nasa.gov/content/observatory/ote/mirrors/index.html> (accessed 10/12).
14. Jeong, K.-H.; Kim, J.; Lee, L. P., Biologically Inspired Artificial Compound Eyes. *Science* **2006**, 312 (5773), 557-561.
15. Choi, C.; Seung, H.; Kim, D. H., Bio-inspired Electronic Eyes and Synaptic Photodetectors for Mobile Artificial Vision. *IEEE Journal on Flexible Electronics* **2022**, 1 (2), 76-87.
16. Zhang, Z.; Wang, S.; Liu, C.; Xie, R.; Hu, W.; Zhou, P., All-in-One Two-dimensional Retinomorph Hardware Device for Motion Detection and Recognition. *Nature Nanotechnology* **2022**, 17 (1), 27-32.
17. Lombardi, F.; Podd, F.; Solla, M. From Its Core to the Niche: Insights from GPR Applications *Remote Sensing* [Online], **2022**.
18. Crocco, L.; Ferrara, V. In *A Review on Ground Penetrating Radar Technology for the Detection of Buried or Trapped Victims*, 2014 International Conference on Collaboration Technologies and Systems (CTS), 19-23 May 2014; **2014**; pp 535-540.
19. Leblanc, M.; Favreau, G.; Maley, J.; Nazoumou, Y.; Leduc, C.; Stagnitti, F.; van Oevelen, P. J.; Delclaux, F.; Lemoalle, J., Reconstruction of Megalake Chad Using Shuttle Radar Topographic Mission Data. *Palaeogeogr., Palaeoclimatol., Palaeoecol.* **2006**, 239 (1), 16-27.
20. Koo, V.; Chan, Y. K.; Vetharatnam, G.; Chua, M. Y.; Lim, C. H.; Lim, C. S.; Thum, C.; Lim, T. S.; bin Ahmad, Z.; Mahmood, K. A., A New Unmanned Aerial Vehicle Synthetic Aperture Radar for Environmental Monitoring. *Progress In Electromagnetics Research* **2012**, 122, 245-268.
21. Zhang, X.; Cheng, J.; Wu, L.; Mei, Y.; Jaffrezic-Renault, N.; Guo, Z., An Overview of an Artificial Nose System. *Talanta* **2018**, 184, 93-102.
22. Gu, X.; Sun, Y.; Tu, K.; Pan, L., Evaluation of Lipid Oxidation of Chinese-style Sausage During Processing and Storage Based on Electronic Nose. *Meat Science* **2017**, 133, 1-9.

23. Dacres, H.; Wang, J.; Leitch, V.; Horne, I.; Anderson, A. R.; Trowell, S. C., Greatly Enhanced Detection of a Volatile Ligand at Femtomolar Levels Using Bioluminescence Resonance Energy Transfer (BRET). *Biosensors and Bioelectronics* **2011**, *29* (1), 119-124.
24. Lee, S. H.; Lim, J. H.; Park, J.; Hong, S.; Park, T. H., Bioelectronic Nose Combined With a Microfluidic System for the Detection of Gaseous Trimethylamine. *Biosensors and Bioelectronics* **2015**, *71*, 179-185.
25. Andablo-Reyes, E.; Bryant, M.; Neville, A.; Hyde, P.; Sarkar, R.; Francis, M.; Sarkar, A., 3D Biomimetic Tongue-emulating Surfaces for Tribological Applications. *ACS Applied Materials & Interfaces* **2020**, *12* (44), 49371-49385.
26. Kim, J.; Lee, M.; Shim, H. J.; Ghaffari, R.; Cho, H. R.; Son, D.; Jung, Y. H.; Soh, M.; Choi, C.; Jung, S.; Chu, K.; Jeon, D.; Lee, S.-T.; Kim, J. H.; Choi, S. H.; Hyeon, T.; Kim, D.-H., Stretchable Silicon Nanoribbon Electronics for Skin Prosthesis. *Nature Communications* **2014**, *5* (1), 5747.
27. Kobayashi, Y.; Hamada, H.; Yamaguchi, Y.; Ikezaki, H.; Toko, K., Development of an Artificial Lipid-based Membrane Sensor With High Selectivity and Sensitivity to the Bitterness of Drugs and With High Correlation With Sensory Score. *IEEE Transactions on Electrical and Electronic Engineering* **2009**, *4* (6), 710-719.
28. Kobayashi, Y.; Habara, M.; Ikezaki, H.; Chen, R.; Naito, Y.; Toko, K., Advanced Taste Sensors Based on Artificial Lipids With Global Selectivity to Basic Taste Qualities and High Correlation To Sensory Scores. *Sensors* **2010**, *10* (4).
29. Lipomi, D. J.; Vosgueritchian, M.; Tee, B. C. K.; Hellstrom, S. L.; Lee, J. A.; Fox, C. H.; Bao, Z., Skin-like Pressure and Strain Sensors Based on Transparent Elastic Films of Carbon Nanotubes. *Nature Nanotechnology* **2011**, *6* (12), 788-792.
30. Zhang, Z.; Wang, W.; Jiang, Y.; Wang, Y.-X.; Wu, Y.; Lai, J.-C.; Niu, S.; Xu, C.; Shih, C.-C.; Wang, C.; Yan, H.; Galuska, L.; Prine, N.; Wu, H.-C.; Zhong, D.; Chen, G.; Matsuhisa, N.; Zheng, Y.; Yu, Z.; Wang, Y.; Dauskardt, R.; Gu, X.; Tok, J. B. H.; Bao, Z., High-brightness All-polymer Stretchable Led With Charge-trapping Dilution. *Nature* **2022**, *603* (7902), 624-630.
31. Sun, T.; Wang, G.; Feng, L.; Liu, B.; Ma, Y.; Jiang, L.; Zhu, D., Reversible Switching Between Superhydrophilicity and Superhydrophobicity. *Angew. Chem. Int. Ed.* **2004**, *43* (3), 357-360.
32. Gao, X.; Jiang, L., Water-repellent Legs of Water Striders. *Nature* **2004**, *432* (7013), 36-36.
33. Tang, Z.; Wang, P.; Xu, B.; Meng, L.; Jiang, L.; Liu, H., Bioinspired Robust Water Repellency in High Humidity by Micro-meter-Scaled Conical Fibers: Toward a Long-time Underwater Aerobic Reaction. *Journal of the American Chemical Society* **2022**, *144* (24), 10950-10957.
34. Sun, T.; Feng, L.; Gao, X.; Jiang, L., Bioinspired Surfaces With Special Wettability. *Acc. Chem. Res.* **2005**, *38* (8), 644-652.
35. Autumn, K.; Dittmore, A.; Santos, D.; Spenko, M.; Cutkosky, M., Frictional Adhesion: A New Angle on Gecko Attachment. *J. Exp. Biol.* **2006**, *209* (18), 3569-3579.
36. Kim, S.; Spenko, M.; Trujillo, S.; Heyneman, B.; Santos, D.; Cutkosky, M. R., Smooth Vertical Surface Climbing With Directional Adhesion. *IEEE Transactions on Robotics* **2008**, *24* (1), 65-74.
37. Tramacere, F.; Follador, M.; Pugno, N. M.; Mazzolai, B., Octopus-like Suction Cups: From Natural To Artificial Solutions. *Bioinspiration & Biomimetics* **2015**, *10* (3), 035004.
38. Bechert, D.; Reif, W., On the Drag Reduction of the Shark Skin. In *23rd Aerospace Sciences Meeting*, American Institute of Aeronautics and Astronautics: **1985**.
39. Fiorini, P.; Burdick, J., The Development of Hopping Capabilities for Small Robots. *Autonomous Robots* **2003**, *14* (2), 239-254.
40. Skiles, S. M.; Singh, V.; Krager, J.; Seepersad, C. C.; Wood, K. L.; Jensen, D., Adapted Concept Generation and Computational Techniques for the Application of a Transformer Design Theory. In *International Design Engineering Technical Conferences and Computers and Information in Engineering Conference* **2006**; pp 951-965.
41. Soltanieh, G.; Shariyat, M.; Kabir, M. Z., Influence of the 3D Material Tailoring on Snap-through and Snap-back Post-buckling Behaviors of Steel-wire-Reinforced Hybrid 3D Graded Orthotropic Shallow Cylindrical Panels. *Proceedings of the Institution of Mechanical Engineers, Part C: Journal of Mechanical Engineering Science* **2018**, *233* (2), 685-701.

42. Arrieta, A. F.; Wagg, D. J.; Neild, S. A., Dynamic Snap-through for Morphing of Bi-stable Composite Plates. *J. Intell. Mater. Syst. Struct.* **2011**, 22 (2), 103-112.
43. Chen, Z.; Guo, Q.; Majidi, C.; Chen, W.; Srolovitz, D. J.; Haataja, M. P., Nonlinear Geometric Effects in Mechanical Bistable Morphing Structures. *Phys. Rev. Lett.* **2012**, 109 (11), 114302.
44. Guo, Q.; Zheng, H.; Chen, W.; Chen, Z., Modeling Bistable Behaviors in Morphing Structures Through Finite Element Simulations. *Bio-Medical Materials and Engineering* **2014**, 24, 557-562.
45. Schlecht, M.; Schulte, K., Advanced Calculation of the Room-temperature Shapes of Unsymmetric Laminates. *J. Compos. Mater.* **1999**, 33 (16), 1472-1490.
46. Haldar, A.; Reinoso, J.; Jansen, E.; Rolfes, R., Thermally Induced Multistable Configurations of Variable Stiffness Composite Plates: Semi-analytical and Finite Element Investigation. *Compos. Struct.* **2018**, 183, 161-175.
47. Chen, Z.; Guo, Q.; Majidi, C.; Chen, W.; Srolovitz, D. J.; Haataja, M., Bistable Structures Exhibiting Snap-through Instability: From Slap Bracelets to the Venus Flytrap. In *Summer Bioengineering Conference by American Society of Mechanical Engineers* **2012**; pp 749-750.
48. Kim, S.; Koh, J.; Cho, M.; Cho, K. In *Towards a Bio-mimetic Flytrap Robot Based on a Snap-through Mechanism*, In 2010 3rd IEEE RAS & EMBS International Conference on Biomedical Robotics and Biomechatronics, 26-29 Sept. **2010**; pp 534-539.
49. Arakawa, K.; Giorgio-Serchi, F.; Mochiyama, H., Snap Pump: A Snap-through Mechanism for a Pulsatile Pump. *IEEE Robotics and Automation Letters* **2021**, 6 (2), 803-810.
50. Ilievski, F.; Mazzeo, A. D.; Shepherd, R. F.; Chen, X.; Whitesides, G. M., Soft Robotics for Chemists. *Angew. Chem. Int. Ed.* **2011**, 50 (8), 1890-1895.
51. Maziz, A.; Plesse, C.; Soyer, C.; Cattani, E.; Vidal, F., Top-down Approach for the Direct Synthesis, Patterning, and Operation of Artificial Micromuscles on Flexible Substrates. *ACS Applied Materials & Interfaces* **2016**, 8 (3), 1559-1564.
52. Zakharov, D.; Lebedev, G.; Irzhak, A.; Afonina, V.; Mashirov, A.; Kalashnikov, V.; Koledov, V.; Shelyakov, A.; Podgorny, D.; Tabachkova, N.; Shavrov, V., Submicron-sized Actuators Based on Enhanced Shape Memory Composite Material Fabricated by FIB-CVD. *Smart Mater. Struct.* **2012**, 21 (5), 052001.
53. Buguin, A.; Li, M.-H.; Silberzan, P.; Ladoux, B.; Keller, P., Micro-actuators: When Artificial Muscles Made of Nematic Liquid Crystal Elastomers Meet Soft Lithography. *Journal of the American Chemical Society* **2006**, 128 (4), 1088-1089.
54. Tipler, P. A.; Mosca, G., *Physics for Scientists and Engineers, Volume 1: Mechanics, Oscillations and Waves; Thermodynamics*. Macmillan: 2003.
55. Forbes, E. G., The Origin and Development of the Marine Chronometer. *Annals of Science* **1966**, 22 (1), 1-25.
56. Guillaume, C. E., The Anomaly of the Nickel-steels. *Proceedings of the Physical Society of London (1874-1925)* **1919**, 32 (1), 374.
57. DeVries, W. R.; Lauderbaugh, L. K., A Model for Bending Bimetallic Strip. *Journal of Engineering for Industry* **1984**, 106 (1), 62-69.
58. Stollard, P., *Fire from First Principles: A Design Guide to International Building Fire Safety*. Routledge: **2014**.
59. Kauffman, G. B.; Mayo, I., The story of nitinol: the serendipitous discovery of the memory metal and its applications. *The Chemical Educator* **1997**, 2 (2), 1-21.
60. Duerig, T.; Pelton, A.; Stöckel, D., An overview of nitinol medical applications. *Materials Science and Engineering A* **1999**, 273-275, 149-160.
61. Chaudhari, R.; Vora, J. J.; Parikh, D. M. In *A Review on Applications of Nitinol Shape Memory Alloy*, Recent Advances in Mechanical Infrastructure, Singapore, 2021//; Parwani, A. K.; Ramkumar, P. L.; Abhishek, K.; Yadav, S. K., Eds. Springer Singapore: Singapore, **2021**; pp 123-132.
62. Huang, X.; Ackland, G. J.; Rabe, K. M., Crystal Structures and Shape-memory Behaviour of NiTi. *Nature Materials* **2003**, 2 (5), 307-311.
63. Liu, Y.; Xie, Z., Detwinning in Shape Memory Alloy. *Progress in Smart Materials and Structures* **2007**, 3, 29.
64. Ko, W.-S.; Grabowski, B.; Neugebauer, J., Development and Application of a Ni-Ti Interatomic Potential With High Predictive Accuracy of the Martensitic Phase Transition. *Physical Review B* **2015**, 92 (13), 134107.

65. Baytekin, B.; Cezan, S. D.; Baytekin, H. T.; Grzybowski, B. A., Artificial Heliotropism and Nyctinasty Based on Optomechanical Feedback and No Electronics. *Soft Robotics* **2017**, 5 (1), 93-98.
66. Datla, N. V.; Honarvar, M.; Nguyen, T. M.; Konh, B.; Darvish, K.; Yu, Y.; Dicker, A. P.; Podder, T. K.; Hutapea, P., Towards a Nitinol Actuator for an Active Surgical Needle. **2012**; pp 265-269.
67. Feil, H.; Bae, Y. H.; Feijen, J.; Kim, S. W., Effect of Comonomer Hydrophilicity and Ionization on the Lower Critical Solution Temperature of N-isopropylacrylamide Copolymers. *Macromolecules* **1993**, 26 (10), 2496-2500.
68. Zhang, Q.; Weber, C.; Schubert, U. S.; Hoogenboom, R., Thermoresponsive Polymers With Lower Critical Solution Temperature: From Fundamental Aspects and Measuring Techniques To Recommended Turbidimetry Conditions. *Materials Horizons* **2017**, 4 (2), 109-116.
69. Zhang, Q.; Zhang, Y.; Wan, Y.; Carvalho, W.; Hu, L.; Serpe, M. J., Stimuli-responsive Polymers for Sensing and Reacting to Environmental Conditions. *Progress in Polymer Science* **2021**, 116, 101386.
70. Li, X.; Cai, X.; Gao, Y.; Serpe, M. J., Reversible Bidirectional Bending of Hydrogel-based Bilayer Actuators. *Journal of Materials Chemistry B* **2017**, 5 (15), 2804-2812.
71. Na, J.-H.; Evans, A. A.; Bae, J.; Chiappelli, M. C.; Santangelo, C. D.; Lang, R. J.; Hull, T. C.; Hayward, R. C., Programming Reversibly Self-folding Origami With Micropatterned Photo-crosslinkable Polymer Trilayers. *Advanced Materials* **2015**, 27 (1), 79-85.
72. Breger, J. C.; Yoon, C.; Xiao, R.; Kwag, H. R.; Wang, M. O.; Fisher, J. P.; Nguyen, T. D.; Gracias, D. H., Self-folding Thermo-magnetically Responsive Soft Microgrippers. *ACS Applied Materials & Interfaces* **2015**, 7 (5), 3398-3405.
73. Hu, X.; Zhang, D.; Sheiko, S. S., Cooling-triggered Shapeshifting Hydrogels With Multi-shape Memory Performance. *Advanced Materials* **2018**, 30 (26), 1707461.
74. Jiang, S.; Liu, F.; Lerch, A.; Ionov, L.; Agarwal, S., Unusual and Superfast Temperature-triggered Actuators. *Advanced Materials* **2015**, 27 (33), 4865-4870.
75. Yao, S.; Cui, J.; Cui, Z.; Zhu, Y., Soft Electrothermal Actuators Using Silver Nanowire Heaters. *Nanoscale* **2017**, 9 (11), 3797-3805.
76. Hu, Y.; Liu, J.; Chang, L.; Yang, L.; Xu, A.; Qi, K.; Lu, P.; Wu, G.; Chen, W.; Wu, Y., Electrically and Sunlight-driven Actuator With Versatile Biomimetic Motions Based on Rolled Carbon Nanotube Bilayer Composite. *Advanced Functional Materials* **2017**, 27 (44), 1704388.
77. Qiu, L.; Liu, D.; Wang, Y.; Cheng, C.; Zhou, K.; Ding, J.; Truong, V.-T.; Li, D., Mechanically Robust, Electrically Conductive and Stimuli-responsive Binary Network Hydrogels Enabled by Superelastic Graphene Aerogels. *Advanced Materials* **2014**, 26 (20), 3333-3337.
78. Clark, E.; Lipson, J., LCST and UCST Behavior in Polymer Solutions and Blends. *Polymer* **2012**, 53 (2), 536-545.
79. Seuring, J.; Agarwal, S., Polymers With Upper Critical Solution Temperature in Aqueous Solution. *Macromol. Rapid Commun.* **2012**, 33 (22), 1898-1920.
80. Zheng, J.; Xiao, P.; Le, X.; Lu, W.; Théato, P.; Ma, C.; Du, B.; Zhang, J.; Huang, Y.; Chen, T., Mimosa Inspired Bilayer Hydrogel Actuator Functioning in Multi-environments. *Journal of Materials Chemistry C* **2018**, 6 (6), 1320-1327.
81. Wang, E.; Desai, M. S.; Lee, S.-W., Light-controlled Graphene-elastin Composite Hydrogel Actuators. *Nano Letters* **2013**, 13 (6), 2826-2830.
82. Dong, L.; Zhao, Y., Photothermally Driven Liquid Crystal Polymer Actuators. *Materials Chemistry Frontiers* **2018**, 2 (11), 1932-1943.
83. Xing, H.; Li, J.; Shi, Y.; Guo, J.; Wei, J., Thermally Driven Photonic Actuator Based on Silica Opal Photonic Crystal With Liquid Crystal Elastomer. *ACS Applied Materials & Interfaces* **2016**, 8 (14), 9440-9445.
84. Liang, C.; Rogers, C. A.; Malafeew, E., Investigation of Shape Memory Polymers and Their Hybrid Composites. *J. Intell. Mater. Syst. Struct.* **1997**, 8 (4), 380-386.
85. Yu, K.; Xie, T.; Leng, J.; Ding, Y.; Qi, H. J., Mechanisms of Multi-shape Memory Effects and Associated Energy Release in Shape Memory Polymers. *Soft Matter* **2012**, 8 (20), 5687-5695.
86. Michal, B. T.; Spencer, E. J.; Rowan, S. J., Stimuli-responsive Reversible Two-level Adhesion From a Structurally Dynamic Shape-memory Polymer. *ACS Applied Materials & Interfaces* **2016**, 8 (17), 11041-11049.

87. Pelrine, R.; Kornbluh, R.; Pei, Q.; Joseph, J., High-speed Electrically Actuated Elastomers With Strain Greater Than 100%. *Science* **2000**, 287 (5454), 836-9.
88. Carpi, F.; Gallone, G.; Galantini, F.; De Rossi, D., Silicone–poly (hexylthiophene) Blends as Elastomers With Enhanced Electromechanical Transduction Properties. *Adv. Funct. Mater.* **2008**, 18 (2), 235-241.
89. Shintake, J.; Cacucciolo, V.; Shea, H.; Floreano, D., Soft Biomimetic Fish Robot Made of Dielectric Elastomer Actuators. *Soft Robotics* **2018**, 5 (4), 466-474.
90. Migliorini, L.; Santaniello, T.; Yan, Y.; Lenardi, C.; Milani, P., Low-voltage Electrically Driven Homeostatic Hydrogel-based Actuators for Underwater Soft Robotics. *Sensors Actuators B: Chem.* **2016**, 228, 758-766.
91. Yang, C.; Wang, W.; Yao, C.; Xie, R.; Ju, X.-J.; Liu, Z.; Chu, L.-Y., Hydrogel Walkers With Electro-driven Motility for Cargo Transport. *Sci. Rep.* **2015**, 5 (1), 13622.
92. Peng, L.; Liu, Y.; Huang, J.; Li, J.; Gong, J.; Ma, J., Microfluidic Fabrication of Highly Stretchable and Fast Electro-responsive Graphene Oxide/Polyacrylamide/Alginate Hydrogel Fibers. *Eur. Polym. J.* **2018**, 103, 335-341.
93. Shepherd, R. F.; Ilievski, F.; Choi, W.; Morin, S. A.; Stokes, A. A.; Mazzeo, A. D.; Chen, X.; Wang, M.; Whitesides, G. M., Multigait Soft Robot. *Proceedings of the National Academy of Sciences* **2011**, 108 (51), 20400-20403.
94. Wehner, M.; Truby, R. L.; Fitzgerald, D. J.; Mosadegh, B.; Whitesides, G. M.; Lewis, J. A.; Wood, R. J., An Integrated Design and Fabrication Strategy for Entirely Soft, Autonomous Robots. *Nature* **2016**, 536 (7617), 451-455.
95. Rothemund, P.; Ainla, A.; Belding, L.; Preston, D. J.; Kurihara, S.; Suo, Z.; Whitesides, G. M., A Soft, Bistable Valve for Autonomous Control of Soft Actuators. *Science Robotics* **2018**, 3 (16), eaar7986.
96. Marchese, A. D.; Onal, C. D.; Rus, D., Autonomous Soft Robotic Fish Capable of Escape Maneuvers Using Fluidic Elastomer Actuators. *Soft Robotics* **2014**, 1 (1), 75-87.
97. Chen, G.; Yang, X.; Zhang, X.; Hu, H., Water Hydraulic Soft Actuators for Underwater Autonomous Robotic Systems. *Applied Ocean Research* **2021**, 109, 102551.
98. Acome, E.; Mitchell, S. K.; Morrissey, T. G.; Emmett, M. B.; Benjamin, C.; King, M.; Radakovitz, M.; Keplinger, C., Hydraulically Amplified Self-healing Electrostatic Actuators With Muscle-like Performance. *Science* **2018**, 359 (6371), 61-65.
99. Henzl, J.; Mehlhorn, M.; Gawronski, H.; Rieder, K. H.; Morgenstern, K., Reversible Cis–Trans Isomerization of a Single Azobenzene Molecule. *Angew. Chem. Int. Ed.* **2006**, 45 (4), 603-606.
100. Yamada, M.; Kondo, M.; Mamiya, J.-i.; Yu, Y.; Kinoshita, M.; Barrett, C. J.; Ikeda, T., Photomobile Polymer Materials: Towards Light-driven Plastic Motors. *Angew. Chem. Int. Ed.* **2008**, 47 (27), 4986-4988.
101. Lu, X.; Guo, S.; Tong, X.; Xia, H.; Zhao, Y., Tunable Photocontrolled Motions Using Stored Strain Energy in Malleable Azobenzene Liquid Crystalline Polymer Actuators. *Advanced Materials* **2017**, 29 (28), 1606467.
102. Ma, S.; Li, X.; Huang, S.; Hu, J.; Yu, H., A Light-activated Polymer Composite Enables On-demand Photocontrolled Motion: Transportation at the Liquid/Air Interface. *Angew. Chem. Int. Ed.* **2019**, 58 (9), 2655-2659.
103. Jiang, Z.; Xu, M.; Li, F.; Yu, Y., Red-light-Controllable Liquid-crystal Soft Actuators via Low-power Excited Upconversion Based on Triplet–Triplet Annihilation. *Journal of the American Chemical Society* **2013**, 135 (44), 16446-16453.
104. Aldoshin, S. M.; Nikonova, L. A.; Smirnov, V. A.; Shilov, G. V.; Nagaeva, N. K., Structure and Photochromic Properties of Single Crystals of Spiropyran Salts. *J. Mol. Struct.* **2005**, 750 (1), 158-165.
105. Kortekaas, L.; Browne, W. R., The Evolution of Spiropyran: Fundamentals and Progress of an Extraordinarily Versatile Photochrome. *Chem. Soc. Rev.* **2019**, 48 (12), 3406-3424.
106. Dunne, A.; Delaney, C.; Florea, L.; Diamond, D., Solvato-morphologically Controlled, Reversible NIPAAm Hydrogel Photoactuators. *RSC Advances* **2016**, 6 (86), 83296-83302.
107. Goncalves, F. D.; Koo, J.-H.; Ahmadian, M., A Review of the State of the Art in Magnetorheological Fluid Technologies--Part I: Mr Fluid and Mr Fluid Models. *The Shock and Vibration Digest* **2006**, 38 (3), 203-220.

108. Phule, P. P., Magnetorheological (MR) Fluids: Principles and Applications. *Smart Materials Bulletin* **2001**, 2001 (2), 7-10.
109. Jackson, J. A.; Messner, M. C.; Dudukovic, N. A.; Smith, W. L.; Bekker, L.; Moran, B.; Golobic, A. M.; Pascall, A. J.; Duoss, E. B.; Loh, K. J., Field Responsive Mechanical Metamaterials. *Science Advances* **2018**, 4 (12), eaau6419.
110. Song, H.; Lee, H.; Lee, J.; Choe, J. K.; Lee, S.; Yi, J. Y.; Park, S.; Yoo, J.-W.; Kwon, M. S.; Kim, J., Reprogrammable Ferromagnetic Domains for Reconfigurable Soft Magnetic Actuators. *Nano Lett.* **2020**, 20 (7), 5185-5192.
111. Xie, H.; Sun, M.; Fan, X.; Lin, Z.; Chen, W.; Wang, L.; Dong, L.; He, Q., Reconfigurable Magnetic Microrobot Swarm: Multimode Transformation, Locomotion, and Manipulation. *Science Robotics* **2019**, 4 (28), eaav8006.
112. Tang, J.; Yin, Q.; Shi, M.; Yang, M.; Yang, H.; Sun, B.; Guo, B.; Wang, T., Programmable Shape Transformation of 3D Printed Magnetic Hydrogel Composite for Hyperthermia Cancer Therapy. *Extreme Mechanics Letters* **2021**, 46, 101305.
113. Tang, J.; Tong, Z.; Xia, Y.; Liu, M.; Lv, Z.; Gao, Y.; Lu, T.; Xie, S.; Pei, Y.; Fang, D.; Wang, T. J., Super Tough Magnetic Hydrogels for Remotely Triggered Shape Morphing. *J. Mater. Chem. B.* **2018**, 6 (18), 2713-2722.
114. Islam, M. R.; Li, X.; Smyth, K.; Serpe, M. J., Polymer-based Muscle Expansion and Contraction. *Angew. Chem. Int. Ed.* **2013**, 52 (39), 10330-10333.
115. Lee, B. P.; Konst, S., Novel Hydrogel Actuator Inspired by Reversible Mussel Adhesive Protein Chemistry. *Advanced Materials* **2014**, 26 (21), 3415-3419.
116. Meng, H.; Zheng, J.; Wen, X.; Cai, Z.; Zhang, J.; Chen, T., pH- and Sugar-induced Shape Memory Hydrogel Based on Reversible Phenylboronic Acid-diol Ester Bonds. *Macromolecular Rapid Communications* **2015**, 36 (6), 533-537.
117. Zhang, X.; Zhao, C.; Xiang, N.; Li, W., Chain Entanglements and Hydrogen Bonds in Carbopol Microgel Reinforced Hydrogel. *Macromolecular Chemistry and Physics* **2016**, 217 (19), 2139-2144.
118. Le, X.; Zhang, Y.; Lu, W.; Wang, L.; Zheng, J.; Ali, I.; Zhang, J.; Huang, Y.; Serpe, M. J.; Yang, X.; Fan, X.; Chen, T., A Novel Anisotropic Hydrogel With Integrated Self-deformation and Controllable Shape Memory Effect. *Macromolecular Rapid Communications* **2018**, 39 (9), 1800019.
119. Liu, S.; Gao, G.; Xiao, Y.; Fu, J., Tough and Responsive Oppositely Charged Nanocomposite Hydrogels for Use as Bilayer Actuators Assembled Through Interfacial Electrostatic Attraction. *Journal of Materials Chemistry B* **2016**, 4 (19), 3239-3246.
120. Huang, L.; Jiang, R.; Wu, J.; Song, J.; Bai, H.; Li, B.; Zhao, Q.; Xie, T., Ultrafast Digital Printing Toward 4D Shape Changing Materials. *Advanced Materials* **2017**, 29 (7), 1605390.
121. Ma, Y.; Hua, M.; Wu, S.; Du, Y.; Pei, X.; Zhu, X.; Zhou, F.; He, X., Bioinspired High-power-Density Strong Contractile Hydrogel by Programmable Elastic Recoil. *Science Advances* **2020**, 6 (47), eabd2520.
122. Ma, C.; Li, T.; Zhao, Q.; Yang, X.; Wu, J.; Luo, Y.; Xie, T., Supramolecular Lego Assembly Towards Three-dimensional Multi-responsive Hydrogels. *Advanced Materials* **2014**, 26 (32), 5665-5669.
123. Whitesides, G. M., Bioinspiration: Something for Everyone. *Interface Focus* **2015**, 5 (4), 20150031.
124. Aubin, C. A.; Choudhury, S.; Jerch, R.; Archer, L. A.; Pikul, J. H.; Shepherd, R. F., Electrolytic Vascular Systems for Energy-dense Robots. *Nature* **2019**, 571 (7763), 51-57.
125. Li, Z.; Hu, S.; Cheng, K., Platelets and Their Biomimetics for Regenerative Medicine and Cancer Therapies. *Journal of Materials Chemistry B* **2018**, 6 (45), 7354-7365.
126. Dang, M.; Saunders, L.; Niu, X.; Fan, Y.; Ma, P. X., Biomimetic Delivery of Signals for Bone Tissue Engineering. *Bone Research* **2018**, 6 (1), 25.
127. Cianchetti, M.; Arienti, A.; Follador, M.; Mazzolai, B.; Dario, P.; Laschi, C., Design Concept and Validation of a Robotic Arm Inspired by the Octopus. *Materials Science and Engineering C* **2011**, 31 (6), 1230-1239.
128. Cianchetti, M.; Calisti, M.; Margheri, L.; Kuba, M.; Laschi, C., Bioinspired Locomotion and Grasping in Water: The Soft Eight-arm Octopus Robot. *Bioinspiration & Biomimetics* **2015**, 10 (3), 035003.

129. Kazakidi, A.; Zabulis, X.; Tsakiris, D., Vision-based 3D Motion Reconstruction of Octopus Arm Swimming and Comparison With an 8-Arm Underwater Robot. *Proceedings - IEEE International Conference on Robotics and Automation* **2015**, 2015, 1178-1183.
130. Calisti, M.; Corucci, F.; Arienti, A.; Laschi, C., Dynamics of Underwater Legged Locomotion: Modeling and Experiments on an Octopus-inspired Robot. *Bioinspiration & Biomimetics* **2015**, 10 (4), 046012.
131. Pellegrino, H. Y. a. S., Bi-stable Cylindrical Space Frames. In *American Institute of Aeronautics and Astronautics* 2005; p 1870.
132. Matoba, H.; Ishikawa, T.; Kim, C.; Muller, R. S. In *A bistable snapping microactuator*, Proceedings IEEE Micro Electro Mechanical Systems An Investigation of Micro Structures, Sensors, Actuators, Machines and Robotic Systems, 25-28 Jan. **1994**; 1994; pp 45-50.
133. Sorrell, C. D.; Serpe, M. J., Reflection Order Selectivity of Color-tunable Poly(N-isopropylacrylamide) Microgel Based Etalons. *Advanced Materials* **2011**, 23 (35), 4088-4092.
134. Carvalho, W. S. P.; Lee, C.; Zhang, Y.; Czarnecki, A.; Serpe, M. J., Probing the Response of Poly (N-isopropylacrylamide) Microgels to Solutions of Various Salts Using Etalons. *Journal of Colloid and Interface Science* **2021**, 585, 195-204.
135. Brochu, P.; Pei, Q., Advances in Dielectric Elastomers for Actuators and Artificial Muscles. *Macromolecular Rapid Communications* **2010**, 31 (1), 10-36.
136. Sivaperuman Kalairaj, M.; Banerjee, H.; Lim, C. M.; Chen, P.-Y.; Ren, H., Hydrogel-matrix Encapsulated Nitinol Actuation With Self-cooling Mechanism. *RSC Advances* **2019**, 9 (59), 34244-34255.
137. Hempenius, M. A.; Cirimi, C.; Savio, F. L.; Song, J.; Vancso, G. J., Poly(Ferrocenylsilane) Gels and Hydrogels With Redox-controlled Actuation. *Macromol. Rapid Commun.* **2010**, 31 (9-10), 772-783.
138. Velders, A. H.; Dijkman, J. A.; Saggiomo, V., Hydrogel Actuators as Responsive Instruments for Cheap Open Technology (HARICOT). *Applied Materials Today* **2017**, 9, 271-275.
139. Ma, Y.; Hua, M.; Wu, S.; Du, Y.; Pei, X.; Zhu, X.; Zhou, F.; He, X., Bioinspired High-power-Density Strong Contractile Hydrogel by Programmable Elastic Recoil. *Science Advances* 6 (47), eabd2520.
140. Lee, S.-H.; Kim, T. H.; Lima, M. D.; Baughman, R. H.; Kim, S. J., Biothermal Sensing of a Torsional Artificial Muscle. *Nanoscale* **2016**, 8 (6), 3248-3253.
141. Lo, C.-Y.; Zhao, Y.; Kim, C.; Alsaied, Y.; Khodambashi, R.; Peet, M.; Fisher, R.; Marvi, H.; Berman, S.; Aukes, D.; He, X., Highly Stretchable Self-sensing Actuator Based on Conductive Photothermally-responsive Hydrogel. *Mater. Today* **2021**, 50, 35-43.
142. Li, J.; Zhang, R.; Mou, L.; Jung de Andrade, M.; Hu, X.; Yu, K.; Sun, J.; Jia, T.; Dou, Y.; Chen, H.; Fang, S.; Qian, D.; Liu, Z., Photothermal Bimorph Actuators With In-built Cooler for Light Mills, Frequency Switches, and Soft Robots. *Adv. Funct. Mater.* **2019**, 29 (27), 1808995.
143. Brann, T.; Patel, D.; Chauhan, R.; James, K. T.; Bates, P. J.; Malik, M. T.; Keynton, R. S.; O'Toole, M. G., Gold Nanoplates as Cancer-targeted Photothermal Actuators for Drug Delivery and Triggered Release. *Journal of Nanomaterials* **2016**, 2016, 2036029.
144. Yang, D.; Verma, M. S.; So, J.-H.; Mosadegh, B.; Keplinger, C.; Lee, B.; Khashai, F.; Lossner, E.; Suo, Z.; Whitesides, G. M., Buckling Pneumatic Linear Actuators Inspired by Muscle. *Advanced Materials Technologies* **2016**, 1 (3), 1600055.
145. Li, Y.; Wang, J.; Li, H.; Huang, L.; Chen, L.; Ni, Y.; Zheng, Q., Highly Transparent RCF/PTFE Humidity and IR Light Dual-driven Actuator With High Force Density, Sensitivity and Stability. *Appl. Surf. Sci.* **2022**, 572, 151502.
146. Li, H.; Li, R.; Wang, K.; Hu, Y., Dual-responsive Soft Actuator Based on Aligned Carbon Nanotube Composite/Graphene Bimorph for Bioinspired Applications. *Macromolecular Materials and Engineering* **2021**, 306 (8), 2100166.
147. Gao, Y.; Ahiabu, A.; Serpe, M. J., Controlled Drug Release From the Aggregation–Disaggregation Behavior of pH-responsive Microgels. *ACS Applied Materials & Interfaces* **2014**, 6 (16), 13749-13756.
148. Wong, W. S. Y.; Li, M.; Nisbet, D. R.; Craig, V. S. J.; Wang, Z.; Tricoli, A., Mimosa Origami: A Nanostructure-enabled Directional Self-organization Regime of Materials. *Science Advances* 2 (6), e1600417.

149. Le, X.; Lu, W.; Xiao, H.; Wang, L.; Ma, C.; Zhang, J.; Huang, Y.; Chen, T., Fe³⁺-, pH-, Thermoresponsive Supramolecular Hydrogel With Multishape Memory Effect. *ACS Applied Materials & Interfaces* **2017**, *9* (10), 9038-9044.
150. Xu, Z.; Li, J.; Gao, G.; Wang, Z.; Cong, Y.; Chen, J.; Yin, J.; Nie, L.; Fu, J., Tough and Self - Recoverable Hydrogels Crosslinked by Triblock Copolymer Micelles and Fe³⁺ Coordination. *J. Polym. Sci., Part B: Polym. Phys.* **2018**, *56* (11), 865-876.
151. Chen, Q.; Yan, X.; Zhu, L.; Chen, H.; Jiang, B.; Wei, D.; Huang, L.; Yang, J.; Liu, B.; Zheng, J., Improvement of Mechanical Strength and Fatigue Resistance of Double Network Hydrogels by Ionic Coordination Interactions. *Chem. Mater.* **2016**, *28* (16), 5710-5720.
152. Strachotová, B.; Strachota, A.; Uchman, M.; Šlouf, M.; Brus, J.; Pleštil, J.; Matějka, L., Super Porous Organic-Inorganic Poly (N-isopropylacrylamide)-Based Hydrogel With a Very Fast Temperature Response. *Polymer* **2007**, *48* (6), 1471-1482.
153. Huerta-Angeles, G.; Hishchak, K.; Strachota, A.; Strachota, B.; Šlouf, M.; Matějka, L., Super-porous Nanocomposite PNIPAm Hydrogels Reinforced With Titania Nanoparticles, Displaying a Very Fast Temperature Response as Well as pH-sensitivity. *Eur. Polym. J.* **2014**, *50*, 341-352.
154. Tien, H. N.; Hien, N. T. M.; Oh, E.-S.; Chung, J.; Kim, E. J.; Choi, W. M.; Kong, B.-S.; Hur, S. H., Synthesis of a Highly Conductive and Large Surface Area Graphene Oxide Hydrogel and Its Use in a Supercapacitor. *Journal of Materials Chemistry A* **2013**, *1* (2), 208-211.
155. Kim, J. H.; Lee, S. B.; Kim, S. J.; Lee, Y. M., Rapid Temperature/PH Response of Porous Alginate-g-Poly (N-isopropylacrylamide) Hydrogels. *Polymer* **2002**, *43* (26), 7549-7558.
156. Sehaqui, H.; Zhou, Q.; Ikkala, O.; Berglund, L. A., Strong and Tough Cellulose Nanopaper With High Specific Surface Area and Porosity. *Biomacromolecules* **2011**, *12* (10), 3638-3644.

Appendix A

Studies on Temperature & Salt Responses of PNIPAm-based Hydrogels

A.1 Introduction

Interests in stimuli-responsive hydrogels continue to grow due to the advancement in the field of soft robotics. Hydrogels, which resemble human tissues, are 3D polymeric networks that can hold large amounts of water. The response of the hydrogel is mostly resulted from the expulsion of water, resulting in the collapse of the structure and a dramatic reduction in the hydrogels size. This response can be induced by a change in external stimuli, such as ionic strength, pH, and temperature. The muscle-like characteristic of hydrogels makes them suitable for a variety of possible uses including sensors, drug delivery systems, and mobility assistive devices. Despite being of high importance in practical application, the key feature, which is the response rate, still is not yet adequate. Hence, we aim to focus on the response rate improvement, temperature and salt response, specifically.

In this project, Poly N-isopropylacrylamide (pNIPAm) based hydrogels were investigated for both temperature and salt response. We investigated the response of a pNIPAm hydrogel using N, N-methylenebisacrylamide (BIS) as the crosslinker, and studied how this response differs from hydrogels using different types of crosslinkers or monomers. Specifically, poly(ethylene glycol) diacrylate (PEGDA) and poly(vinyl alcohol) (PVA) were investigated.

A.2 Experimental Section

Materials: The N-isopropylacrylamide monomer (NIPAm) (MW = 113.16 g/mol) was obtained from TCI Chemicals (Tokyo, Japan), and was recrystallized in hexane before use. N, N-methylenebisacrylamide (BIS, 99%), poly(ethylene glycol) diacrylate (PEGDA, average Mn 250 or 700), poly(vinyl alcohol) (PVA, Mw 86,000 or 146,000-186,000), 2,2-diethoxyacetophenone (DEAP, PI, >95%), potassium chloride (KCl, 99.0-100.5%) were purchased from Sigma Aldrich (St. Louis, Missouri, USA). All the

chemicals were used as received without further purification, unless otherwise indicated. UV lamp (Model B 100 AP, 365nm) was purchased from UVP (San Gabriel, CA, USA).

Synthesis of the PNIPAm Hydrogel: The pre-solution containing 0.67 M NIPAm monomer, 40 μ L of 2,2-diethoxyacetophenone (DEAP) as the photo initiator (PI), and 1.318% (a.t.% to NIPAm) of BIS as the crosslinker were mixed well in a 10 mL centrifuge tube. The solution was vortexed until all solids dissolved and degassed for 45 s using nitrogen gas. All samples that contained PI were wrapped in tinfoil and kept out of direct sunlight to avoid polymerization. For the synthesis of each varying sample, the additional components were added together with BIS. To fabricate the hydrogel, the pre-solution was injected into a rectangular Teflon gasket clamped between two glass slides, which was sealed and placed on a cold plate at 0 °C for 2 min. Next, the sample was exposed to the UV light at an angel of 45° for a certain period of time (Figure A.1). The sample was removed from the UV light, removed from the Teflon gasket, rinsed with DI water, and submerged in a petri dish with DI water for about 24 hours to reach equilibrium. Before testing, the samples were cut into 1.5 cm x 1.5 cm squares (exact sizes were used in calculations).

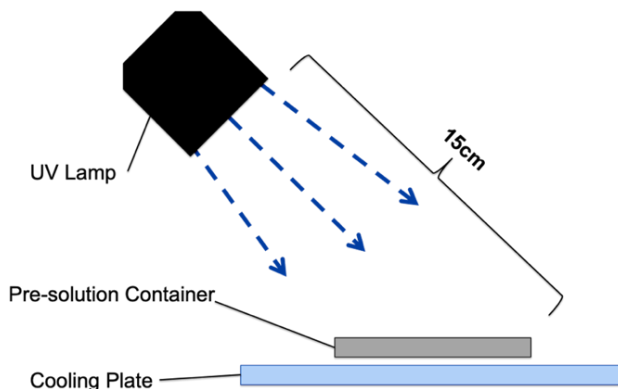


Figure A.1. The setup for the synthesis of hydrogels. The pre-solution sample was clamped between glass slides and put on top of a cooling plate. The UV lamp was placed at a 45° angle, irradiating the surface of the pre-solution container.

Variations of Hydrogel Synthesis:

PNIPAm + BIS Hydrogels: Samples were made with varying concentrations of BIS from 0.1-2% (a.t.% to NIPAm) and UV exposure times of 20-60 min.

PNIPAm + PEGDA Hydrogels: Samples were made by replacing the BIS cross linker with PEGDA (Avg Mw = 700) in concentrations of 1-5% (a.t.% to NIPAM). UV exposure time was 30 min.

PNIPAM + BIS + PEGDA Hydrogels: Samples were made with the addition of PEGDA (Avg Mw = 250) at concentrations of 1-5% (a.t.% to NIPAM). UV exposure time was 30 min.

PNIPAM + BIS + PVA Hydrogels: Samples were made with the addition of PVA (Avg Mw = 86,000 or 146,000-186,000) at concentrations of 1-5% (w.t.% to solution water content). UV exposure time was 60 min.

Thermal Response Test: The response to temperature was calculated by monitoring the size change of a sample hydrogel equilibrated at room temperature (25 °C) after immersion in 55 °C water for 2 min. The thickness of the sample (0.25 mm) did not change significantly, so only the area was measured.

Salt Response Test: The response to salt was studied by submerging the hydrogel samples into a 0.74 M potassium chloride (KCl) solution. The response was monitored by measuring the size change. The thickness of the sample (0.25 mm) did not change significantly, so only the area was measured.

A.3 Results and Discussion

In this chapter, we aim to study the temperature and salt responses of the pNIPAm hydrogels and variations with slight composition changes. The experiments were performed once only, which may result in larger errors and deviations. The preliminary results were presented as follows just for crude discussions. Further experiments and repetitions are needed for future in-depth studies.

A.3.1 PNIPAm/BIS-based Hydrogel Tests

At first, the characterization of the simple PNIPAm + BIS hydrogel was carried out. This series of experiments was used as a comparison for the rest of the experiments. As seen in Figure A.2, the results showed that with increased concentration of BIS, the hydrogel size change decreased. Also, it was noted that the reduction in UV exposure time caused larger size changes. However, for samples with lower BIS concentrations,

reduced UV exposure times resulted in no substantial polymerization, hence these samples did not undergo thermal response testing.

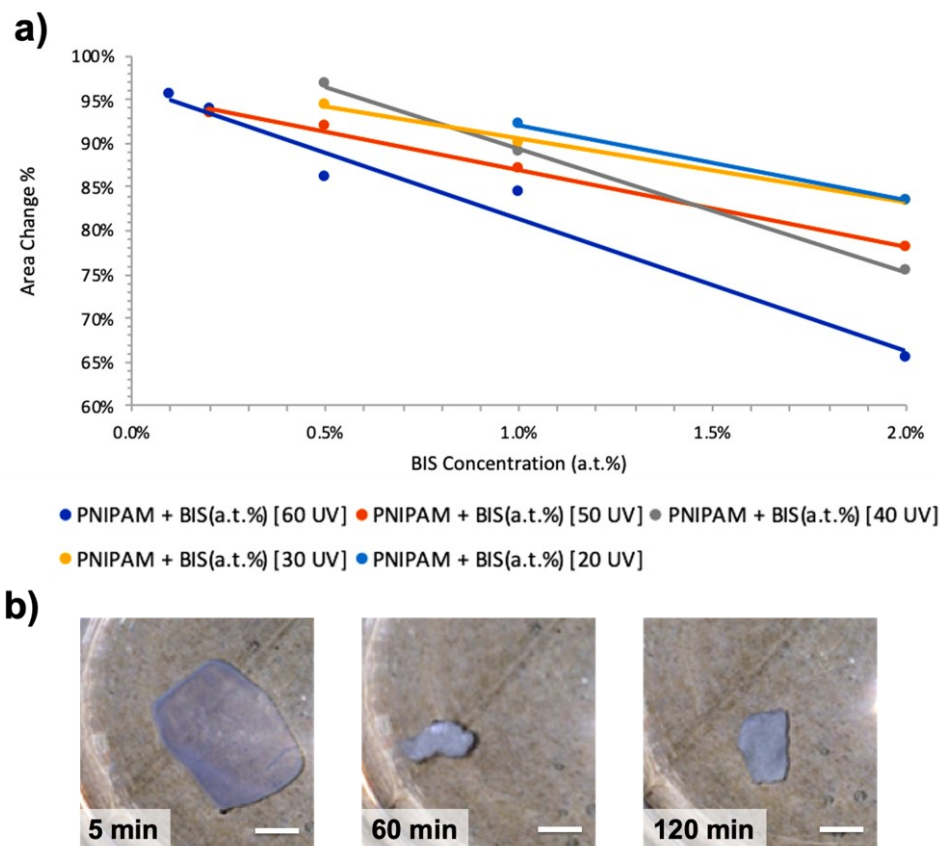


Figure A.2. Hydrogel thermal response results and experimental pictures of the hydrogel shape changing. a) Hydrogel size change with different BIS concentrations. Different colored lines represented different UV exposure times; b) pictures of a piece of hydrogel (1 a.t.% BIS, 30 min UV exposure) immersed in 55 °C water after 5 min, 60 min, and 120 min, respectively. (Scale bar represents 0.5 cm in length.)

The effect of UV exposure time on polymerization was down to the radical formation. Shorter UV exposure time means less radical formation thus less crosslinking within the polymer network; less crosslinking resulted in larger water content and larger size changes. The effect of the BIS concentration also can be attributed to the crosslinking density. A higher BIS concentration corresponds to more crosslinking points among polymer chains, giving rise to smaller size changes. Additionally, it was observed qualitatively that the lower concentrations of BIS resulted in a softer hydrogel. Some other observations included the appearance of white spots

on some of the samples. This was thought to be caused by overheating of this portion of the sample during the synthesis. When all further samples were synthesised on a cooling plate, no further white spots were observed.

The 60 min UV exposure time (60 UV) pNIPAm + BIS hydrogel was tested for its response to KCl salt solution (Figure A.3). Similarly, when BIS concentration was increased, the size changes decreased. It was speculated that the response was a result of the osmotic pressure effects.

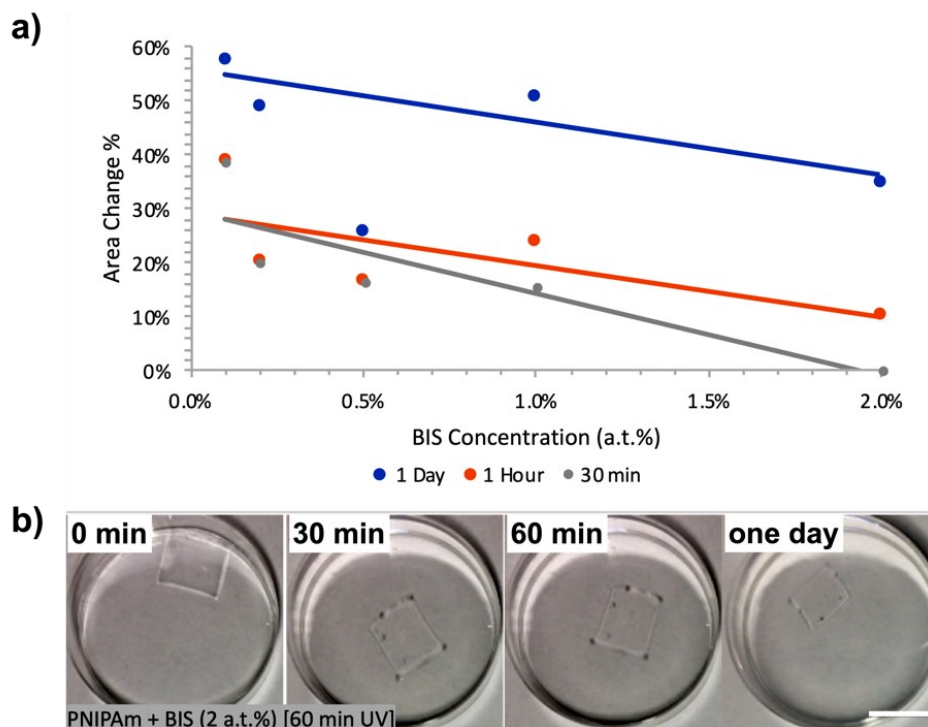


Figure A.3. Hydrogel KCl response results and experimental pictures of the hydrogel shape changing. a) Hydrogel size change with different BIS concentrations. Different colored lines represented different soaking times; b) pictures of a piece of hydrogel (2 a.t.% BIS, 60 min UV exposure) immersed in KCl solution after 0 min, 30 min, 60 min, and one day, respectively. (Scale bar represents 1.5 cm in length.)

A.3.2 PEDGA-based Hydrogel Tests

PNIPAm + PEGDA and pNIPAm + BIS + PEGDA samples were tested for the salt response. Unlike the pNIPAm + BIS sample, the pNIPAm + PEGDA sample showed a positive correlation between the concentration of PEGDA and the hydrogel size change (Figure A.4). This difference suggested that the size change was resulted from the interaction between PEGDA and the salt. This response could be attributed to the

coordination interactions of the with the PEGDA linker. As a result, the PEGDA chains switched from the extended state to the coiled state, surrounding the K^+ ion in the center, which caused the network to reduce its size.

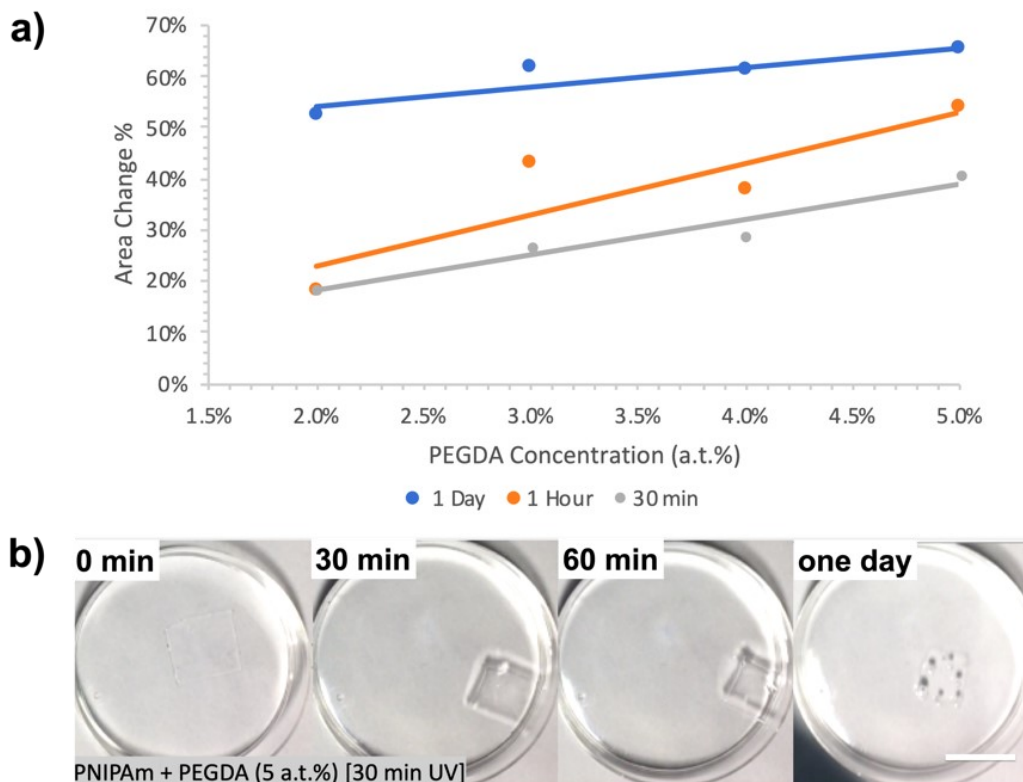


Figure A.4. PEGDA-based hydrogel in response to KCl and experimental pictures of the hydrogel shape changing. a) Hydrogel size change with different PEGDA concentrations. Different colored lines represented different soaking times; b) pictures of a piece of hydrogel (5 a.t.% PEGDA, 30 min UV exposure) immersed in KCl solution after 0 min, 30 min, 60 min, and one day, respectively. (Scale bar represents 1.5 cm in length.)

Interestingly, the same effect was not obvious for pNIPAm + BIS + PEGDA hydrogels (Figure A.5). The varying concentration of PEGDA had little effect on the size change, especially for shorter soaking times. It showed close to no correlation with a minor positive trend for the samples soaked for one day. This suggested that the presence of the extra BIS crosslinker might restrict the possible structural deformation. When BIS was present, the overall crosslinking density was higher, as long as the network rigidity. This could significantly reduce the effectiveness of PEGDA bringing the network closer.

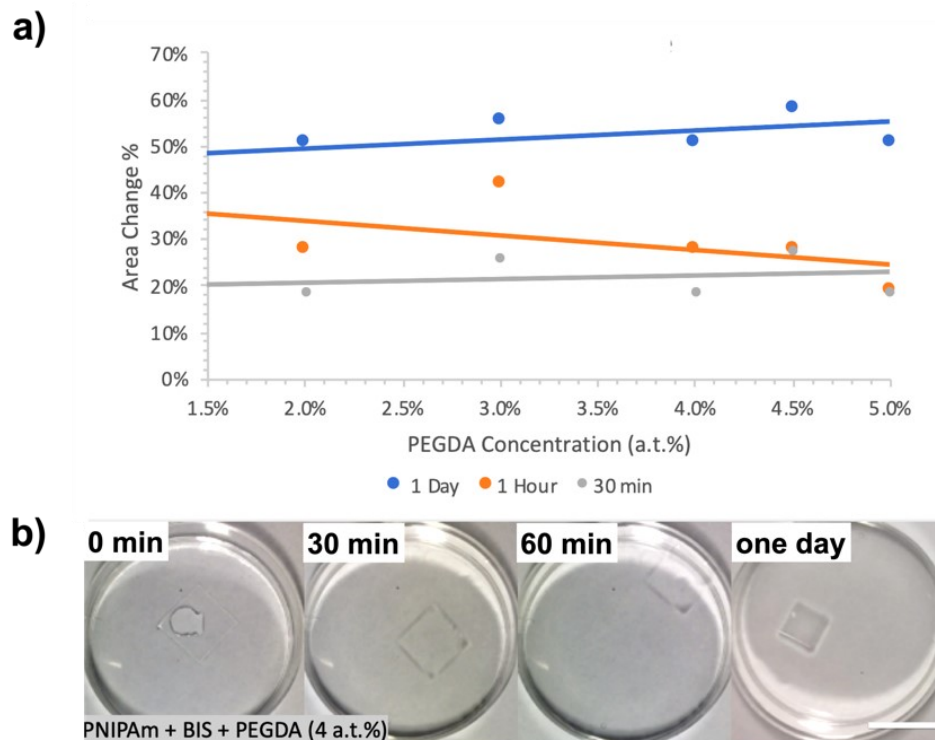


Figure A.5. PEGDA+BIS-based hydrogel in response to KCl and experimental pictures of the hydrogel shape changing. a) Hydrogel size change with different PEGDA concentrations. Different colored lines represented different soaking times; b) pictures of a piece of hydrogel (4 a.t.% PEGDA) immersed in KCl solution after 0 min, 30 min, 60 min, and one day, respectively. (Scale bar represents 1.5 cm in length.)

The salt responses for all the tested pNIPAm based samples were incredibly slow with most not achieving max reduction in size until a period of 24 hours had passed. PEGDA-based polymers did show the most promise however the rate of response is not fast enough at this moment for desired application. It is also to be noted that hydrogels only returned fully to its original size after removed from the salt solution and left in DI water for several days, which indicated the strong coordination interactions between PEGDA and K^+ ions.

A.3.3 PVA-based Hydrogel Tests

The response of PVA-based pNIPAm hydrogels was very fast. The thermal response was close to one magnitude faster than the BIS-based hydrogels, and the qualitative strength was greater. Preliminary tests showed a large size change occurred within five seconds of exposure to the 55 °C DI water. This response rate was extremely fast

compared to the BIS-based hydrogel, which was close to 120 seconds. With higher concentration of the PVA, the response rate also was faster. Interestingly, not only the concentration but also the chain length of the PVA affected the response. 86,000 Mw and 146,000 Mw PVA were used in different samples for the chain length effect comparison. The results showed that longer PVA chains rendered the hydrogel with larger size changes. This synthesis method involved no covalent bonding of the linear PVA chains to the pNIPAm + BIS network. Instead, an intertwining of the two polymer networks were formed. Due to the hydrophilicity of PVA, the structure could uptake more water into the network. Moreover, the linear PVA chains creating channel-like structures resulted in more efficient water exchange in/out from the network, hence a faster response rate.

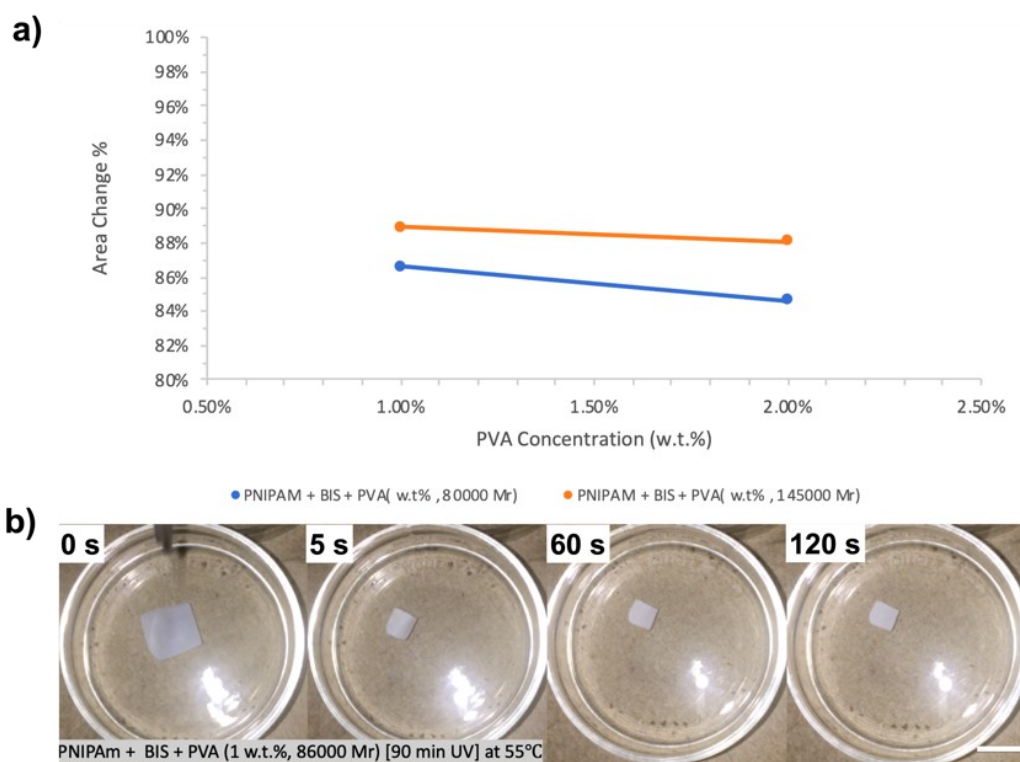


Figure A.6. PVA-based hydrogel thermal response test and experimental pictures of the hydrogel shape changing. a) Hydrogel size change with different PVA concentrations. Different colored lines represented different molecular weight of PVA used; b) pictures of a piece of hydrogel (1 w.t.% PVA, 86,000 Mr) immersed in 55 DI water after 0 s, 5 s, 60 s, and 120 s, respectively. (Scale bar represents 1.5 cm in length.)

A.4 Conclusions and Outlook

To conclude, we investigated the thermal and salt responses in various pNIPAm-based hydrogels. Specifically, we studied the BIS concentration effect on the response of pNIPAm hydrogels. More BIS resulted in higher crosslinking density and network rigidity, thus smaller size change and response rate in both thermal and salt responses. Meanwhile, we investigated the PEGDA effect on the KCL salt response. We speculated that due to the coordination interaction between the K^+ ions and PEG chains, the hydrogel crosslinked by PEGDA showed larger size reduction with higher PEGDA incorporation content. This work opened up more possible applications using the similar mechanism. Moreover, PVA showed a promising effect on improving the pNIPAm hydrogel response rate by improving its hydrophilicity and creating water channels for more efficient water exchange. Longer PVA chains also provided long range interaction inside the hydrogel network, showing better improvement compared to shorter PVA counterparts.

However, there still are many problems to solve before definite conclusions can be drawn. For example, more repetitions are needed for all the tests. Also, how to improve the response rate while maintaining the mechanical strength of the hydrogels remain the difficulties in this research area. Hopefully, our research can provide some insights into the advancement of related research and inspire more novel designs and applications.

Appendix B

Poly(Ethylene Glycol) Diacrylate-based Hydrogel Actuators in Response to Alkaline Potassium Ions

B.1 Introduction

In the previous appendix, we mentioned the poly(ethylene glycol) diacrylate-based hydrogel that can respond to K^+ ions due to coordination interactions between the alkaline metal ions and the PEG chains (Rowan, S. J.; Cantrill, S. J.; Cousins, G. R.; Sanders, J. K.; Stoddart, J. F., Dynamic covalent chemistry. *Angew. Chem. Int. Ed.* **2002**, *41* (6), 898-952.). This interaction resulted in the shrinkage of the hydrogel, which can be used as a novel actuation mechanism for stimuli-responsive actuators.

In this chapter, we investigated how PEGDA can affect the hydrogel network when the gel is in contact with the alkaline metal ions. In addition, we fabricated a helical-structured bilayer actuator composed of a PDMS passive layer and a PEGDA incorporated pNIPAm hydrogel active layer. When exposed in KCl solution, the helical structure responded to the alkaline metal ions by shrinking the active layer thus resulting in the shortening of the helical structure.

B.2 Experimental Section

Materials: The N-isopropylacrylamide monomer (NIPAm) (MW = 113.16 g/mol) was obtained from TCI Chemicals (Tokyo, Japan), and was recrystallized in hexane before use. N, N-methylenebisacrylamide (BIS, 99%), poly(ethylene glycol) diacrylate (PEGDA, average Mn 250), poly(diallyldimethylammonium chloride) solution (PDADMAC, Mw 400.000-500.000, 20 wt% in H₂O), 2,2-diethoxyacetophenone (DEAP, PI, >95%), potassium chloride (KCl, 99.0-100.5%) were purchased from Sigma Aldrich (St. Louis, Missouri, USA). Sylgard 184 silicone elastomer base and Sylgard 184 curing were obtained from Dow (Midland, Michigan, United States). All the chemicals were used as received without further purification, unless otherwise indicated. UV lamp (Model B 100 AP, 365nm) was purchased from UVP (San Gabriel, CA, USA).

Synthesis of the PEGDA-based Hydrogel: NIPAm, BIS, PEGDA, PDADMAC, and DEAP were weighed and mixed well in a centrifuge tube wrapped by tinfoil. The pre-solution was purged in nitrogen gas for 5 min, and stored in the fridge at 4 °C for later use. To synthesize the hydrogel, a rectangular shape was carved out from the center of a Teflon sheet to afford a gasket. The gasket was sandwiched between two glass slides, and the pre-solution was injected into the Teflon gasket. The gasket was sealed properly by clamping with some binder clips. The final assembly was irradiated under the UV light for 5 min to polymerize the hydrogels. The obtained hydrogels were rinsed with DI water and soaked in DI water to reach equilibrium for later tests.

Synthesis of the PDMS Passive Layer: SYLGARD™ 184 Silicone Elastomer Kit from Dow Inc. (Midland, Michigan, USA) was purchased from Sigma-Aldrich. A polymeric base and curing agent were mixed in a 10:1 ratio. It was mixed well, and the mixture poured into a large Petri dish. The Petri dish was placed on a heating plate overnight at 65 °C. The cured PDMS sheet was cut into long strips for bilayer actuator fabrication.

Fabrication of the PEGDA-based Hydrogel/PDMS Bilayer Actuator: A piece of PDMS sheet was placed in the Teflon gasket. On top of it, some hydrogel pre-solution was poured to fill the gasket. The assembly was irradiated under the UV light to polymerize the hydrogel; the gel and the PDMS sheet were bond together in this step. The afforded bilayer actuator was placed in DI water to reach equilibrium.

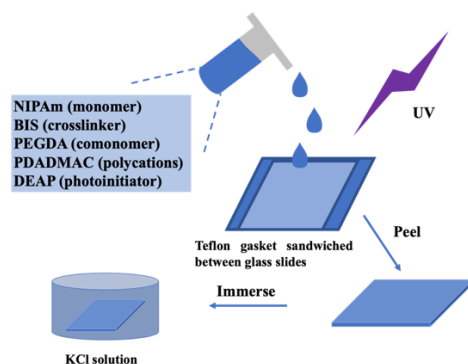


Figure B.1. The scheme for the synthesis of hydrogels. The pre-solution was mixed well in a centrifuge tube and poured into a Teflon gasket sandwiched between two glass slides. The solution was irradiated under UV light to polymerize. The afforded hydrogel was peeled from the mold and tested in a KCl solution.

Hydrogel in KCl Salt Solution Test: The response to salt was studied by submerging the hydrogel samples into a 1.0 M potassium chloride (KCl) solution. The response was monitored by recording the size change.

Actuator in KCl Salt Solution Test: The equilibrated bilayer actuator was immersed in a 1.0 M potassium chloride (KCl) solution. The shape morphing was recorded using a camera.

B.3 Results and Discussion

In this chapter, we aim to investigate how PEGDA-based hydrogels respond to KCl alkaline metal ions. As we speculated, the mechanism of the PEGDA in response to alkaline metal ions is the coordination interaction, which can bring the extended polymer network to a coiled, more compact state (Figure B.2a). Moreover, we came up with the bilayer actuator design composed of a PDMS passive layer and a PEGDA-based hydrogel active layer (Figure B.2b). When the bilayer actuator is exposed to KCl alkaline metal ion solution, the active layer will shrink while the passive PDMS layer remains unchanged. Due to the imbalance between the two layers, the bilayer structure will deform, depending on the geometry of the bilayer structure. The experiments were performed once, however, the preliminary results showed promising applications of this mechanism being used for various actuation designs.

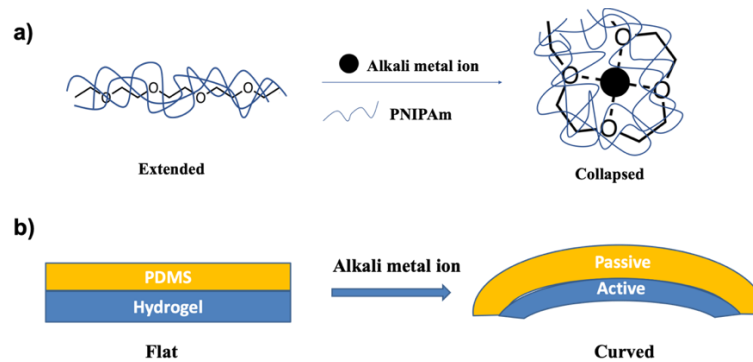


Figure B.2. Illustrations of the mechanisms for the actuation and the actuator design. a) Coordination interaction between the PEG structural units and the alkaline metal ions; the polymer network changes from the extended state to the coiled state; b) bilayer actuator design composed of a PDMS passive layer and a PEGDA-based hydrogel active layer; the bilayer actuator cross-section changes from the flat state to a curved state, resulting in shape morphing of the whole actuator.

B.3.1 PEGDA-based Hydrogel Salt Response Tests

At first, the salt response to KCl alkaline metal ion solution was tested. For comparison, hydrogel with no PEGDA was also tested. As seen in Figure B.3a, the hydrogel with no PEGDA shrank in size after soaking in KCl solution. This was attributed to osmotic pressure effect when the hydrogel was soaked in high concentration salt solution. However, for hydrogels with 10% PEGDA, we observed a larger size reduction, which was resulted from the coordination interaction between the PEG chains and the alkaline metal ion K^+ . Interestingly, when PEGDA concentration was increased, we noticed that the size changes became smaller. We speculated that due to the increasing concentration of PEGDA, the crosslinking density of the hydrogel was increased, which also increased the rigidity of the gel, resulting in less water exchange. From this result (Figure B.3b), we hypothesized that there might be an optimum concentration between 0% and 10% of PEGDA incorporation. Further experiments were carried out to investigate this hypothesis.

We varied the incorporation concentration of the PEGDA from 0% to 10%, and performed some similar salt response tests (Figure B.3c). As can be seen, similar phenomenon was observed. From the salt response tests, we can see a large volume reduction for samples with 8% PEGDA incorporation within 25 min.

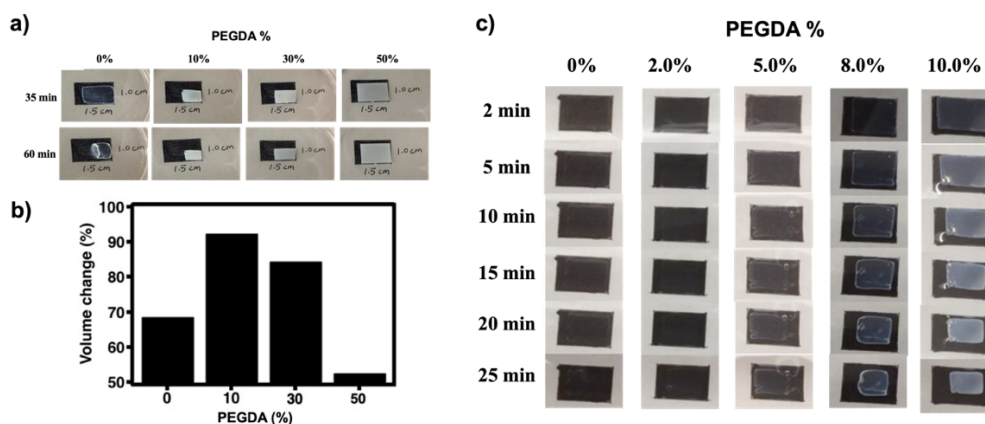


Figure B.3. Hydrogel KCl salt response. a) Pictures of hydrogels with 0%, 10 %, 30%, and 50% of PEGDA incorporation after soaking in salt solution for 35 min and 60 min (black rectangles were the original sizes when they were cut); b) a bar graph showing the size change for different PEGDA incorporations; c) pictures of hydrogels with 0%, 2.0%, 5.0%, 8.0%, and 10.0% of PEGDA incorporation after soaking in salt solution.

B.3.2 PEDGA-based Hydrogel/PDMS Bilayer Actuators

The PEGDA-based hydrogel/PDMS bilayer actuator was tested for the salt response. Due to the innate property of the bilayer structure geometry, the bilayer actuator adopted a helical structure with the swollen hydrogel layer exposed to the outside after soaked in DI water (Figure B.4a). After immersed in the KCl solution, the bilayer actuator started to change its shape. As seen in Figure B.4b-f, the helical structure started to unravel, resulting in a shorter and thicker helical structure due to the shrinkage of the hydrogel layer. This response could be attributed to the coordination interactions between the alkaline metal ions and the PEG chains in the hydrogel network. As a result, the PEGDA chains switched from the extended state to the coiled state, surrounding the K^+ ion in the center, which caused the network to reduce its size, thus unraveling the bilayer structure (Figure B.4g).

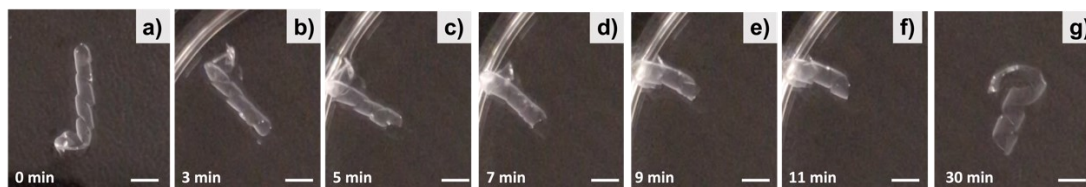


Figure B.4. Pictures of the PEGDA-based hydrogel/PDMS bilayer actuator shape changing in response to a 1.0 M KCl solution. a) The helical structure of the bilayer actuator after DI water equilibrium; b-f) pictures of the bilayer actuator immersed in the KCl solution after 3 min, 5 min, 7 min, 9 min and 11 min, respectively; g) the unraveled helical bilayer actuator after 30 min soaking in the KCl solution. (Scale bar represents 1.0 cm in length.)

A.4 Conclusions and Outlook

To conclude, we investigated the alkaline metal ion responses of the PEGDA-based hydrogels. We speculated that due to the coordination interaction between the K^+ ions and PEG chains, the hydrogel crosslinked by PEGDA showed a size reduction with PEGDA incorporation. A series of experiments were carried out to find the optimum PEGDA concentration incorporation. Moreover, we fabricated a PEGDA-based hydrogel/PDMS bilayer actuator that adopted a helical structure after equilibrated in DI water. The KCl alkaline metal ion solution actuated the shape morphing of the helical bilayer actuator by unraveling and shortening the structure.

However, there still are many problems to solve. For example, more repetitions are needed for all the tests. Also, osmotic pressure effects were not investigated thoroughly. More studies are needed on how we can reduce the concentration of the KCl solution but keep the same, if not better, actuation performances. We would like to inspire more ideas of using this mechanism to realize more novel actuation applications.

Appendix C

A PNIPAm/P(AAm-co-AAc) Bilayer Actuator with Locking and Unlocking Mechanism

C.1 Introduction

PNIPAm hydrogels have been studied extensively due to their temperature-responsive properties. PAAm hydrogels also are receiving more attention due to their simple synthesis and easy addition of other functionalities utilizing copolymerization methods. More complex properties can be achieved by combining both materials, which could expand their individual potentials.

Controlled factors that can dictate the behavior of actuator are of great interest in the area of on-demand actuation. In this chapter, we fabricated a pNIPAm/p(AAm-co-AAc) bilayer actuator with locking and unlocking mechanism. The actuator can be actuated with a temperature change as well as Fe^{3+} ions soaking, which can be tailored for on-demand actuation.¹⁴⁹⁻¹⁵¹

C.2 Experimental Section

Materials: The N-isopropylacrylamide monomer (NIPAm) (MW = 113.16 g/mol) was obtained from TCI Chemicals (Tokyo, Japan), and was recrystallized in hexane before use. Acrylamide (AAm, >99% (HPLC)), acrylic acid (AAc, 99%), N, N-methylenebisacrylamide (BIS, 99%), 2,2-diethoxyacetophenone (DEAP, PI, >95%), poly(ethylene glycol) (PEG, average mol wt 8,000), and iron (III) chloride (FeCl_3 , 97%) were purchased from Sigma Aldrich (St. Louis, Missouri, USA). Hydrogen chloride (HCl, FW/PM: 36.46) was purchased from Caledon Laboratories (Georgetown, Ontario, Canada). All the chemicals were used as received without further purification, unless otherwise indicated. UV lamp (50W, 365 nm) was purchased from Everbeam (British Columbia, Canada).

Fabrication of a PNIPAm/P(AAm-co-AAc) Bilayer Actuator: NIPAm, BIS, PEG, and DEAP were weighed and mixed well in a centrifuge tube wrapped by tinfoil. AAm, BIS, PEG, AAc, and DEAP were weighed and mixed well in a centrifuge tube

wrapped by tinfoil. Both pre-solutions were purged in nitrogen gas for 5 min, and stored in the fridge at 4 °C for later use. To prepare the container for the fabrication, a rectangular shape was carved out from the center of a Teflon sheet to afford a gasket; two identical Teflon gaskets were prepared. The first gasket was sandwiched between two glass slides, and the NIPAm pre-solution was filled into the Teflon gasket (Figure C.1). The gasket was sealed properly by clamping with some binder clips. The assembly was irradiated under the UV light for 5 min to polymerize the pNIPAm hydrogel. After that, the clips and the top cover slide were removed. The second Teflon gasket was placed on top of the first one to create additional space for the AAm pre-solution. The gasket was again sealed properly by binder clips. The assembly was irradiated under the UV light for another 5 min to polymerize the p(AAm-co-AAc) hydrogel. The obtained bilayer hydrogel was rinsed with DI water and soaked in DI water to reach equilibrium for later tests.

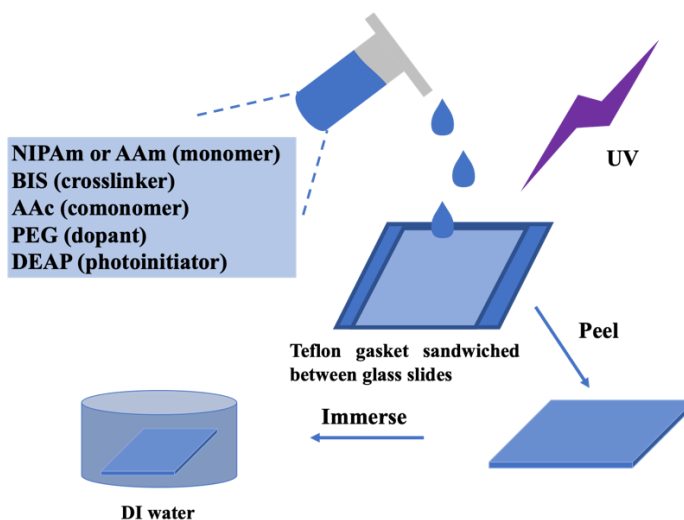


Figure C.1. The scheme for the synthesis of hydrogels and the bilayer actuator. The pre-solution was mixed well in a centrifuge tube and poured into a Teflon gasket sandwiched between two glass slides. The solution was irradiated under UV light to polymerize. To fabricate the bilayer actuator, the previous steps were repeated to polymerize the second hydrogel on top of the first. The afforded bilayer actuator was peeled from the mold and soaked in DI water.

Bilayer Actuator Actuation Test: The equilibrated bilayer actuator was immersed in a DI water bath. The water was heated slowly to increase the temperature. Meanwhile, a beaker containing 0.06 M FeCl₃ solution was heated at the same time. The bilayer strip bent towards the pNIPAm side to afford an arch-shaped strip. The

arched strip was transferred to the FeCl_3 solution to be locked. Afterwards, the strip was transferred to a room temperature water bath to reswell the pNIPAm hydrogel side. The strip was put in a 0.1 M HCl solution to bend towards the other side. The process was repeated a few times to test the durability and repeatability.

C.3 Results and Discussion

Using the Teflon gasket molding technique, we aim to fabricate a pNIPAm/p(AAm-co-AAc) bilayer actuator with locking and unlocking mechanism. The design of the actuator and the working mechanisms were shown in Figure C.2.

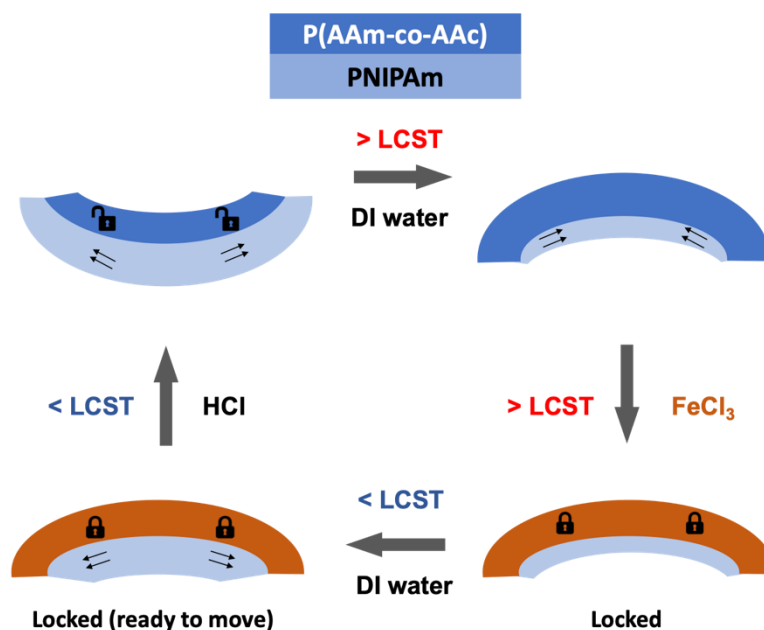


Figure C.2. Illustrations of the mechanisms for the actuation and bilayer actuator design. Note: The bilayer actuator taken from the mold did not show any bending before the test. However, after the first cycle, the structure was consistent, showing repeatable two-sides bending.

The bilayer structure was heated in DI water to actuate the pNIPAm temperature-responsive layer. Due to the shrinking of the pNIPAm layer, the bilayer started to bend. In a FeCl_3 solution at a similar temperature, the bilayer actuator was soaked for 30 min to lock p(AAm-co-AAc) layer. Due to the strong coordination interaction between the Fe^{3+} ions and the acrylates, a secondary crosslink was established among the polymer network, which increased the stiffness and rigidity of

the p(AAm-co-AAc) layer thus locking the structure in this temporary shape. After the actuator was transferred to room temperature DI water, the pNIPAm temperature-responsive layer reswelled due to lower than LCST environment. However, the locked p(AAm-co-AAc) layer restrained the opening of the bilayer structure, even though there was strong tension exerted by the swollen pNIPAm layer. The tension was released by the “key”, which was the HCl solution introduced that can destroy the Fe^{3+} /acrylate crosslinking points. The whole process was repeated without obvious performance deterioration. The preliminary results showed promising applications of this mechanism being used for various actuation designs.

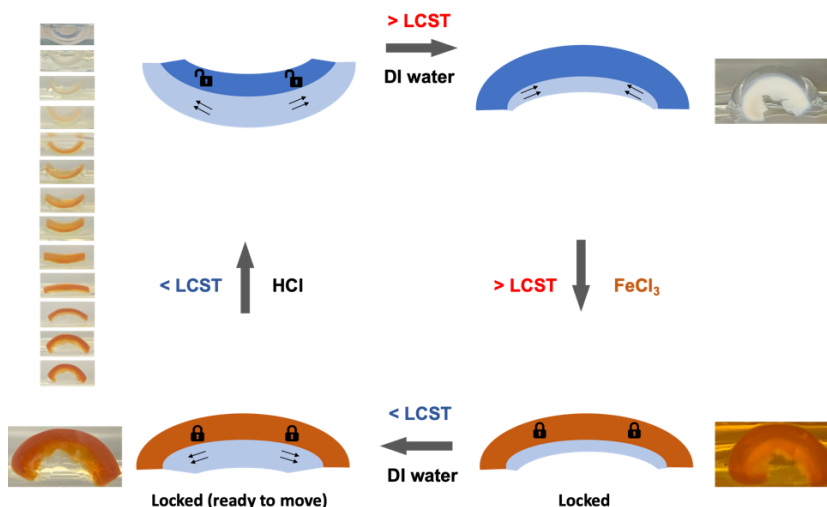


Figure C.3. Pictures of the pNIPAm/p(AAm-co-AAc) bilayer actuator shape changing in one locking/unlocking cycle. The cycle was performed four times; similar behavior was observed.

C.4 Conclusions and Outlook

To conclude, we fabricated a pNIPAm/p(AAm-co-AAc) bilayer actuator with locking and unlocking mechanism. The temperature-responsive layer pNIPAm could actuate when temperature was raised above LCST to bend the bilayer structure towards the pNIPAm side. The resulted bent actuator was soaked in FeCl_3 solution at temperature above LCST to lock the p(AAm-co-AAc) layer into a stiffly crosslinked hydrogel. The coordination interaction between the Fe^{3+} ions and the acrylates could explain this behavior. This locked hydrogel actuator could only be re-actuated to bend with the HCl

solution “key”. The process could be repeated many times without obvious performance failure.

However, there still are many problems to solve. For example, more repetitions are needed for all the tests. Also, more characterizations were needed, quantitatively. Hopefully, this novel locking/unlocking actuator could inspire more ideas of using this mechanism to realize more novel actuation applications.

Appendix D

Developing a Science Education Kit Based on the Swimming Device Project

D.1 Introduction

The previous work in Chapter 2 titled “Octopus-Like Shape-Memory-Alloy-Based Bistable Metal Actuators” received a lot of interests among friends and colleagues. The final product from project, a swimming device, is just like a fun toy that children would be really interested in playing with, let alone that there were a lot of scientific knowledge involved in the fabrication process. This enlightened us to start developing a science education set for children.

Considering the intricacies and difficulties that were encountered in the project, we aim to simplify the fabrication process, remove all the possible hazards, optimize all the key components, and emphasize the key steps that are more valuable for science education. Hopefully, we can develop a science education set that can inspire children in exploring science, as well as having fun with their hand-made products.

D.2 Experimental Section

Designs and Optimizations: The focus of the experiments is to remove all the existing hazards, pre-fabricate or pre-assemble the parts that could involve hazards, optimize the designs for better performance, and emphasize the steps that involve more science knowledge.

“How-to” Manuals and Videos: A manual is needed for this science education kit that involves many steps. We would like to prepare a manual that is clear and attractive. In the manual, we would list all the components, describe what they are and what their functions, instruct on step-by-step assembly, and point out all the potential hazards and warnings. A “How-to” video would be made available online or with a CD enclosed. In the video, we would provide detail introductions on the components and science behind it, demonstrate step-by-step assembly, and give tips and warnings if needed. Specifically, the working mechanism of the Nitinol shape memory alloy and

the bistable metal strip will be discussed. We would like to incorporate the PDMS fish flipper sheet synthesis kit inside the package, so that the children can get their hands on some polymerization experiments. It is noted that some specific warnings regarding the chemicals and potential hazards will be provided.

D.3 Results and Discussion

According to *Industry Guide to Health Canada's Safety Requirements for Children's Toys and Related Products*, a lot of the components and designs of our previous swimming device needed attention. For example, the bistable metal strip was sharp, and it must be enclosed in a durable material to prevent cutting hazards. Also, the battery used was a lithium ion polymer battery (FCONEGY 11.1 V 3S 7000 mAh 40 C Lipo RC Rechargeable Battery), which might be a potential hazard for children.

First, we redesigned how PDMS fish flippers are attached to the bistable metal strip. Previously, we used superglue to fix the flipper, which caused hardening of the material and difficulty for disassembly. To solve this problem, we decided to cut a few openings on the flipper. The bistable metal strip could be inserted easily into these openings (Figure D.1a). This resolved the permanent attachment problem, and added the convenience when removal of the flippers is needed.

Second, the spacing fish string was redesigned. In the previous design, the spacing string needed readjustments constantly to ensure similar actuation length for both sides so that the simultaneous two-arm snapping/slow moving movements could be realized. We came up with a new beaded spacing string that is shown in Figure D.1b-c. We can tune the spacing by adjusting the beads position.

Third, we looked into the PAAm hydrogel used on the Nitinol coil for heat loss prevention. In the previous design, a piece of hydrogel with a vacant channel in the center was hooked onto the Nitinol wire. Once the two ends were fixed to the electric wire, it became difficult to make any alterations to the gel. Besides, the hydrogels were not robust, and could break easily if not handled well. If the children break the hydrogel, it will be a lot of efforts to disassemble the wire and replace the broken hydrogel. Moreover, the hydrogels need to stay hydrated, which means that the swimming device should be immersed in water the whole time; biofouling and rusting could be a problem.

To solve this problem, we came up with an alternative material—3M VHB™ acrylic tape (Figure D.1d-f). This thin tape is very elastic, which will not hinder the movement of the Nitinol coil. It also is very durable, and easy to add onto or remove from the Nitinol. The tape worked great as a thin layer to hinder the heat loss to water, which served the same purpose of the hydrogel used previously.

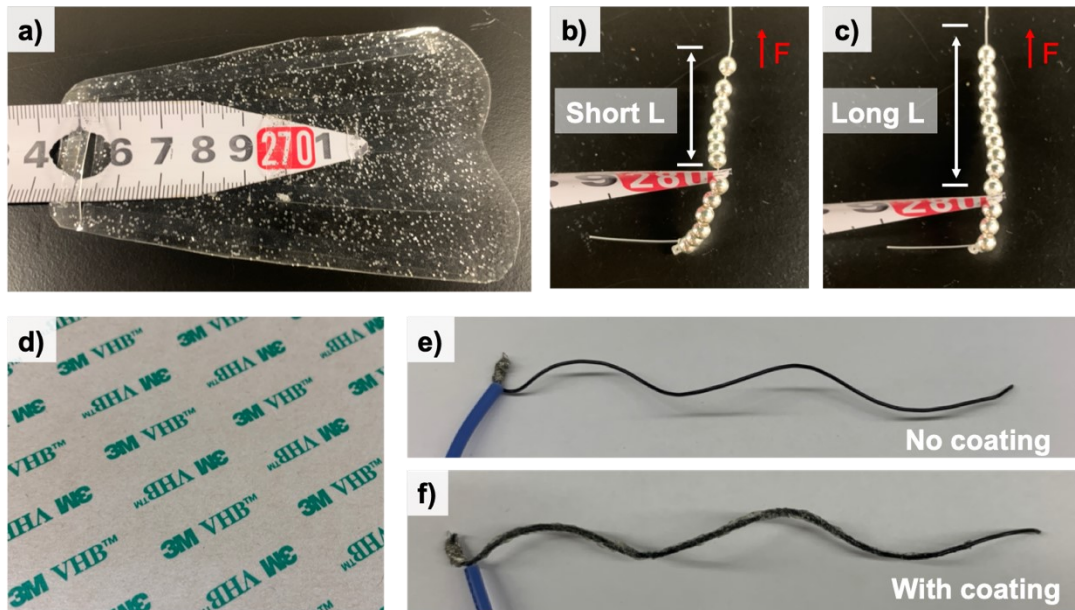


Figure D.1. Pictures of the parts that were optimized. a) The fish flipper with cut openings for easier operations; b-c) the beaded spacing string design that enabled easier adjustment of the effective actuation length (b with short actuation length; c with long actuation length); d) the picture of the 3M VHB™ acrylic tape that was used; e) the Nitinol wire without any coating; f) the Nitinol coil coated with 3M VHB™ acrylic tape.

D.4 Conclusions and Outlook

To conclude, we redesigned the swimming device to fit the purpose of developing a science education kit. Many problems were identified, and solutions were provided. Specifically, the *Industry Guide to Health Canada's Safety Requirements for Children's Toys and Related Products* was read to comply with the regulations required for safe products. To make the design easier to assemble, we changed the flippers, replaced the fish spacing string with a beaded spacing design, and replaced the fragile hydrogels with a robust and easy to handle 3M VHB™ acrylic tape. We also planned to make the “How-to” manuals and videos for better education and demonstration purposes.

Chemistry is a cool science, which should receive more attention than it has right now. This additional exploration after the development of the swimming device inspired us to care more about children's science education. Hopefully, more "unfathomable" scientific research can be brought to younger generations to intrigue their interests, and ultimately, cultivate a prosperous science education environment.